

ABSTRACT

Title of Dissertation: EXPERIMENTAL AND COMPUTATIONAL
INVESTIGATION OF PLANAR ION DRAG
MICROPUMP GEOMETRICAL DESIGN
PARAMETERS

Vytenis Benetis, Doctor of Philosophy, 2005

Dissertation directed by: Professor Michael Ohadi
Department of Mechanical Engineering

To deal with increasing heat fluxes in electronic devices and sensors, innovative new thermal management systems are needed. Proper cooling is essential to increasing reliability, operating speeds, and signal-to-noise ratio. This can be achieved only with precise spatial and temporal temperature control. In addition, miniaturization of electric circuits in sensors and detectors limits the size of the associated cooling systems, thereby posing an added challenge. An innovative answer to the problem is to employ an electrohydrodynamic (EHD) pumping mechanism to remove heat from precise locations in a strictly controlled fashion. This can potentially be achieved by micro-cooling loops with micro-EHD pumps. Such pumps are easily manufactured using conventional microfabrication batch technologies.

The present work investigates ion drag pumping for applications in reliable and cost effective EHD micropumps for spot cooling. The study examines the development, fabrication, and operation of micropumps under static and dynamic conditions. An optimization study is performed using the experimental data from the micropump prototype tests, and a numerical model is built using finite element methods.

Many factors were involved in the optimization of the micropump design. A thorough analysis was performed of the major performance-controlling variables: electrode and inter-electrode pair spacing, electrode thickness and shape, and flow channel height. Electrode spacing was varied from 10 μm to 200 μm and channel heights from 50 μm to 500 μm . Also, degradation of the electrodes under the influence of an intense electric field was addressed. This design factor, though important in the reliability of EHD micropumps, has received little attention in the scientific and industrial applications literature.

Experimental tests were conducted with prototype micropumps using the electronic liquid HFE7100 (3M[®]). Flow rates of up to 15 ml/min under 15 mW power consumption and static pumping heads up to 750 Pa were achieved. Such performance values are acceptable for some electronic cooling applications, where small but precise temperature gradients are required.

EXPERIMENTAL AND COMPUTATIONAL INVESTIGATION OF PLANAR
ION DRAG MICROPUMP GEOMETRICAL DESIGN PARAMETERS

by

Vytenis Benetis

Dissertation submitted to the Faculty of the Graduate School of the
University of Maryland, College Park in partial fulfillment
of the requirements for the degree of
Doctor of Philosophy
2005

Advisory Committee:

Professor Michael Ohadi, Chair/Advisor
Associate Professor Elisabeth Smela, Co-advisor
Associate Professor Jungho Kim
Professor Ugo Piomelli
Professor Gary A. Pertmer

©Copyright by

Vytenis Benetis

2005

Dedicated
to
Lina, my lifetime friend

Acknowledgements

First and foremost I would like to thank my advisor Dr. Michael Ohadi, who has put enormous faith and trust in me. He never stopped encouraging and guiding me during the entire length of my studies and research.

I would also like to thank my co-advisor, Dr. Elisabeth Smela, for her continuous advice not only in her specialty area of MEMS but also for her guidance on the path of researcher (and extensive help with the final thesis).

I also extend my appreciation to the other members of my advisory committee who have constantly provided constructive advice and guidance, Dr. Jungho Kim and Dr. Gary A. Pertmer. Especially I would like to thank another advisory committee member, Dr. Ugo Piomelli for his continuous support not only in the academic but also in many of the daily challenges associated with the life as a foreign student in the US.

During the course of my research, I had the privilege of working with and being advised by several fellow scientists, including Dr. Jafar Darabi, Dr. Francis Franca, Dr. John Lawler, Dr. Serguei Dessiatoun and Dr. Jianwei Qi, to whom I wish to express my sincere gratitude.

I am grateful to my many friends and colleagues at the Smart and Small Thermal Systems (S^2TS) Laboratory for providing a stimulating, constructive and fun environment in which I learned and grew. I am especially thankful to Amir Shooshtari, Parisa Foroughi, Sourav Chowdhury, Guohua Kuang, Saeed Moghaddam, Arman Molki, Mihai Catalin Rada, Valentin Tudor, Jianlin Wu, Mohamed Al-Shehhi and Ebrahim Al-Hajri.

I also wish to thank the AHX/EHD Consortium and ATEC Inc. for their long and invaluable financial support of this project.

My dear parents have always supported me during the years of academic pursuits in the foreign countries. Their patience, love and care have provided me the strength to work harder and not to give up under the times of difficulties. For all of that I would like to send them my dearest thanks.

Finally, I would like to express gratitude to my dearest friend Lina whom I dedicated this work to, and who had appeared in my life during this research, and helped me daily with her unmatched love and care.

TABLE OF CONTENTS

LIST OF TABLES	IX
NOMENCLATURE	XI
CHAPTER 1 INTRODUCTION.....	1
1.1 BACKGROUND.....	1
1.2 RESEARCH OBJECTIVES	3
1.3 RESEARCH SEQUENCE	3
CHAPTER 2 FUNDAMENTALS OF ELECTROHYDRODYNAMIC (EHD) PUMPING	
PHENOMENA	7
2.1 INTRODUCTION	7
2.2 ELECTROHYDRODYNAMICS PUMPING FUNDAMENTALS.....	7
2.2.1 <i>Electrohydrodynamics (EHD) definition</i>	7
2.2.2 <i>Electric body forces</i>	8
2.3 GOVERNING EQUATIONS	10
2.3.1 <i>Electrical equations</i>	10
2.3.2 <i>Fluid flow equations</i>	13
2.3.3 <i>Nondimensional form of the governing equations</i>	14
2.3.4 <i>Application equations</i>	15
2.4 ELECTRIC CHARGE BEHAVIOR IN THE EHD PHENOMENON	17
2.4.1 <i>Charge generation in liquids</i>	17
2.4.2 <i>Polar and non-polar liquids</i>	18
2.4.3 <i>Current density - electric field characteristic curve</i>	18
2.4.4 <i>Ion mobility</i>	20
2.4.5 <i>Charge decay</i>	21
2.4.6 <i>Space charge limited current</i>	23
2.4.7 <i>Summary</i>	24

2.5	LITERATURE REVIEW	25
2.5.1	<i>Ion-drag pumps</i>	25
2.5.2	<i>Other EHD pumps</i>	36
2.6	SUMMARY	39
CHAPTER 3 ION DRAG MICROPUMP DESIGN, FABRICATION, AND TESTING		41
3.1	INTRODUCTION	41
3.2	MICROPUMP DESIGN	42
3.2.1	<i>Fabrication method and material selection</i>	44
3.2.2	<i>Electrode geometries</i>	50
3.2.3	<i>Channel height considerations</i>	53
3.3	MICROPUMP FABRICATION.....	54
3.4	MICROPUMP TEST SETUP	59
3.4.1	<i>Pump packaging</i>	59
3.4.2	<i>Test loop</i>	65
3.4.3	<i>Measurement and instrumentation</i>	69
3.5	SUMMARY	74
CHAPTER 4 EXPERIMENTAL RESULTS.....		76
4.1	INTRODUCTION	76
4.2	CLASSIFICATION AND NOMENCLATURE OF THE MICROPUMP PROTOTYPE DESIGNS.....	76
4.3	DISCUSSION AND CLASSIFICATION OF THE MICROPUMP DESIGN PARAMETERS	78
4.4	SUMMARY OF THE MICROPUMP PROTOTYPES	82
4.5	TESTING PROCEDURE CONSISTENCY.....	83
4.6	DATA REDUCTION WORKFLOW.....	86
4.7	TEST RESULTS OF THE GEOMETRICAL DESIGN PARAMETERS	87
4.7.1	<i>Overview</i>	87
4.7.2	<i>Electrode thickness</i>	88
4.7.3	<i>Surface roughness</i>	89

4.7.4	<i>Flow channel height</i>	91
4.7.5	<i>Electrode gap and spacing between electrode pairs</i>	99
4.7.6	<i>Electrode pair spacing, further investigation</i>	106
4.7.7	<i>Electrode shape (2D and 3D)</i>	109
4.7.8	<i>Characteristic curves and efficiency optimization</i>	112
4.8	PUMP RELIABILITY ISSUES AND ANALYSIS	114
4.8.1	<i>Electrode degradation</i>	115
4.8.2	<i>Working fluid performance with EHD phenomenon</i>	121
4.8.3	<i>Charge behavior and electric breakdown</i>	124
4.8.4	<i>Pump reliability and test repeatability</i>	129
4.9	SUMMARY AND CONCLUSIONS	131
CHAPTER 5 NUMERICAL WORK		133
5.1	INTRODUCTION	133
5.2	MODELING OF ION-INJECTION PUMPING MECHANISM	134
5.2.1	<i>Model assumptions and governing equations</i>	134
5.2.2	<i>Boundary conditions</i>	138
5.3	MODEL APPLICATION TO THE ION-INJECTION PUMP USING NUMERICAL SOLVER	139
5.3.1	<i>Problem setup</i>	140
5.3.2	<i>Model verification</i>	146
5.3.3	<i>Conclusion on numerical model verification</i>	154
5.3.4	<i>Convection current modeling</i>	157
5.4	NUMERICAL RESULTS	158
5.4.1	<i>Channel height effect on pump's performance</i>	158
5.4.2	<i>Inter-electrode distance effect on pump performance</i>	161
5.4.3	<i>Discussion of the flow patterns</i>	162
5.4.4	<i>Electric field simulation</i>	167
5.5	SUMMARY	172

CHAPTER 6 CONCLUSIONS AND RECOMMENDED FUTURE WORK	174
6.1 INTRODUCTION	174
6.2 OVERVIEW AND CONCLUSIONS	174
6.3 RECOMMENDATIONS	177
6.3.1 <i>Recommendations on the test setup</i>	177
6.3.2 <i>Recommendations on the design and fabrication of EHD micropumps</i>	181
6.3.3 <i>Recommendations on the numerical modeling of the ion-drag micropump</i>	184
6.4 SUMMARY	185
APPENDIX A	186
APPENDIX B.....	191
REFERENCES	192

LIST OF TABLES

Table 2-1 Primary dimensionless parameters based on conservation equations.	14
Table 2-2 Summary of ion-drag pump experimental works (only selected information is listed).....	34
Table 3-1 Comparison of planar and grid type ion-drag micropumps.....	43
Table 3-2 Factors influencing the selection of micropump 1) material and 2) geometry.	45
Table 3-3 Electrode potential for several common elements with respect to the hydrogen reference reaction (eFunda 2005).	46
Table 3-4 Work functions of several common metals (eFunda 2005).....	47
Table 3-5 Physical properties of HFE-7100 in comparison with a number of other liquids.*	49
Table 3-6 Pressure transducer and output signal demodulator specifications.	70
Table 3-7 Specifications for gas flow meter.	72
Table 3-8 Data acquisition unit specifications.....	73
Table 3-9 DC power supply specifications.....	74
Table 4-1 Micropump design variables	77
Table 4-2 Micropump performance parameters.	80
Table 4-3 Description and explanation of frequently used types of plots.	80
Table 4-4 Test matrix.....	83
Table 4-5 Typical raw data from a micropump.	87
Table 4-6 Micropump design comparison for different methods of evaluation (1-best, 7-worst).	104
Table 4-7 Deterioration of electrodes.	116

Table 4-8 Elemental analysis for emitter and collector electrodes obtained with WDS.	
All values are relative percentages by weight.....	121
Table 5-1 HFE7100 physical properties reported by 3M [®]	141
Table 5-2 Boundary conditions for the electrostatics mode.....	142
Table 5-3 Boundary conditions for the electrokinetic mode.....	143
Table 5-4 FEMLAB input variables and constants for the 50f100-220 pump model. ..	148
Table 5-5 Comparison of the fluid fields with and without convection current included.	
50f100-100 micropump design with test loop setting #1.....	157
Table 5-6 Flow streamlines overlaid on the velocity field for ion-drag micropump	
50f100 with 10, 50, 100, and 220 μm channel heights. Velocity vectors are represented	
by white arrows, and velocity magnitude is shown according to the B-W color gradient	
scale shown to the right of the graphs. Operating conditions: 600 V input voltage,	
external loop with valve setting #1.....	164
Table 5-7 Charge density profiles for ion-drag micropump 50f100 with 10, 50, 100, and	
220 μm channel heights. Velocity vectors are represented by black arrows and the	
magnitude of velocity is shown in the B-W color scheme.....	166
Table 6-1 Effect of geometrical parameters on the performance of the pump.....	175

NOMENCLATURE

A	Cross-sectional area
C	Nondimensional number defining injection regime (Atten 1996)
D	Diffusion coefficient (m^2/s)
D	Electric displacement (C/m^3)
E_0	Electric charge constant, 1.6×10^{-19} (C)
E	Electric field intensity (V/m)
F_e	Electric body force (N/m^3)
I	Electrical current (A)
J	Electric current density (A/m^2)
k_d	Dissociation constant [$\text{m}^3/(\text{C}\cdot\text{s})$]
k_r	Recombination constant [$\text{m}^3/(\text{C}\cdot\text{S})$]
L	Length scale (m)
M_A	Mass of molecule (a.m.u.)
N_A	Avogadro's number, $6.023 \times 10^{23} \text{ mol}^{-1}$
n	Unit normal surface vector
p	Pressure (Pa)
P	EHD input power (W)
P	Polarization vector (C/m^3)
q	Fluid flow rate (ml/min)
R	Radius of molecule (m)
r_A	Radius of the electrode tip (m)

t	Time (s)
T	Temperature (K)
u	Velocity of fluid or medium (m/s)

Greek Letters

ϵ	Electric permittivity (F/m)
ϵ_0	Permittivity of free space
ϵ_r	Dielectric constant (F/m)
η	Electrohydrodynamic efficiency
μ	Dynamic viscosity of fluid (Pa.s)
μ_e	Mobility of charge ($\text{m}^2/\text{V.s}$)
ν	Kinematic viscosity of fluid (m^2/s)
ρ	Fluid density (kg/m^3)
ρ_e	Volume charge density (C/m^3)
ρ^0	Injected charge density (C/m^3)
ρ_e^0	Injected charge density in absent of the electric field (C/m^3)
σ_e	Electric conductivity (S/m)
φ	Electric potential (V)
τ	Fluid stress tensor (N/m^2)

CHAPTER 1 INTRODUCTION

1.1 Background

Engineers know that no electronic circuit design can meet the high performance and reliability standards of a global economy just by considering the primary electronic function: secondary structural and thermal design features are important as well. Because of increasing heat fluxes resulting from shrinking device sizes and more densely packed circuitry, thermal control of the electric circuit is so essential that in many cases it is a limiting consideration in the design. As the amount of heat generated per unit volume grows, while the specified operating temperature range stays almost constant and the surface area available for heat dissipation is reduced, conventional thermal management solutions become insufficient or impossible to apply. Other limiting factors, such as requirements for operation in harsh environments or restraints on the acoustic noise produced by the cooling system, further limit the applicability of various cooling techniques. As an example, conventional airflow fans either cannot handle the heat load or are too bulky and noisy for cooling super-computer microprocessors. Yet continuous growth in heat flux per unit area is expected, not only in high-end electronics, but also in conventional electronics.

It is clear that current thermal management solutions require change, and that simply scaling down current cooling technologies is not possible. New technologies and materials have to be combined to remove the new high heat fluxes. In addition, good understanding of the problem is needed in order to come up with cost-effective solutions.

One important aspect of the high heat flux problem is that most of the peak energy is generated in so-called “hot spots.” This means that only certain spots experience excessively high temperatures, not the entire surface, and reliability failures tend to occur in such hot spots. Hot spot sizes vary, but are typically an order of magnitude smaller than the overall dimensions of the device. Thermal management of hot spots would be most efficiently handled by localized or spot cooling.

Furthermore, since the sizes of electronic devices are constantly being reduced, the dimensions of the cooling system should be scaled down as well to yield a compact overall product design. A relatively new field of engineering called MEMS (micro-electromechanical systems) might be the most appropriate solution to the development of small-scale thermal management systems for spot cooling. Combining microfluidics with various actuating mechanisms to produce a micro-scale cooling loop could yield an attractive solution (Shoji and Esashi 1994; Garimella and Singhal 2004). There are various types of cooling loops, but in general they include the following key components: an evaporator, coolant lines, a heat sink, and a pump.

The aim of the present study was to conduct research and development toward reliable and effective operation of such micro-pumps. Among the many actuating mechanisms available for pumping refrigerants, EHD pumping was chosen because of its applicability to microelectronics as well as to an array of biomedical applications and other local fluid flow applications. EHD pumping has many advantages. First, EHD has been shown to be simply implemented in small-scale structures using standard microfabrication technologies. Second, EHD pumps do not have any mechanically wearable parts, and thus cause no acoustic signature due to vibration. Third, EHD pumps

are easily controllable devices since input electric power has a precise relationship with the flow rate in a particular device. Finally, these pumps consume little power and are attractive not only in conventional electronics, but also in the fast-growing mobile and portable electronics industries.

1.2 Research objectives

This study aimed to fully investigate the practical and theoretical operation of an EHD ion-drag micropump through the accumulation of analytical, numerical, and experimental data, with a particular emphasis on the geometry of the design. The specific objectives of the present research study were the following.

- Examine the operation of the ion-drag micropump under static and dynamic conditions, and use these tests to optimize the pump.
- Investigate the effect of design variables on the performance of the micropump, including electrode spacing, electrode pair spacing, electrode shape, and channel height.
- Monitor the long-term reliability of the micropump and examine the effects of pumping on the fluid and the electrode surfaces.
- Develop a simplified numerical model of the micropump using a commercial finite element code, and use the model to further understand, predict, and improve the pump's performance.

1.3 Research sequence

This study represents the continuation of EHD pump research initiated by Mihai Rada and Jeff Darabi, former Ph.D. students and fellow researchers at the Small and

Smart Thermal System laboratory of the University of Maryland. These researchers performed a feasibility study and a preliminary static pressure test on an EHD micropump. Their work, primarily at the meso-scale, was reported in journal articles and in the authors' theses (Darabi, Rada et al. 2002; Rada 2004). Rada's work focused mainly on EHD mesoscale pumping of cryogenic liquids. EHD micropump prototypes were designed, tested, and evaluated without taking into account either the important design parameters mentioned above or fluid contamination, and no closed loop (dynamic) tests were performed.

This PhD investigates the EHD ion-drag micropump in depth, while identifying the most important variables and evaluating their effects on the pump's performance. First, a comprehensive literature review of existing information on the EHD phenomenon was conducted, and the governing equations defining the operation of the micropump were collected. These findings are documented in Chapter 2. Needless to say, the EHD phenomenon has never been fully understood, and knowledge in this field is being constantly updated by researchers all over the world.

As explained in Chapter 2, EHD is a broad concept that includes various electrical body forces acting on the working fluid. The particular type of micropump investigated in the present study is called an ion-drag pump, and it is based on Coulomb forces acting on free charges injected into the working fluid from a so-called emitting electrode. To further understand the complexity of the EHD phenomenon, other EHD mechanisms are also reviewed in Chapter 3.

In parallel with accumulating knowledge and building the analytical model, experiments moved ahead at full steam. Micropump prototypes were built using

microfabrication facilities at the University of Maryland. A test loop was designed and built to address formerly ignored issues, such as isolation of the system from the environment, generating the pumps' characteristic curves, and determining the pumps' efficiency. These tests led to an identification of the shortcomings of the pump, the loop, and the packaging, and to improvements in later design iterations. The test results are presented in Chapter 4.

In Chapter 5, numerical modeling of the ion-drag micropump is discussed. The modeling was completed in the later stages of the research, as previously no commercial numerical software capable of solving these or similar PDEs was available. A parallel study was conducted by a laboratory colleague, Dr. Amir Shooshtari, who used the commercial CFD code Fluent UDF (user defined functions) to encode the EHD equations. However, this was custom work requiring an in-depth understanding of CFD code, and it required much time to develop and to be understood by others. Another software package that our laboratory had been using since its inception is FEMLAB (created by Comsol, Inc.). This multi-physics finite element code first appeared as a rudimentary program for solving systems of PDEs, and it eventually progressed to a 2-D code with GUI. This software was used for electric field simulation in various 2-D electrode geometries, but its limitation to flat surfaces (or symmetric 3-D volumes) prevented more complex electrode geometries from being investigated. With ever increasing power, a transition to 3-D space, and numerous other improvements, FEMLAB enabled us to tailor one of their modules to modeling the EHD pumping mechanism. Since this numerical work is a result of the last part of the research period,

only results from a simplified mono-ionic model are presented, while further work with suggested improvements is described at the end of the chapter.

Finally, chapter 6 provides an overview and draws conclusions from the entire study, compares the numerical and experimental results, describes the key findings, and proposes further studies in the field.

CHAPTER 2 FUNDAMENTALS OF ELECTROHYDRODYNAMIC (EHD) PUMPING PHENOMENA

2.1 Introduction

This chapter introduces the definition, the fundamental physics, and the governing equations characterizing the electrohydrodynamic (EHD) pumping mechanism. This information is particularly focused on ion-drag pumping and on the relevant assumptions and simplifications needed to make the governing equations practical for use in analytical and numerical analysis. In this Chapter, some fundamental EHD concepts are reviewed first, followed by a literature review of the existing work in the field, especially on the development, optimization, and modeling of ion-drag pumps. In order to avoid unnecessary redundancy, additional material should be obtained from the introductory chapters of the theses of Darabi (Darabi 1999), Rada (Rada 2004), and Shooshtari (Shooshtari 2004), which provide in-depth discussion on certain aspects of the EHD phenomena.

2.2 Electrohydrodynamics pumping fundamentals

2.2.1 Electrohydrodynamics (EHD) definition

Electrohydrodynamics (EHD) is a field of science that studies the interaction between dielectric fluids and electric fields. This interaction generates fluid movement, which can take various forms: pumping, agitation, and mixing. The low electrical

conductivity of dielectric fluids under large electric fields results in small electric currents, and thus low power consumption.

2.2.2 Electric body forces

EHD-induced fluid motion is due to electric body forces. The nature of these forces is best understood through a step-by-step derivation as presented by Darabi (Darabi 1999); however, the derivation is omitted here due to its length and complexity. In brief, since the force density F_e acting on a dielectric liquid has not been successfully modeled using a microscopic model, the law of conservation of energy is used to evaluate the increment in energy due to the presence of a space charge ρ_e in a dielectric medium with permittivity ϵ , density ρ , and external electric field E (Stratton 1941):

$$\mathbf{F}_e = \rho_e \mathbf{E} - \frac{1}{2} E^2 \nabla \epsilon + \frac{1}{2} \nabla \left[E^2 \rho \left(\frac{\partial \epsilon}{\partial \rho} \right)_T \right] \quad (2-1)$$

The three components in Eq. (2-1) represent different types of forces acting on the fluid. The first term, called the electrophoretic force, represents the Coulomb force acting on a free space charge in the presence of an electric field. The nature of this force is easy to imagine, as it derives from Coulombs' law, which states that a charge q placed in an electric field will experience a force equal to the product of the charge and the electric field in the direction of the field for positive charges and in the opposite direction for negative charges. (Since ρ_e is the charge density, F_e is considered to be a force density rather than a force.) Since ρ_e represents the sum of all the charge densities (positive and negative), only one direction and size of the force is defined for the EHD model at any time. This relationship indicates that fluid motion will follow the direction of the applied external field.

The second term is known as the dielectrophoretic or Korteweg-Helmholtz force density. It is defined for fluids in which a gradient in permittivity is observed. It can be shown by expansion of the dielectrophoretic term that such a gradient can be present only in two-phase or non-isothermal fluids.

$$\frac{1}{2} E^2 \nabla \varepsilon = \frac{1}{2} E^2 \left(\left(\frac{\partial \varepsilon}{\partial \rho} \right)_T \nabla \rho + \left(\frac{\partial \varepsilon}{\partial T} \right)_T \nabla T \right)$$

(2-2)

Dielectrophoresis acts on neutral molecules that experience a translational force by being polarized and acted upon by a non-uniform electric field. The direction of motion is independent of the sign of the field, contrary to the phenomenon of electrophoresis (Darabi 1999).

The third term is known as electrostrictive force density. This force requires the presence of an inhomogeneous electric field or fluid compressibility. Using the Clausius-Mossotti relation, which describes dielectric fluid polarizability in terms of dielectric properties, it is possible to simplify the expression for electrostrictive force (Melcher 1981).

$$\frac{1}{2} \nabla \left[E^2 \rho \left(\frac{\partial \varepsilon}{\partial \rho} \right)_T \right] = \nabla \left(\frac{E^2 (\varepsilon - \varepsilon_0) (\varepsilon + 2\varepsilon_0)}{6\varepsilon_0} \right)$$

(2-3)

Ion-drag pumping uses a single-phase, incompressible fluid placed in a homogeneous electric field. Thus, only Coulombic body force causes mass transport. (In a hypothetical case where some thermally induced phase change or temperature gradient is present, dielectrophoretic force should be accounted for as well.)

2.3 Governing equations

With a solid understanding of the nature of EHD pumping, it is now necessary to set up the governing equations for ion-drag pumping. Electrical and fluid equations, derived from Maxwell's equations and fluid conservation, respectively, will be presented with a brief overview of the energy equations and the assumptions for excluding them. Finally, the governing equations will be presented in non-dimensional form. It should be mentioned that an in-depth derivation of the governing EHD equations has been reported in many previous publications (Melcher 1981; Castellanos and Gonzalez 1998; Shooshtari 2004), and only a simplified version applicable to the current study is presented here.

2.3.1 Electrical equations

Gauss's law, one of Maxwell's equations, defines the relationship between the electric field and charge density:

$$\nabla \cdot \vec{E} = \frac{\rho_e}{\varepsilon} \quad (2-4)$$

where E is electric field vector, ρ_e is charge density, and ε is permittivity of the dielectric medium. In addition, since the magnetic field is negligible,

$$\nabla \times \mathbf{E} = 0 \quad (2-5)$$

The irrotational nature of the electric field yields an expression for the electric field in terms of the potential field gradient.

$$\mathbf{E} = -\nabla\phi \quad (2-6)$$

Next, the law of charge conservation implies that

$$\frac{\partial \rho_e}{\partial t} + \nabla \cdot \mathbf{J} = 0 \quad (2-7)$$

where the electric current density, \mathbf{J} , is defined as the sum of the current density components both within the control volume medium and due to bulk motion of the medium. Under the unipolar charge assumption (discussed further in the section on migration charge density) as proposed by (Melcher and Firebaugh 1967), the current density \mathbf{J} is

$$\mathbf{J} = \mu_e \rho_e \mathbf{E} + D \nabla \rho_e + \rho_e \mathbf{u} + \sigma_e \mathbf{E} \quad (2-8)$$

where μ_e , D , ρ_e , and σ_e are the mobility, molecular diffusion coefficient, unipolar charge density, and conductivity of the bulk fluid, respectively.

Under high electric fields, as in the ion-drag mechanism, diffusion plays a negligible role and can be ignored. In addition, a steady state is assumed, thus making a time-dependent term unnecessary. Therefore

$$\mathbf{J} = \mu_e \rho_e \mathbf{E} + \rho_e \mathbf{u} + \sigma_e \mathbf{E} \quad (2-9)$$

These three current components (migration, convection, and conduction, respectively) will now be discussed individually.

Migration charge current (unipolar assumption)

Coulombic force is the key driver acting on *free* charges present in the fluid. The source of these charges is ion injection at the metal/liquid interface (discussed later in this chapter). Assuming a single type of charge (unipolar EHD model), the migration current density \mathbf{J} is defined as

$$\mathbf{J} = \mu_e \rho_e \mathbf{E} \quad (2-10)$$

The term $\mu_e \mathbf{E}$ is the velocity \mathbf{u} of these charge carriers, while ρ_e represents their volume density. It is also important to note that only migrative charge flux participates in the creation of fluid flow.

Convective charge current

When bulk liquid is in motion with a velocity \mathbf{u} , it produces a secondary motion of the charges present in the fluid. This secondary motion contributes to the total current flux, with this convective current density component calculated as the product of velocity \mathbf{u} and volumetric charge density ρ_e . In order to estimate the importance of the convective velocity, it should be compared to the migration velocity. As a first step, we check if the migration current velocity $\mu_e \mathbf{E}$ is more than one order of magnitude larger than \mathbf{u} . As a second step, we check whether the divergence of the migrative current flux is more than an order of magnitude larger than the divergence of the convective current flux. If both of these are true, then $\mathbf{u}\rho_e$ can be ignored. This issue is taken up again in the modeling chapter.

Electrical conduction current

As discussed earlier, the EHD phenomenon works only with low conductivity liquids, or dielectrics. Dielectrics are distinguished by two electrical properties: a resistivity (inverse of conductivity) above $10^7 \Omega\text{-m}$ and a dielectric constant below 20 (Schmidt 1997). As an electric field is applied to the fluid, the electrical conduction process begins as a result of dissociation of either neutral impurity molecules inside the liquid or ionization of the liquid molecules themselves. An equal number of opposite charges dissociate and recombine; thus, there is no net free charge, only the electric current equal to the product of the fluid conductivity and the external electric field.

For a typical single-phase ion-drag pumping application, dielectric liquids are chosen from among various refrigerants, such as CFCs (chlorofluorocarbons), HCFCs (hydrochlorofluorocarbons), HFCs (hydrofluorocarbons), and HFEs (hydrofluoroethers), which have conductivities in the range of 10^{-12} to 10^{-8} S/m. With a typical average electric field of 10^6 V/m, conduction current is expected to be in the range of 1 μ A to 10 mA.

2.3.2 Fluid flow equations

As discussed earlier, electric body forces can be combined with the fluid equations to complete the coupling between electrostatics and fluidics. The motion of an incompressible, Newtonian fluid with an electric body force \mathbf{F}_e acting on it is derived by combining the continuity and Navier-Stokes equations ((2-11) and (2-12), respectively).

$$\nabla \cdot \mathbf{u} = 0 \tag{2-11}$$

$$\rho \left[\frac{\partial \mathbf{u}}{\partial t} + (\mathbf{u} \cdot \nabla) \mathbf{u} \right] = -\nabla p - \nabla \cdot \boldsymbol{\tau} + \rho \mathbf{g} + \mathbf{F}_e \tag{2-12}$$

Energy equations

The equation of energy, evaluated from the energy conservation principle, could be added to the fullest description of the EHD phenomenon. The addition of these equations would be justified by the Joule heating produced by charge flux passing through the working fluid. An additional variable, temperature T , would be introduced and coupled to the electric (as a heat source) and flow (distributive heat mechanism) equations. In addition, temperature-dependent material properties would need to be considered for larger temperature variations. The overall system of equations would

become even more complex. Luckily, the ion-drag mechanism operates at a low power level, and the amount of heat produced in the bulk liquid is so small that no apparent heating was observed during the experimental stage of this study. For this reason, the energy equations were neglected.

2.3.3 Nondimensional form of the governing equations

Putting the EHD governing equations in a nondimensional form enables the study of the phenomenon independent of particular experimental conditions. Only equations applicable to the ion-drag mechanism under the assumption of unipolar charge migration are presented here; no dielectrophoretic or electrostrictive forces are shown. The results are based on work done by Shooshtari (Shooshtari 2004), who has summarized the applicable dimensionless parameters according to the IEEE-DEIS EHD Technical Committee recommendations (IEEE-DEIS-EHD Technical Committee 2003). These parameters are given in Table 2-1.

Table 2-1 Primary dimensionless parameters based on conservation equations.

Symbol	Expression	Name
Re	Lu/ν	Reynolds number
E_{hd}	$\rho_e EL^3 / \rho \nu^2$	EHD number (conductive electric Rayleigh number)
Md	$\epsilon_0 E^2 L^2 / \rho \nu^2$	Masuda number (dielectric electric Rayleigh number)
Sc	ν/D	Ion Schmidt number
F_E	$\mu_e EL/D$	Ion drift number

There are several other dimensionless parameters that can be expressed by a combination of the nondimensional parameters. One of them, the electric Reynolds number, Re_e , is particularly useful in nondimensional analysis of the ion-drag

mechanism. It is defined as $Re_e = \frac{\epsilon \cdot u}{\sigma_e L}$.

Using these dimensionless parameters, the nondimensional form of the governing equations can be derived. The dimensionless Gauss equation (i.e. Eq.(2-4)) is

$$\nabla^* \cdot (\varepsilon_s \mathbf{E}^*) = \frac{E_{hd}}{Md} \rho_e^* \quad (2-13)$$

For the steady state condition, the charge conservation equation, given in Eq. (2-7), becomes:

$$\frac{F_E}{E_{hd} \cdot Re \cdot Sc_i} \nabla^* \cdot \mathbf{J}^* = 0 \quad (2-14)$$

The dimensionless current density is defined as

$$\begin{aligned} \mathbf{J}^* &= \frac{L^3}{\rho v^2 \mu_e} \mathbf{J} \\ &= E_{hd} \rho_e^* \mathbf{E}^* + \frac{Re Sc_i Md}{Re_e F_E} \mathbf{E}^* + \frac{Re Sc_i E_{hd}}{F_E} \rho_e^* \mathbf{u}^* \end{aligned} \quad (2-15)$$

Nondimensionalization of the momentum equation Eq.(2-12), yields

$$\left[\frac{\partial \mathbf{u}^*}{\partial t^*} + (\mathbf{u}^* \cdot \nabla^*) \mathbf{u}^* \right] = -\nabla^* p^* + \frac{1}{Re} \nabla^{*2} \cdot \mathbf{u}^* + \mathbf{g}^* + \mathbf{F}_e^* \quad (2-16)$$

where the dimensionless EHD body force is

$$\mathbf{F}_e^* = \frac{L \mathbf{F}_e}{\rho U_0^2} = \frac{E_{hd}}{Re^2} \rho_e^* \mathbf{E}^* \quad (2-17)$$

2.3.4 Application equations

In addition to the governing equations, it is appropriate to present a set of equations that defines the output variables of the device under investigation. Flow rate, efficiency, current, and power are the main factors that define micropump performance.

Pumps are evaluated by their ability to perform work, which is given by flow rate and the generated pressure head. Pressure is a variable defined in the governing fluid equation, while the flow rate q is calculated by integrating the velocity \mathbf{u} over the flow cross-sectional area:

$$q = \int \bar{\mathbf{u}} \cdot \bar{\mathbf{n}} dA \quad (2-18)$$

In order to evaluate the EHD system efficiency, input power has to be calculated. For an ion-drag pump, the input is provided by an electric power supply and is calculated using $P = I \cdot \phi$, where I is total current and ϕ is the potential difference (applied voltage). Current I is defined as $I = \int \mathbf{J} dA$, where current density \mathbf{J} is defined by Equation (2-8).

The efficiency of an EHD pump is defined as the ratio of useful work to the power input. One obvious useful output measurement is the movement of the bulk liquid, which is equal to the product of the pressure head p and flow rate q . The efficiency for an EHD pump is calculated using

$$\eta = \frac{q \cdot \Delta p}{I \cdot \phi} \quad (2-19)$$

Efficiencies calculated according to the equation (2-19) are typically less than 6% as reported in various literature sources (Bryan and Seyed-Yagoobi 1990; Richter and Sandmaier 1990). The low efficiencies are due to large internal pressure drops. (Crowley suggests considering the work done to overcome the pressure drop inside the device as a useful work as well, thus “increasing” the efficiency up to 80% (Crowley, Wright et al. 1990).) Finally, it is important to add that although the largest fraction of

the input power is dissipated as heat, the total power is still small, on the order of milliwatts (as shown in the experimental data, Chapter 4).

2.4 Electric charge behavior in the EHD phenomenon

As discussed above, ion-drag pumping is dominated by Coulomb forces acting on charges in the fluid. This section will therefore discuss charge generation, transport, and recombination. In addition, some discussion is offered about the creation of the high electric fields necessary to produce free charges.

2.4.1 Charge generation in liquids

There are several ways that charged particles can appear in a dielectric fluid under the influence of an electric field. For conducting liquids, the dissociation-recombination processes always exists, providing balanced densities of both negative and positive ions. In less conducting fluids, an electric double layer, or heterocharge layer (discussed in the conduction and electroosmotic pumping section), can accumulate a local net charge. In dielectric fluids, two main charge generation processes are theoretically possible and are overviewed here.

Field ionization

Near an electrode of positive polarity, molecules adjacent to the electrode can become ionized due to electron being stripped from the liquid and tunneling into the metal. Field ionization energy is defined as the amount of energy needed to strip one electron from an atom to make it an ion. Field ionization becomes dominant when the difference between the ionization energy I of the fluid and the work function of the electrode metal ($I - \phi$) is smaller than the work function ϕ (Schmidt 1997). The work

function is the energy needed to free an electron from the surface of a metal. In other words, ionization energy I has to be at least twice as large as the work function ϕ before field ionization occurs. For typical combinations of dielectric fluids and electrode metals, this condition is never satisfied.

Ion injection in non-polar liquids

The method that dominates charge creation in dielectric liquids is field emission, sometimes called ion injection. It is applicable to non-polar liquids (defined in the next section) and is governed mainly by the electrode work function. In this case, electrons tunnel from the metal to the liquid. Field emission occurs at intense electric fields, and streamers of electrons destroy the double layer near the emitter surface and freely migrate into the bulk fluid.

2.4.2 Polar and non-polar liquids

Polar liquids have permanent dipoles. This asymmetry in molecular structure enables the use of dielectrophoretic force to establish motion in the field. Examples of polar liquids are water, acetone, and some alcohols.

Non-polar liquids form temporary dipoles only in the presence of external electric fields. Many of the dielectric liquids are non-polar, as is the working liquid investigated in this study, a hydrofluoroether with the commercial name HFE-7100 produced by 3M[®].

2.4.3 Current density - electric field characteristic curve

The various phenomena that take place during EHD pumping make themselves clear in an observation of current density vs. electric field. This curve typically displays

the behaviors shown in Figure 2-1, with four distinct regions (Schmidt 1997). (For a fixed geometry, an identical curve can be plotted for current vs. applied voltage.)

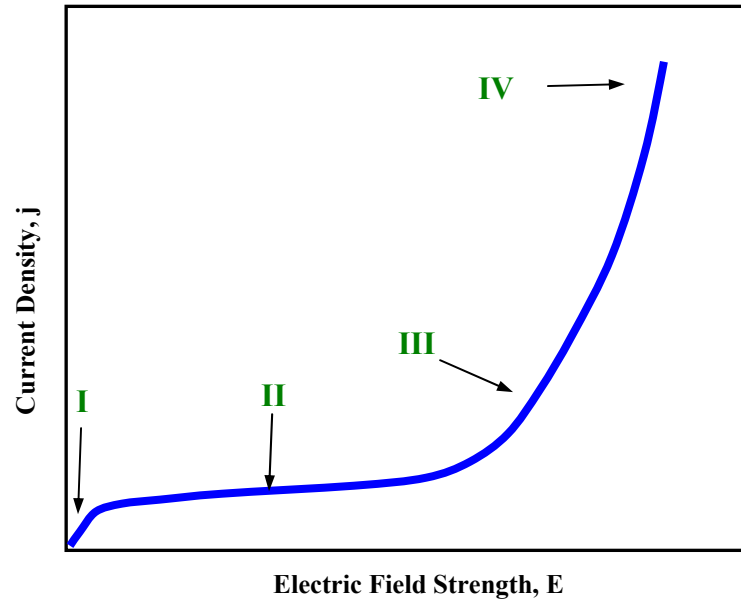


Figure 2-1 J-E characteristics of gases and nonpolar liquids.

In Region I, where electric field intensity is lowest (i.e. $E < 1$ kV/cm), current is due to impurities present in the liquid and is linearly proportional to voltage by Ohm's law. This region is more evident in gases and is sometimes indistinguishable from, or merged with, Region II for liquids (Castellanos 1998). Next, a region of low slope (Region II) exists where the current approaches saturation. Ionization dominates charge production, though a balance is achieved as the rate of charge recombination approaches the rate of dissociation. At higher electric fields (above 10 kV/cm), a steep increase of j with E is observed (Region III), where field emission takes place by charge injection at the liquid/metal interface. If the field is further increased (> 100 kV/cm), the dielectric strength of the fluid is exceeded and breakdown occurs (region IV). Dielectric breakdown is characterized by an uncontrolled avalanche of charges passing through the

dielectric medium and expelling a large amount of energy in the form of heat. Breakdown causes the destruction of the electrodes and an accumulation of particles (byproducts of high energy discharge). An experimental I-V curve allows the EHD operating regions to be distinguished, which helps one to prevent the device from operating in region IV. In addition, the I-V curve provides a way to extrapolate the emitter charge density boundary condition, as shown in Chapter 5.

In Regions I and II dissociated impurities can accumulate on the surface of the electrodes and change their work function, thus changing the emission process. Impurities are controlled by the double layer potential, which in turn is determined by the density and nature of absorbed ions. Charge behavior becomes complex quickly with any level of impurities, and extreme care needs to be taken to use pure working fluids to ensure stable and repeatable performance of EHD devices. Solid particles also get charged and are affected by fields within the fluid. They are either dragged along with the bulk fluid or are moved by the electric field. Once again, the purity of fluid is important for continuous and reliable operation of an EHD device, as solid particles can form small conductive bridges or reduce the distance between the electrodes, and thus lower the potential for dielectric breakdown.

2.4.4 Ion mobility

Equation (2-8) shows that the migration current density is proportional to the mobility of the unipolar charge. Experimental ion mobility measurements have been performed on various liquids for both positive and negative ions; however, different measurement methods and liquid purity states have resulted in significant inconsistencies (Schmidt 1990; Zhakin 2002). In addition, no data have been provided by 3M on HFE-

7100. Therefore, a method for estimating mobility is needed. Walden's rule can be applied to non-polar liquids. In this model, the ion is considered to be a charged sphere of radius R carrying an elementary charge through a viscous medium of viscosity μ . If it is assumed that the driving electric force applied to the charge carrier is equal to the viscous Stokes force exerted on a spherical ion of radius R , then mobility can be found from:

$$\mu_e = \frac{e_0}{6\pi R\mu} \quad (2-20)$$

where μ is the dynamic fluid viscosity. (Zhakin 2002) estimated the size of ions to be:

$$R = \left(\frac{3M_A}{4\pi\rho N_A} \right)^{1/3} \quad (2-21)$$

where M_A is the mass of the ion, ρ is the density of the bulk fluid, and N_A is Avogadro's number. For HFE-7100, $M_A = 250$ and $\rho = 1483 \text{ kg/m}^3$, so the mobility is approximately $\mu_e = 4 \cdot 10^{-9} \text{ m}^2/\text{V}\cdot\text{s}$.

2.4.5 Charge decay

Various researchers observed that space charge (injected electric charges present in the control volume) under the application of a constant field is not preserved permanently but decays over time (Watson 1996; Castellanos 1998). The rate of this decay is an important factor in the analysis of the EHD phenomenon because Coulombic force is directly proportional to the space charge. Thus, long charge decay times are desirable. This means that the EHD pumping mechanism can be assumed to be in a

steady state for as long as the electric body force acting on the charges does not vary much.

As the voltage on the emitter is increased, more charge is injected, increasing the current. However, the charge in the channel decreases the electric field between the electrodes, so that with increasing applied voltages a limiting current is reached, called the space charge limited current. In addition, some of the injected charge is not removed at the collector, but remains in the channel, lowering the current that can be obtained at a given voltage even further. (One solution to providing constant current is to continuously increase the voltage, but this leads to dielectric breakdown.) Impurities play a negative role in the process, hindering discharge (see section 4.8.3). Upon first turning on the device, therefore, the current decreases until a steady-state is reached, after which the free charge density in the channel presumably does not increase further. It is desirable to reach this steady-state current quickly, and to have it be as large as possible.

Charge decay process is not well understood; however, Castellanos provided two empirical cases for investigation: ohmic and unipolar charge injection regimes (Castellanos 1998). In the ohmic regime, the dimensionless charge density variation is expressed by the equation,

$$\rho_e^* = \rho_e^*(0) e^{\frac{-t^*}{\epsilon_r \text{Re}_e}} \quad (2-22)$$

Equation (2-22) shows that the electrical Reynolds number defines the decay time. Let us recall the definition of Reynolds number, $\text{Re}_e = \frac{\epsilon U_0}{\sigma_e L}$. From this it can be concluded that low electrical conductivity and high electrical permittivity slow down the charge decay process and thus improve EHD pumping.

For the unipolar charge injection regime it can be shown that charge density behaves according to the following equation (Castellanos 1998):

$$\rho_e^* = \frac{\rho_e^*(0)}{\left(1 + \frac{\tau_E}{\tau} t^*\right)} \quad (2-23)$$

After several decay times, the dimensionless charge density reaches a limiting

value $\rho_e^*(0) \frac{\tau}{\tau_E t^*}$, and the dimensional charge density approaches a limiting value $\varepsilon/\mu_e t$,

which is independent of the initial conditions. This indicates that charge decay is unavoidable even in the charge injection regime and has to be accounted for if DC power is used in the application of the EHD pumping device. Space charge effects played a role in our experimental results, as discussed in section 4.8.3.

2.4.6 Space charge limited current

Another nondimensional number, $C = \rho_{e,0} L / \varepsilon E$, characterizes two separate regimes of charge injection. Small values of C indicate that the electric field is determined by the external power supply and sometimes is called weak injection (Atten 1996). For large values of C (>1), the electric field is strongly dependent on the generated charges and is called space charge limited (SCL) injection. This means that the electric fields are distorted by the injected charge (electric field decreases with the increasing electric charge). SCL current (SCLC) is typically characterized by region III in the I-V current as shown in Section 2.4.2. The benefit of these empirical correlations is that, based on the nondimensional number C , it is possible to predict the behavior of the electric current and thus the input voltage at which injection regime starts. This

voltage onset point is an indication of the approximate minimum electric input operating conditions for the ion-drag pumping mechanism. Using $\tilde{n}_{e,0} = 10$, $L = 50 \text{ um}$, and $\epsilon_0 = 8.82 \times 10^{-12} \text{ F/m}$, $\epsilon_r = 7.39$, to obtain $C=1$ (at which SCL injection begins), a field of almost 1 MV/m is needed, which converts to a minimum input of 300 V.

In the unipolar injection case, charge behavior is governed by two equations: conservation of charge and Poisson's equation. Coupling them and solving them with the space charge field leads to a limiting current that has been shown to depend quadratically on the voltage applied to the electrodes. Castellanos derived the following expressions (Castellanos 1998).

- For planar electrodes a distance L apart, the SCLC density vs. voltage is

$$J = (9/8) \mu \epsilon V^2 / L^3 \quad (2-24)$$

- For point-plane electrodes with point electrode radius r_A , the SCLC vs. voltage is

$$I = (3\pi/2) \mu \epsilon V^2 / r_A \quad (2-25)$$

This equation can be used to estimate the size of SCLC in EHD micropumps having emitter electrodes with protrusions. For our designs, which had $0.1 \text{ }\mu\text{m}$ tip radii, the current was estimated to be on the order of $1 \text{ }\mu\text{A}$, which enabled us to size the power supplies to be used in the experiments.

2.4.7 Summary

The discussion in previous sections reveals that though a great deal of understanding already exists in the field of EHD, the physics of the phenomenon such as charge generation is still not complete. The tools that have been developed by earlier researchers allow the use of measured outputs, such as EHD current and electric field, to

estimate average values for charge generation and to predict general behaviors. A significant unknown is the charge boundary condition at the emitter electrode, and an empirical correlation needs to be derived for specific operating input conditions. These correlations will be dependent on bulk material electrical properties, which have not been fully explored as functions of operating system parameters such as established electric field and environmental conditions.

2.5 Literature review

EHD pumping has been investigated for over a century, and interest has not subsided. Many engineers have attempted to make working models due to the attractiveness of a readily controllable, noise-free, vibration-free pump without mechanical parts. Although the complexity of the EHD phenomenon has slowed progress in making these devices reliable, potential applications such as pumps, mixers, cooling systems, and even power thrusters are coming closer to commercial realization (Yu, Hallinani et al. 2002; Rada 2004).

This section provides an overview of several types of EHD pumps. This is followed by a presentation of the “big picture” of EHD pumping research to date. To conclude, a literature survey on numerical modeling of the EHD mechanism is presented.

2.5.1 Ion-drag pumps

Pumping mechanism

EHD pumping that relies solely on Coulombic body forces is called ion-drag pumping because it uses the electric field to “drag” the ions, which transfer some of their momentum to the bulk molecules and produce an overall pumping effect. The source for

these charges is injection of electrons at the liquid/electrode interface and their interaction with bulk molecules of the working fluid to produce ions.

Figure 2-2 shows a sketch of the working fluid, HFE7100, between emitter and collector electrodes. This simplified cartoon shows that injected electrons create a flux of negative ions that is larger than that of positive ions, thus providing a net charge flow from the emitter to the collector. In addition, neutral HFE7100 molecules get dragged along with the charges and produce a bulk liquid flow.

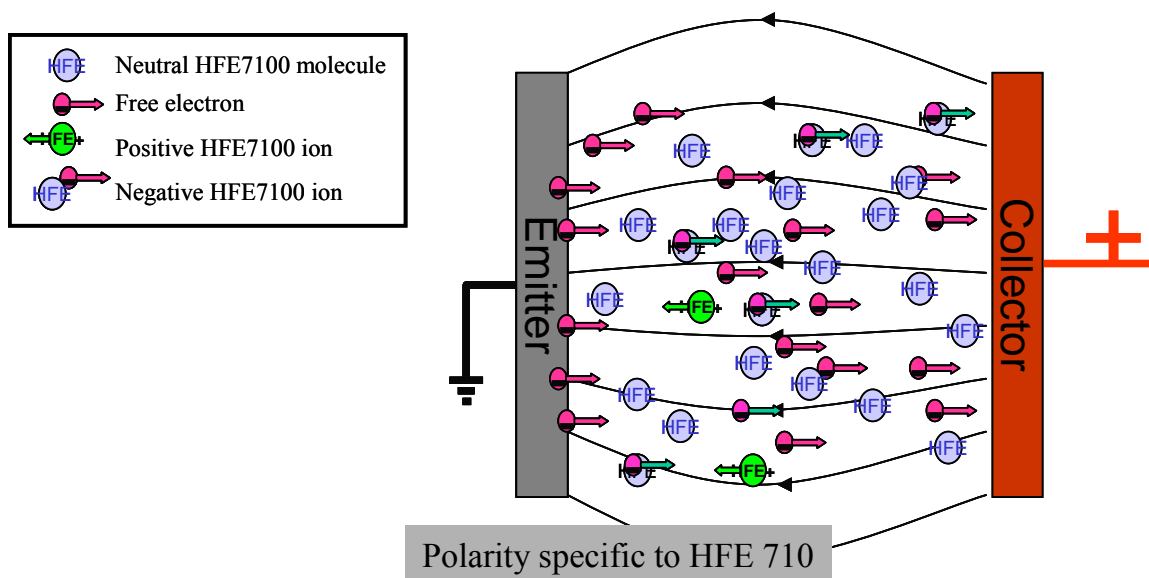


Figure 2-2 Ion-drag in HFE7100: negatively charged species drag neutral molecules to the right.

Ion-drag macro-scale pumps

The possibility for dielectric liquids to be pumped by electric fields has been known since the beginning of the twentieth century (Chattock 1901). This early work, however, was only conceptual and lacked complementary in-depth analysis or experimental support, which was performed some 50 years later by a group of scientists who produced innovative understanding of both the physical phenomenon and the potential applications.

First, Stuetzer studied ion-injection pressure generation in his classical paper (Stuetzer 1959), providing ample experimental work to support his analytical predictions. Stuetzer presented a unipolar model for three electrode geometries: plane, cylindrical, and spherical. His first paper concentrated on static pressure generation, but a year later he presented a dynamic case model as well (Stuetzer 1959; Stuetzer 1960). He was the first to present an I-V curve and define its regions. Later, his model was expanded by Schmidt (Schmidt 1997).

Work started by Stuetzer was complemented by Pickard (Pickard 1963), who derived a classical correlation between the EHD pump pressure and the electric field between two flat plate electrodes: $P = 9/8\epsilon E^2$. He investigated ion-drag theoretically and collected new experimental data for both static and dynamic cases.

Another influential study in the ion-drag pump field was performed by (Melcher 1981), who did extensive theoretical work on continuum electromechanics. He nondimensionalized all the EHD governing equations and introduced a new parameter, the electric Reynolds number. Melcher showed that in his DC voltage-operated pump, pressure and efficiency depended on the electric Reynolds number.

The first model of ion-drag pumps accounting for the material properties of the working liquid (viscosity, dielectric constant, and mobility) was proposed by Crowley et al. (Crowley, Wright et al. 1990). They presented a simplified model of the EHD pump considering contributions from all three charge flux components (convection, migration, and conduction). This work was an extension of Crowley's earlier studies on the efficiency of ion-drag pumps (Crowley 1980). Crowley and his colleagues concluded that the best flow rate performance could be achieved with high dielectric constant, low

viscosity fluids, while the efficiency could be increased by lowering the mobility and conductivity of the working fluid. Considering these findings and Walden's rule for mobility, liquids cannot operate at both maximum efficiency and flow rate, since the viscosity and mobility are inversely proportional.

During the nineties, there was much productive research on the development of ion-drag pumps. For his master's thesis Bryan designed a 10-stage ion-drag pump and tested it with fluids such as industrial oils, kerosene, and dodecylbenzene (Bryan and Seyed-Yagoobi 1990). Later, he tested many other commercial oils and refrigerants and obtained similar performances. One publication (Bryan and Seyed-Yagoobi 1992) reported the effects of multiple pump stages and working fluid doping. The authors concluded that electric current and pressure increased linearly with the number of stages. The maximum efficiency reported was 6%.

A comprehensive study on the effect of the electrode gap on the pump's static performance was performed by Coletti and his colleagues (Coletti and Bozzo 1996). They manufactured two metallic grids that were placed inside a 30 mm diameter polymethylmethacrylate (PMMA) housing. Tests were conducted with silicon oil, castor oil, and dodecylbenzene with input voltages of positive and negative polarities. Test results indicated that there was a difference in the pumping and electric current behavior in dodecylbenzene under different input voltage polarity. This was explained by the difference in the liquid's molecular and ionic composition. The pressure varied as $(1/d)^2$, where d is the electrode gap; however, this was applicable to negative polarity voltage only. Coletti et al. also investigated the dependence of the pressure head on applied electric potential $d\phi$. They found a quadratic dependence for silicon and castor oil;

however, dodecylbenzene displayed a more linear trend. This indicated that ion drag operation strongly depended on the working fluid's material properties, though the correlation between those properties and charge generation and distribution was not understood.

Russian scientists Zhakin and Lunev (Zhakin and Lunev 1998) presented a model for a two-dimensional EHD-pumped loop. Their work was not supported by experiments, but yielded a numerical model. Turbulence within the EHD device was discussed, and for two parallel electrodes embedded in the channel they proved the existence of a limiting value (channel height/electrode spacing = 0.3), above which turbulent flow begins. This model was investigated with large scale geometries (hydraulic diameter > 1 cm) and did not provide a discussion on microscale geometries.

Asano et al. (Asano and Yatsuzuka 1999) investigated an EHD pump with needle-cylinder electrodes. They used silicon oil, and they varied electrode geometries by punching variously sized holes in the collector and by putting needles on the emitter. A maximum static pressure of 300 mm (2.8 kPa) was achieved at 28 kV input voltage. This was the highest pressure achieved by an ion-drag pump to date. They also found that there is an optimum number of needles for best pump performance, thus indicating the need for optimization of the electrode designs.

For his doctoral thesis, Rada (Rada 2004) developed a meso-scale EHD pump that included two rings. The collector electrode had a smooth surface, while the emitter electrode had sharp needles around the perimeter of the ring. The pump was tested with the refrigerants R134 and HFE7100. Maximum static pressure heads of 160 Pa at 12 kV and 2 kPa at 30 kV were obtained for R134 and HFE7100, respectively. These input

voltages are significantly larger than those of the current micropump due to the several orders of magnitude larger electrode gaps. As expected, due to the low dielectric constant of LN₂, this did not result in high pressure heads or flow rates. However, a consistent flow of 0.8 g/s at 1 Pa pressure head was achieved.

Most of the papers on meso-scale pumps have not reported any data on, or have referred only minimally to, the reliability and repeatability of the experimental data. However, since the first EHD pump prototype (Stuetzer 1959), it has been known that certain intrinsic issues exist regarding the stability of EHD flows. In addition, the interaction of high electric fields with dielectric liquids unavoidably results in various electrochemical processes that change the surface properties of the electrodes and sometimes the chemical nature of the working fluid. The common practice has been to clean the electrodes after each test and to purify the working liquids before use (Pickard 1963; Castaneda and Seyed-Yagoobi 1991; Kojevnikov, Motorin et al. 2001). Sometimes such measures have been sufficient for large-scale systems (on the order of centimeters and larger), but smaller geometries and increased pump operation times have resulted in decreased performance and sometimes damaged pumps. Bologna (Bologna, Kozhukhar et al. 1993) performed service life tests with an ion-drag pump. They used kerosene, transformer oil, and polymethylsiloxane-5 (PMS-5). The liquids were purified by degassing and filtering, and results with these were compared to results from a sample of unpurified liquid. They found that after 200 hours of operation, the pump's performance began to decrease for the purified liquids. Performance decreased gradually at first, but eventually gained momentum, with loss in pumping power at an exponential rate past the 1000-hour mark. Non-filtered pump liquids performed differently,

producing diminishing pressure head from the beginning of the test and sometimes displaying sudden jumps in pumping. An investigation of the micropump EHD reliability phenomenon is offered in Chapter 4, section 4.8.

Ion-drag micro-scale pumps

A strong motive for decreasing the size of EHD ion-drag pumps has been known since their inception: a decrease in the electrode gap produces better performance and drives the operating voltage down. However, producing electrode geometries and spacing in the sub-millimeter range was not possible until the development of microfabrication technologies in the mid-eighties.

Credit for the first micro-scale EHD pump is owed to (Richter and Sandmaier 1990), who fabricated electrode grids on a silicon substrate with orifice diameters from 90 to 160 μm , grid thicknesses of 35 μm , and electrodes plated with gold. Electrode grid spacings were fixed distances of 10 μm and 60 μm . A maximum static pressure of 1200 Pa with ethanol as the working fluid was achieved with an input voltage of 300 V. Such a small input voltage was due to relatively high working fluid conductivity and small electrode gaps. Static pressure was comparable to the pressure obtained with the current pump. Richter proposed using this pump as a flow meter by recording the time of flight method for injected charges.

Sandia National Laboratory researchers (Wong, Chu et al. 1995) used laser micromachining to develop a micro-EHD pump. They produced two designs. The first one had two silicon substrates with gold layers stacked on top of each other, and fluid channels were drilled with a laser. The second design had silicon grids manufactured and attached back-to-back, which reduced the electrode distances to about 100 μm . A static

pressure head of 290 Pa was obtained with an input voltage of 120 V. To date it was the lowest input voltage used for a sensible pump's performance and is only about an order of magnitude of the power levels provides by a typical battery.

The first planar EHD micropump was developed by Ahn and Kim (Ahn and Kim 1998). They microfabricated an array of gold electrodes on a glass substrate. The electrode spacing was fixed at 100 μm , and the distance between the electrode stages was set to 200 μm . Ethyl alcohol was the working fluid. Two channel heights were used: 100 μm and 200 μm . The static pressure head was found to depend on the channel height (a maximum value of 220 Pa was achieved at 110 V). Flow rate was also measured and found to be strongly dependent on the channel height. A maximum value of 50 $\mu\text{l}/\text{min}$ was achieved for 110 V and 1 mA current. They reported the occurrence of dielectric breakdown close to 100 V but did not provide any in-depth comment or investigation of this reliability-affecting phenomenon.

Darabi (Darabi, Rada et al. 2002) reported fabrication and testing of an EHD ion-injection micropump. In their design, electrodes was deposited and patterned on a ceramic substrate. An epoxy gasket was used as the side-wall, and inlet and outlet ports were located on the top cover. Four different electrode designs were fabricated. The first design had rectangular electrodes, a gap of 50 μm , and a distance between stages of 100 μm . The second had a saw-tooth shaped emitter electrode and a rectangular collector, with the same electrode distances as the first. The third shared the same shape as the second, but with electrode gaps twice as wide. The fourth was identical to the third with the exception of the inclusion of 3D bumps along the emitter electrode. Static pressure tests were performed with HFE-7100. A pumping head of up to 700 Pa at an applied

voltage of 300 V was obtained for the fourth design (the best performer). Only static pressure measurements were reported in this work.

Taiwanese researcher Yang fabricated and tested another ion-drag micropump using indium-tin-oxide (ITO) planar electrodes (Yang, Wang et al. 2003). The ITO on glass enabled him to package the pump using anodic bonding to a silicon wafer with microchannels. A flow rate of 87 nl/min at 40 V DC was obtained; however, there were serious issues concerning repeatability and reliability.

Table 2-2 presents a short summary of the prior work. Both macro- and micro-scale pumps are listed. Since almost none of the data reported on the pumps' performances included uncertainty of the measurements, a separate column indicates whether any notion of repeatability and reliability was provided in the respective reports.

Table 2-2 Summary of ion-drag pump experimental works (only selected information is listed).

Reference	Fluid(s)	Electrode Geometry	Inter-electrode gap size	Maximum Efficiency	Flow rate/ Pressure drop (for static case)	Applied voltage	Repeatability/reliability issues
(Stuetzer 1960)	Kerosene, castor oil	Needle emitter, ring collector	0.6-10 mm	5%	Not reported/1.6 kPa	Up to 30 kV	±25% repeatability; electrochemical degradation of liquid reported
(Pickard 1963)	Acetone	Molybdenum parallel wires embedded onto a plastic ring	2.5-15 mm	Not reported	0.17 cm/s; 2 kPa	Up to 10 kV	Pretreated fluid by careful filtering and chemical purification; no reference to experimental tests
(Bryan and Seyed-Yagoobi 1990)	Dodecylbenzene	Emitter: Ring with needles; Col: Rings with and without wire mesh	5 mm	6%	33.4 cm/s; 112 Pa (10 stages)	Up to 25 kV	Not Reported
(Castaneda and Seyed-Yagoobi 1991)	Refrigerant R11	Tin-copper wires embedded into flow tube	8 mm	4 %	20 cm/s / 50 Pa (13 stages)	Up to 25 kV	Not Reported
(Richter, Plettner et al. 1991)	Ethanol	Micro-grids mesh for emitter and collector	350 μm	Not reported	14 ml/min/2.5 kPa	Up to 700 V	Not Reported
(Barbini and Coletti 1995)	Silicon oil, castor oil, dodecylbenzene	Emitter: circular drilled disk; Col: 1)circular mesh, 2) drilled disk	0.5-3.5 mm	N/A	N/A/ Up to 600 Pa	Up to 37 kV	Not Reported
(Wong, Chu et al. 1995)	Propanol	Both electrodes were microfabricated grids	330 μm, 178μm, 127μm	N/A	N/A/300 Pa	Up to 100 V	Not Reported
(Ahn and Kim 1998)	Channel height: 100 μm & 200 μm Channel width: 3 mm	Microfabricated rectangular strips (planar dimension)	100 μm	~0.1 %	50 μl/min/ 200 Pa	Up to 100 V	Not Reported

(Asano and Yatsuzuka 1999)	Silicone oil	Needles-cylinder	2-8 mm	N/A	N/A; 300 Pa	Up to 30 kV	Not Reported
(Bologa, Kozhevnikov et al. 2000)	Transformer oil ($\sigma \sim 10^{-11} \Omega^{-1} \text{cm}^{-1}$)	Metal wire mesh	3 and 4 mm	6%	600 ml/s/10kPa (with 27 stages)	Up to 18 kV	Purified liquid with electric field; mentioned incomplete charge recombination at the collector; found residue on collectors after test
(Yanada, Hakama et al. 2002)	Mineral oils and silicone oil	Needle-mesh	2,4, 6 mm	5%	40 ml/s; 400 Pa	Up to 30 kV	Not Reported
(Darabi, Rada et al. 2002)	HFE-7100	Planar, saw-tooth, and saw-tooth with bumps	50 μm , 100 μm	N/A	N/A; 800 Pa	700 V	Not Reported
(Yang, Wang et al. 2003)	Ethanol	Indium-tin-oxide (ITO) rectangular and planar	80 μm	Not reported	Up to 100 nl/min; Not reported	Up to 100 V	No repeatability of data; strong liquid breakdown issues; no solution offered
(Shooshtari 2004)	HFE-7100	Microfabricated grids	250 μm	0.5 %	270 Pa	Up to 1.5 kV	Degassed liquid before experimentation; used research grade liquid

2.5.2 Other EHD pumps

For completeness, other types of EDH pumps are described here. These phenomena also occur in ion drag pumps, but to a lesser extent.

2.5.2.1 Conduction pumps

Pumping mechanism

Conduction pumps utilize dielectric liquids of low electrical conductivity ($\sigma_e < 10^{-7}$ S/m), and they rely on the creation of a heterocharge layer near the electrode surface produced through the dissociation of neutral molecules. The heterocharge layer consists of a layer several Å thick of charges of opposite polarity from that of the electrode. (Conductive liquids have an electric double layer (EDL) that is identified by the Debye length λ_D .)

As discussed earlier, Coulomb force vanishes in the bulk of the liquid, which is electrically neutral. However, Coulomb forces act on the heterocharge layer. Clever arrangement of the electrode geometry and the prevention of field injection can increase the pumping head.

Literature review of conduction pumping

Conduction pumping has been proposed and developed by Atten et al. (Atten and Seyed-Yagoobi 2003). The conduction pump designed by Seyed-Yagoobi provided pumping heads of up to several hundred Pascals. As the input voltage was increased, transition to the ion-injection regime was observed by shifting of the electric current from linear to exponential dependence on the input voltage, which is well in agreement with the predicted I-V characteristic curve. Seyed-Yagoobi (Seyed-Yagoobi and Bryan 2003)

have filed a patent to protect their intellectual rights to the conduction pump concept and design.

2.5.2.2 Induction pumps

Pumping mechanism

Induction pumping relies on dielectrophoretic force, as described in Section 2.2.2. Typically, a traveling wave is used to establish a non-uniform electric field. In addition, a gradient of fluid permittivity or conductivity is needed. Typically, fluids do not possess such variations, but artificially stratifying liquids that do not mix, imposing a temperature gradient, producing a two-phase system, or seeding the fluid with particles can produce the desired gradients.

Review of existing work

The classic paper by (Melcher and Firebaugh 1967) established the principles of traveling wave-induced charges in a liquid with a permittivity and/or conductivity gradient at the liquid surface or within the bulk of the fluid. Under certain conditions these charges can be set into motion and transfer momentum to the rest of the fluid.

Bart et al. (Bart, Tavrow et al. 1990) designed and tested microfabricated pumps with a traveling wave. For the system to work, every third electrode was connected to the same vertical bus line to form a three-phase electrode system. Using silicon oil as the working liquid, a 1-kHz traveling wave of 200 V peak-to-peak propelled the fluid at a maximum of 9 mm/s with a channel depth of 20 μm .

Several other investigations on induction pumping have also been reported. Kashani (Kashani, Kang et al. 2000) produced another micro-induction pump, while Seyed-Yagoobi investigated induction pumping with two-phase fluid applications

(Seyed-Yagoobi 2002). He patented various electrode designs for optimum EHD induction pumping and thermal energy transfer (Seyed-Yagoobi and Brand 2001).

It should be noted that induction pumping, due to its limited applicability to two-phase non-isothermal systems, is not a direct competitor to ion-drag pumping, which can typically operate only with single-phase and isothermal fluids. However, understanding of all the EHD mechanisms is essential to an engineer working with various test setups and device geometries, since all three EHD mechanisms can be present.

2.5.2.3 Electrokinetic pumps

Pumping mechanism

In electrokinetic pumping, electrophoretic forces act on ions within the electric double layer (EDL) generated in an electrolyte solution. Two subsets of electrokinetic motion can be analyzed: *electrophoresis*, which is typically used for separation of biochemical species based on electrophoretic mobility (mass-to-charge ratio), and *electro-osmosis*, which generates motion in electrolytic solutions near the surface. The double-layer structure can be described by several models (Stern, Gouy-Chapman). Based on Stern's work, the electrokinetic velocity is, in simplified form:

$$\mathbf{u} = \frac{\varepsilon \mathbf{E} \zeta}{\eta} \quad (2-26)$$

where ε is permittivity, \mathbf{E} the electric field, ζ the zeta potential, and η the viscosity. This equation indicates that in addition to the proportionality of the flow to the dielectric fluid constant and applied electric field, electrokinetic pumping also relies on a property called the zeta potential.

Electrokinetic pumps

This is a rich area of research, and only a comparatively short summary of electrokinetic pump performance can be given here. For microchannel electroosmotic pumps, flow rates in the range from 0.55 to 0.2 $\mu\text{l}/\text{min}$ have been achieved at pressure heads reaching 20 MPa (Ramos, Gonzalez et al. 2001; Scott, Kaler et al. 2001; Zeng and Chen 2001). Significantly higher flow rates, but with lower pressure heads, could be achieved by fabricating electrokinetic micropumps with porous media. Flow rates of up to 7 ml/min and dynamic heads up to 250 Pa have been reported (Zeng and Chen 2001).

2.6 Summary

This chapter provided an overview of the complex EHD mechanism with specific application to ion-drag pumping. First, starting with Maxwell's equations, a set of equations were given that govern EHD body forces. Then, a specific model was derived for a non-polar dielectric liquid subject to an uniform external electric field. Further assuming unipolar injection with ohmic conduction, coupling of the charge conservation law with the Navier-Stokes equations led to the final set of equations applicable to ion-drag pumping.

In the next section, the behavior of the electric charge under the influence of electric fields was briefly summarized. Charge mobility, polar vs. non-polar fluids, space-charge limited current (SCLC), and charge behavior over time were introduced. These concepts, along with the characteristic I-V (current-voltage) curve, the ion-injection mechanism, and charge generation models help to better understand the fundamentals of the ion-drag pumping mechanism. This knowledge was then schematically applied to the specific problem investigated in the current study, ion-drag pumping mechanism of 3HFE7100, a non-polar dielectric liquid.

Next, a literature review was offered for the better understanding of the experimental work performed in the field. A transition occurred from the large-scale EHD pumping systems of the 1960s - 1980s towards miniaturized systems in the early 1990s due to the availability of microfabrication technologies. The potential benefits of smaller EHD pumps include reduced power consumption, mass-fabrication, wafer-scale packaging, and lower cost. The literature review, however, indicated that challenges associated with electrochemical processes on the electrodes have been abundant, but have rarely been investigated. Commercialization of EHD pumps has not been achieved, and more fundamental knowledge of the phenomenon is still needed. The chapter was completed with a table summarizing the previous work and a short literature review of several other, non-injection, EHD pumps.

CHAPTER 3 ION DRAG MICROPUMP DESIGN, FABRICATION, AND TESTING

3.1 Introduction

This chapter presents work done on the design, fabrication, and test setup for the ion-drag micropump. The goal of the present study is to identify, analyze, and evaluate the significance of selected geometrical design parameters on the pump's performance. To accomplish this goal, a series of electrode shapes, sizes, and separations was chosen. In addition, a microfabrication technique was selected to manufacture the pumps at the University of Maryland since commercial fabrication was too costly, although microfabrication at UMD put a practical limit on the shape and size of the electrodes. In addition, packaging for the pump was constructed with inline inlet and outlet ports and variable channel heights. A test loop capable of measuring the pump's performance under various static and dynamic conditions was also built. The test loop incorporated materials with minimized outgassing and the ability to hold a low vacuum, sensitive instrumentation for low current, differential pressure measurements. A computerized data acquisition system was set up to run the tests and record the output variables in real time.

Although ion-drag micropumps have been investigated by many researchers (Bart, Tavrow et al. 1990; Richter and Sandmaier 1990; Fuhr, Hagedorn et al. 1992; Wong, Chu et al. 1995; Ahn and Kim 1998; Darabi, Rada et al. 2002; Shooshtari 2004), the pumps have differed in their fabrication techniques, test settings, and geometry. None

of the previous studies examined the effects of geometrical design on a planar ion-drag micropump under static and dynamic flow conditions. Darabi's and Rada's work (Darabi, Rada et al. 2002), which served as the foundation for the current study, evaluated pump designs based only on static pressure tests, which, as the current work indicates, is not sufficient to fully characterize an EHD pump. Ahn's study of planar ion-drag pumps used only one type of electrode without any geometric enhancements, while this study introduced several electrode geometries with sharpened features like saw-teeth and overhangs. Others have reported work only with non-planar pumps (pumping active surface not inline with the flow field), but such pump designs are not well suited to the electronics applications where planar surfaces dominate. The present study aims to fill this gap in knowledge.

3.2 Micropump design

Historically, fabrication of ion-drag pumps was carried out with precision machining and involved various sharp-angled emitter electrodes (needles, edges, thin wires). Collector electrodes were typically made to be smooth (e.g., flat plates, dull edged metal mesh, and thick wire). Typical electrode gap sizes ranged from 1 millimeter to several centimeters, and emitter tips were made with radii of a few tens of micrometers. More recently, the availability of microfabrication techniques has enabled fabrication of ion-drag micropumps with much smaller feature sizes (Bart, Tavrow et al. 1990; Richter, Plettner et al. 1991). Two types of micropumps have emerged: planar (Ahn and Kim 1998) and grid-type (Richter, Plettner et al. 1991). The former consists of electrodes deposited on a planar surface, and the latter has grid electrodes perpendicular to the flow direction. The device made by Richter had grid holes down to 70 μm and

electrode spacing of several hundred micrometers (Richter, Plettner et al. 1991). Ahn and Kim built a planar pump with an electrode spacing of 100 μm and a channel height of similar dimensions (Ahn and Kim 1998). Pumps based on planar and grid electrodes are compared in Table 3-1.

Table 3-1 Comparison of planar and grid type ion-drag micropumps.

	Planar Pumps	Grid Based Pumps
Pressure drop	Is mainly a function of channel height.	Depends on grid density, shape, and surface roughness.
Flow rate	Generated by electric shear stress acting on the fluid propagated through the boundary layer.	Generated by electric body forces acting on a fluid bulk cross-section.
Microfabrication	Simple photolithography techniques such as thin film deposition.	More complex, involves etching of holes and cavities in bulk silicon.
Electrode geometry	Limited emitter features size and shapes (maximum protrusions are several μm). Example shapes: planar saw-tooth, lines, overhangs, bumps.	Limited by microfabrication techniques. Protrusion sizes are on the order of the substrate thickness (500 μm for standard silicon wafers).
Applications	Where planar (or curved planar) mounted surfaces are needed: electronics components, microfluidics.	Better suited for larger (> 1 mm) diameter channels with low aspect ratio: small pipes, condenser channels.

The pump chosen for this study was a planar type for both application and fabrication related reasons. First, to achieve microscale, chip-integrated cooling systems the substrate must be mounted flat onto the electronic component. Second, the simpler fabrication leads to a higher prototype yield, making in-house fabrication of different

design prototypes possible. Pump design consisted of three stages: selection of materials and fabrication technique, geometrical design of electrodes and packaging, and creation of the micropump flow channel with interconnects, each of which will now be described in detail.

3.2.1 Fabrication method and material selection

To pattern the electrodes, thin films of metal were deposited, masked with photoresist patterned photolithographically, and wet chemically etched. In-house fabrication facilities enabled rapid pump prototyping at a small fraction of the cost needed for similar commercial orders. On the other hand, fabrication tolerances and yield were lower because the university microfabrication lab cannot achieve state-of-the-art commercial foundry fabrication results. However, this did not compromise the goals of the current study.

Micropump device materials selection guidelines

Materials and typical sizes/geometries were selected for the three parts that make up the ion-drag micropump: substrate, electrodes, and fluid channel walls. The selection of these materials was dictated by the following factors: the EHD phenomenon, fabrication technology, and the micropump application. The constraints are summarized in Table 3-2. Based on these considerations, the choices outlined in the following sections were made.

Table 3-2 Factors influencing the selection of micropump 1) material and 2) geometry.

	Influencing factor		
	EHD phenomenon	Fabrication technology	Pump application (micropump/microevaporator)
Substrate	1) Electrical insulator for isolation of the metallic electrodes, minimum outgassing. 2) N/A	1) Any material that wicks with photoresist 2) Smooth surface and low aspect ratio (thickness/diameter) for photoresist spinning.	1) Thermal conductor (for best heat removal). 2) Flat for electronic surfaces, flexible for non-flat heat sources.
Electrodes	1) Metal for electron injection; metals resistant to electrochemical processes preferred for reduced corrosion. 2) Micron-size electrode distances, maximum height and sharp angle protrusions for creation of high electric fields.	1) Metals, semiconductors, insulators. 2) Thin films are several μm thick, maximum; metal thickness is controlled by intrinsic stresses.	1) Low electrical resistivity for minimal power consumption and Joule heating. 2) Lower electrode height imposes less pressure drop in the channel.
Channel walls	1) Non-conducting, degassed materials. 2) N/A	1) N/A 2) If made by microfabrication, limits are several hundred μm .	1) N/A 2) Optimized height to minimize the pressure drop and keep the pump dimensions small.

Electrodes

Gold and platinum are noble metals, and hence resistant to corrosive electrochemical processes. Electrochemical potentials for some common electrode reactions are listed in Table 3-3 vs. SHE (the standard hydrogen electrode). Gold has the highest potential for oxidation (corrosion) compared to other metals. However, during EHD pumping the fields are so high that corrosion processes cannot be eliminated.

Metal electrodes were made from chromium/gold thin films. Chromium is needed to adhere gold to the substrate. Platinum was also tested, but it turned out to be too challenging for in-house fabrication, resulting in a low yield of working prototypes. Fabrication challenges, during various stages of the study, were associated with both metal deposition (cracks, blistering, and poor adhesion), and patterning (incomplete etching, thin metal bridges between electrodes, and “wings” on the electrode edges after lift-off). Platinum is also almost twice as expensive as gold.

Table 3-3 Electrode potential for several common elements with respect to the hydrogen reference reaction (eFunda 2005).

Element	Reaction	Electrode Potential (V)
Gold	$\text{Au}^+ + e^- \leftrightarrow \text{Au}$	1.692
Platinum	$\text{Pt}^{2+} + 2 e^- \leftrightarrow \text{Pt}$	1.18
Silver	$\text{Ag}^+ + e^- \leftrightarrow \text{Ag}$	0.695
Copper	$\text{Cu}^{2+} + 2 e^- \leftrightarrow \text{Cu}$	0.521
<i>Hydrogen</i>	$H^{2+} + 2 e^- \leftrightarrow H_2$	0
Aluminum	$\text{Al}^{3+} + 3 e^- \leftrightarrow \text{Al}$	-1.662

The second consideration for electrode material is the ability of the metal to inject charges, since the electric body force is proportional to this charge. Emission charge density is a function of the metal work function. Fowler and Nordheim showed that current density is given by (Fowler 1928):

$$J(E) = 1.545 \times 10^{-6} \frac{\beta^2 E^2}{\phi} \exp\left[-6.83 \times 10^7 \frac{\phi^{\frac{3}{2}}}{\beta E}\right]$$

(3-1)

where ϕ (eV) is the work function of the metal, E is the electric field strength, and β is a field enhancement factor that is closely related to electrode geometry. Equation (3-1) indicated that the smaller the work function, the less energy is needed to remove electrons from the electrode surface. Table 3-4 lists work functions for several materials typically used in thin film fabrication processes.

Table 3-4 Work functions of several common metals (eFunda 2005).

Metal	Pt	Au	Cu	Cr	Nb	Al
Work function (eV)	5.65	5.1	4.7	4.5	4.3	4.28

The less expensive aluminum and niobium are better in this respect, but their favorable electron emission is outweighed by their corrosiveness. This was confirmed experimentally in this study. Electrodes made from Al and Nb had little resistance to corrosive electrochemistry. (Niobium was also used in the micropumps built by the commercial foundry at TRW for Darabi's work (Darabi, Rada et al. 2002).)

Pump Substrate

Two substrates were considered. One was oxidized silicon, chosen for its smoothness and widespread use in the commercial semiconductor industry. Silicon also has a relatively high thermal conductivity. The other was alumina, which is a non-conducting ceramic with higher durability than silicon. Alumina (Al_2O_3) substrates were purchased from Coorstek, Inc, (Golden, CO) in 1x 0.5" sample sizes. They were polished to two different surface roughnesses: 0.2 μm (commercial name ADS-995), and 0.02 μm (commercial name ADS-996).

Fluid Channel

Fluid channels can be created by either one of two techniques: microfabrication or machining. For a planar micropump, the substrate has, at least initially, to be flat for electrode fabrication; later, channel walls can be added over the electrodes, or the substrate can be bonded to another one with channels. (Flexible substrates could possibly be rolled or molded into some other closed shape to produce channels.) For the current study, the simpler and less costly method (for prototyping and basic studies) of machining was chosen. The top layer plate provided machined fluid inlet and outlet ports, and it was attached to the substrate by gluing and/or clamping.

Working fluid selection

As mentioned before, the current study used a 3M[®] manufactured methoxy-nonafluorobutane working fluid with the chemical formula $C_4F_9OCH_3$ and brand name of HFE-7100. This substance is a clear, colorless, nonflammable, and low-odor dielectric liquid with low toxicity. Compared to many hydrofluorocarbons (HFCs), the global warming potential (GWP) of HFE-7100 is low, and as a result HFE-7100 is a more environment-friendly choice than most other HFC refrigerants. The main advantages of this liquid are its relatively high dielectric constant (7.39) and low electrical conductivity ($\sim 3.0 \times 10^{-10} \Omega^{-1}cm^{-1}$). As explained in Chapter 2, a higher dielectric constant leads to a higher pumping head, while a lower electrical conductivity results in a higher efficiency. HFE-7100 is a liquid at atmospheric pressure, and therefore there is no need to keep the test loop at high pressure, as is the case with typical refrigerants. The boiling temperature of this liquid at atmospheric pressure is 61 °C. HFE-7100 is a poor thermal conductor. For example, the specific heat of HFE7100 is almost three times lower than that of water.

(Unfortunately, the high electrical conductivity of water makes it unsuitable for ion-drag pumping. In addition, water is highly corrosive.) Table 3-5 presents a comparison of the physical properties of HFE-7100, water, the common refrigerant R123, and liquid nitrogen.

Table 3-5 Physical properties of HFE-7100 in comparison with a number of other liquids.*

Property	HFE-7100	Water	R-123	LN2
Molecular Weight, g/mol	250	18	152.9	28
Density (kg/m ³)	1480	997	1464	810.6
Dynamic Viscosity (kg/m-s)	6.51×10^{-4}	9.93×10^{-6}	4.09×10^{-4}	1.67×10^{-4}
Thermal Conductivity (W/m-K)	0.069	0.595	0.077	0.139
Specific Heat (J/kg-K)	1180	4183	1035	2038
Boling Point (C)	61	100	27.8	-195.8
Heat of Vaporization @ B.P. (kJ/kg)	111.6	2257	229	198.8
Surface Tension (N/m)	0.0136	0.072	0.015	0.009
Vapor Pressure (Pa) @ 25 C	26,931	3,169	91,477	N/A
Dielectric Constant	7.39	80	4.5	1.43
Resistivity (Ω cm)	3.29×10^9	1.0×10^6	1.47×10^{12}	_____
Ion Mobility (cm ² /V-sec)[Calculated using Walden's Rule and $R = 1 \times 10^{-9}$]	1.31×10^{-8}	8.5×10^{-7}	2.08×10^{-8}	5.09×10^{-8}

*All values are determined at 25 °C except for LN2, for which properties are given at 77 K.

The molecular structure of HFE-7100 is shown in Figure 3-1. The molecule can fragment upon ionization into $-\text{CH}_3$, $-\text{OCH}_3$, and $-(\text{CF}_2)_n\text{CF}_3$ ions.

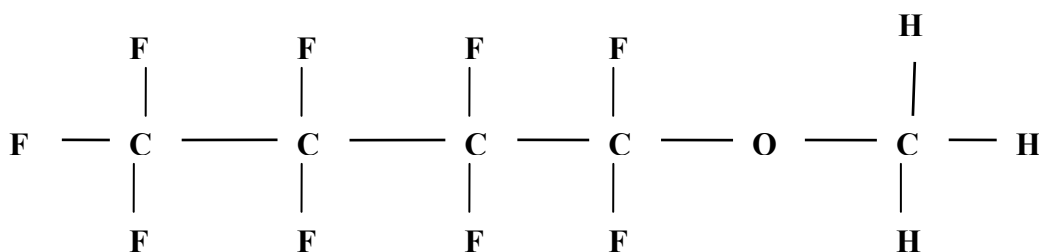


Figure 3-1 Chemical structure of HFE-7100 (C₄F₉OCH₃).

3.2.2 Electrode geometries

Micropump electrodes were designed to try to improve pump performance. Charge injection and the electric body force both depend on the maximum electric field, which is determined by pump geometry once the materials are fixed. Using various geometrical shapes and varying the distance between the electrodes, it is possible to significantly influence the magnitude and direction of the electric field.

One way to increase the electric field, for a fixed applied voltage, is to reduce the distance between emitter and collector electrodes. A second way to significantly increase the electric field is to create sharp-angled protrusions on the electrodes. Because the electric field on a boundary is equal to the gradient of potential field on it, higher curvature tips produce larger fields. Note that curvature $\kappa = 1/R$, where R is the radius of curvature. Using microfabrication techniques, the radius of curvature can be on the order of nanometers and yield electric fields of a few megavolts per meter.

The base case for this study was a pump with the design geometry of strip electrodes emerging from two parallel buses at different potentials, since it was the easiest to model. Further iterations of the electrode design are compared to this one.

With boosting the electrical field in mind, Darabi and Rada used saw-tooth-shaped electrodes for the emitter. They also planned to make saw-teeth that were partially raised off the surface, dubbed overhang electrodes, as illustrated in Figure 3-2. They out-sourced electrode fabrication to a commercial foundry. Fabrication of the overhang electrodes in Darabi's study did not succeed, but was successfully achieved in the current study.

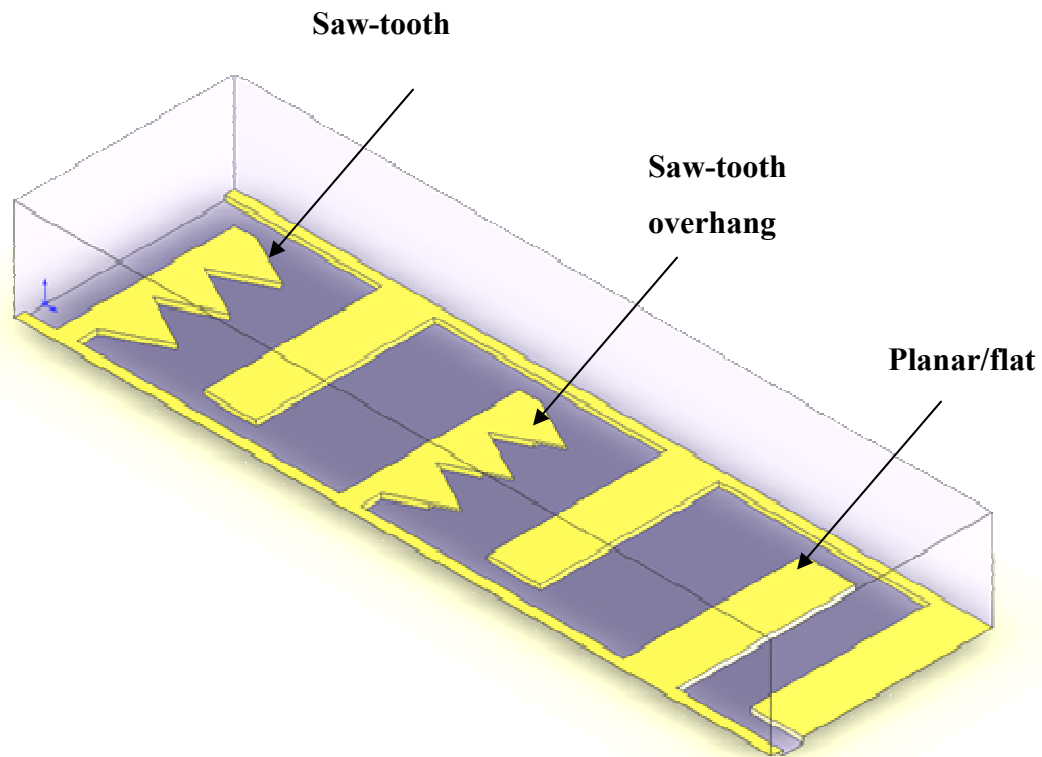


Figure 3-2 A sketch of three pump electrode designs: planar/flat, saw-tooth, and saw-tooth with overhang.

For each of the geometries, the spacing between the electrodes and electrode pairs was varied. For the saw-tooth electrodes, two values were tested for the tip angle: 53° and 26° . As there had been no prior investigation of geometrical design parameters, these variables were selected based on an in-depth literature review and insight gained from the

expressions for the EHD phenomenon (Chapter 2). Several other geometries were investigated in numerical modeling only: flat overhangs, bumps, and trenches.

Once the electrode geometries were chosen, they were drawn into AutoCAD so that masks could be ordered for the microfabrication process, following design rules specified by the mask manufacturer. A typical drafted design is shown in Figure 3-3. The tightly spaced electrode strips make up the dark middle block. The two rectangular legs are for input power connections. Letter and number codes (explained in chapter 4) on the top of each pump indicate its design type. The mask we purchased was a soda-lime glass plate with the desired patterns transferred to a film of chromium, either a replica of the drawing (positive mask) or its negative (negative mask, dark and light inverted).

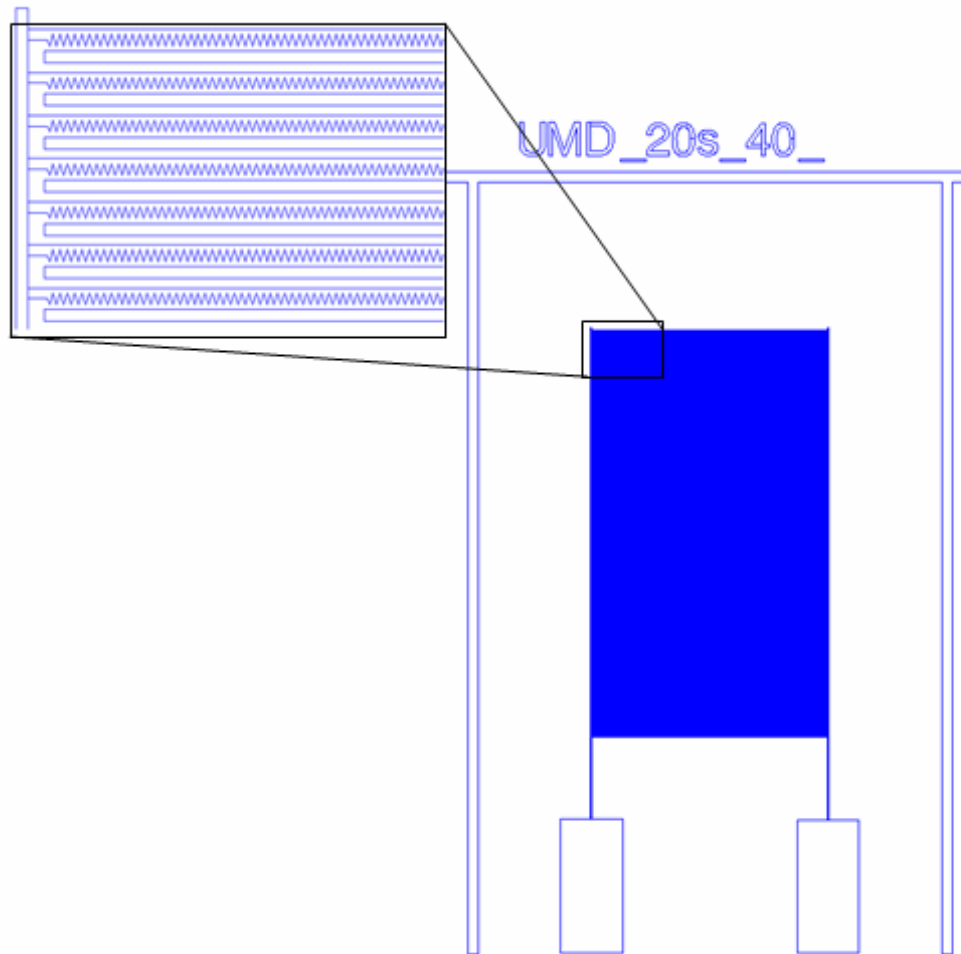


Figure 3-3 Photolithography mask drawing prepared in AutoCAD and labeled with identifying codes. Eight designs were fabricated in total.

3.2.3 Channel height considerations

The fluid channel then had to be designed to complete the pump. For the dynamic case, the depth of the channel is one of the most important parameters in determining the flow. For the applications of interest, final packaged sizes on the order of several millimeters are needed. The expressions describing the EHD phenomenon indicate that the charge boundary layer, which creates the pumping force, will be most effective for a channel depth of several hundred micrometers. As shown in Chapter 5, greater depths reduce the effectiveness of the force transfer to the bulk flow, and may even induce

recirculation. Channel heights of $< 50 \mu\text{m}$ or so result in increased internal pressure drops, making it impossible for the pump to generate significant flow.

3.3 Micropump fabrication

Several iterations of the pump design were chosen for microfabrication. A commercial foundry (TRW, Inc.) was used to produce the first prototypes. However, due to long their turn-around time (4-6 weeks) and high cost (several hundred \$US per pump), later prototypes were made at the university. Proper training and hours of experimentation quickly paid off as fabrication of electrodes sped up (1-2 days per pump) and costs went down (20-50 \$US per pump).

Switching to a local microfabrication facility also brought microfabrication knowledge and skills to the author of this study, while enabling him to have more control over the fabrication. These benefits came, however, at the cost of working with less expensive masks having larger dimensions, increasing the minimum feature size of the electrodes, and working in a dirtier cleanroom without automated equipment, thus decreasing yield due to human error. TRW, Inc. could potentially have fabricated electrodes with 0.5-1 μm electrode spacing, which would have enabled micropump operation at battery voltages. In the university fabrication lab, only 10 μm spacing was reliably achieved, although 5 μm features were occasionally achieved.

Three workflows were used in fabricating the micropump electrode designs: for flat and saw-tooth electrodes, wet etching using a positive mask and lift-off using a negative mask were both used, and for the overhang electrodes two different positive mask processes were used. The workflows are shown schematically in Figure 3-5, Figure 3-6, and Figure 3-7. An in-depth description of the materials used and precise fabrication

recipes are given in Appendix A. The major steps of a typical workflow wet etch process are as follows.

- 1) Cleaning the substrate.
- 2) Depositing a thin adhesion layer of chromium and a thicker film of gold on top of that.
- 3) Spinning a layer of photoresist over the gold.
- 4) Exposing the photoresist to ultraviolet (UV) light through the mask.
- 5) Developing (removing) the exposed photoresist.
- 6) Etching the metals using commercial wet etchants for gold and chromium.
- 7) Removing the residual photoresist.

This sequence of work produced pumping surfaces as shown in Figure 3-4 with an array of electrodes (one corner patch is magnified in the bubble), electrode connection pads, and a pump design code indicating the spacing between electrodes and electrode pairs as well as the shape of the emitting electrode.

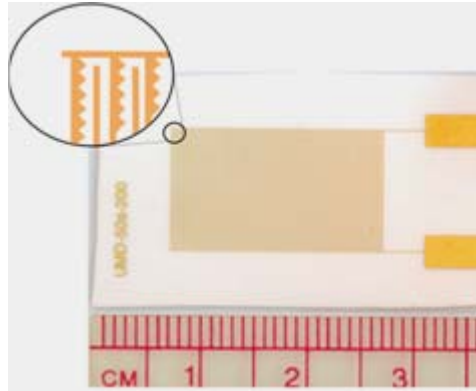


Figure 3-4 Sample of micropump substrate with the electrodes.

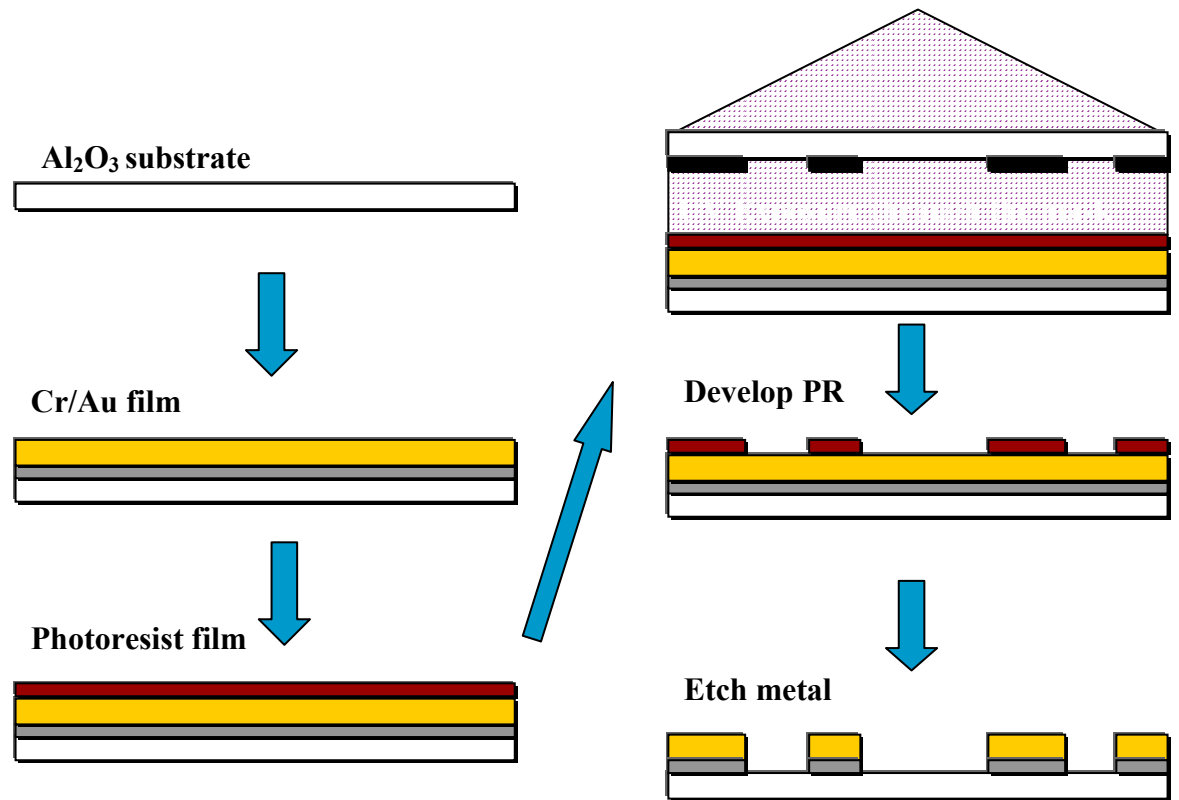


Figure 3-5 Positive mask fabrication workflow for one level electrodes.

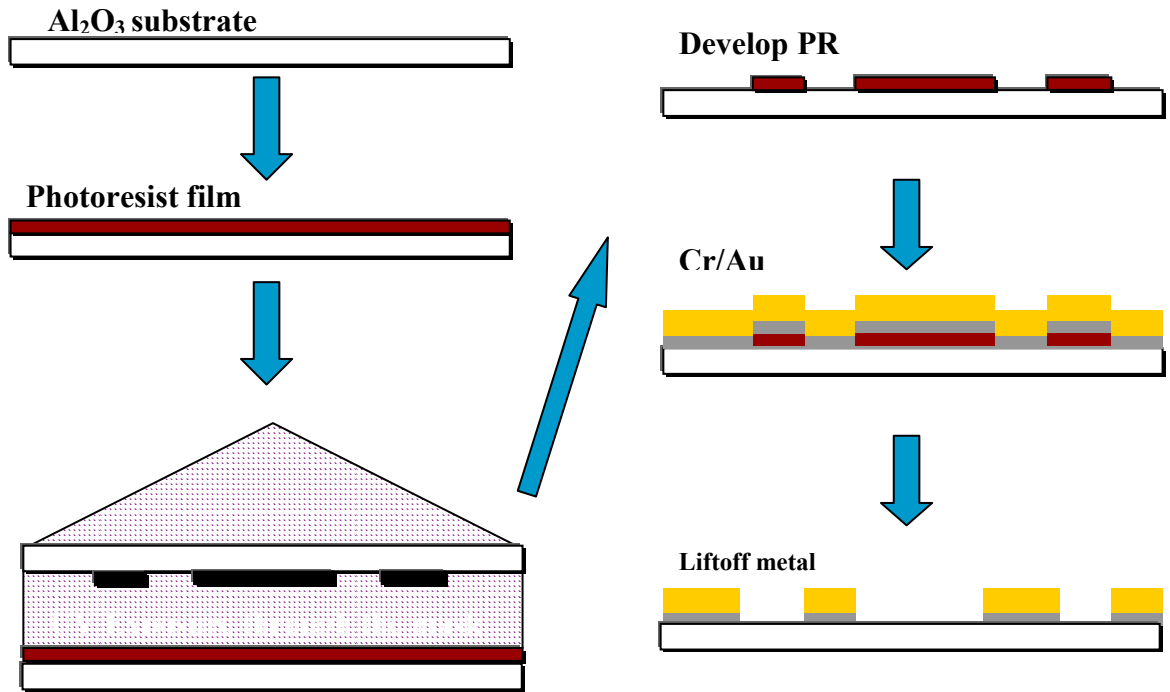


Figure 3-6 Negative mask electrode fabrication workflow.

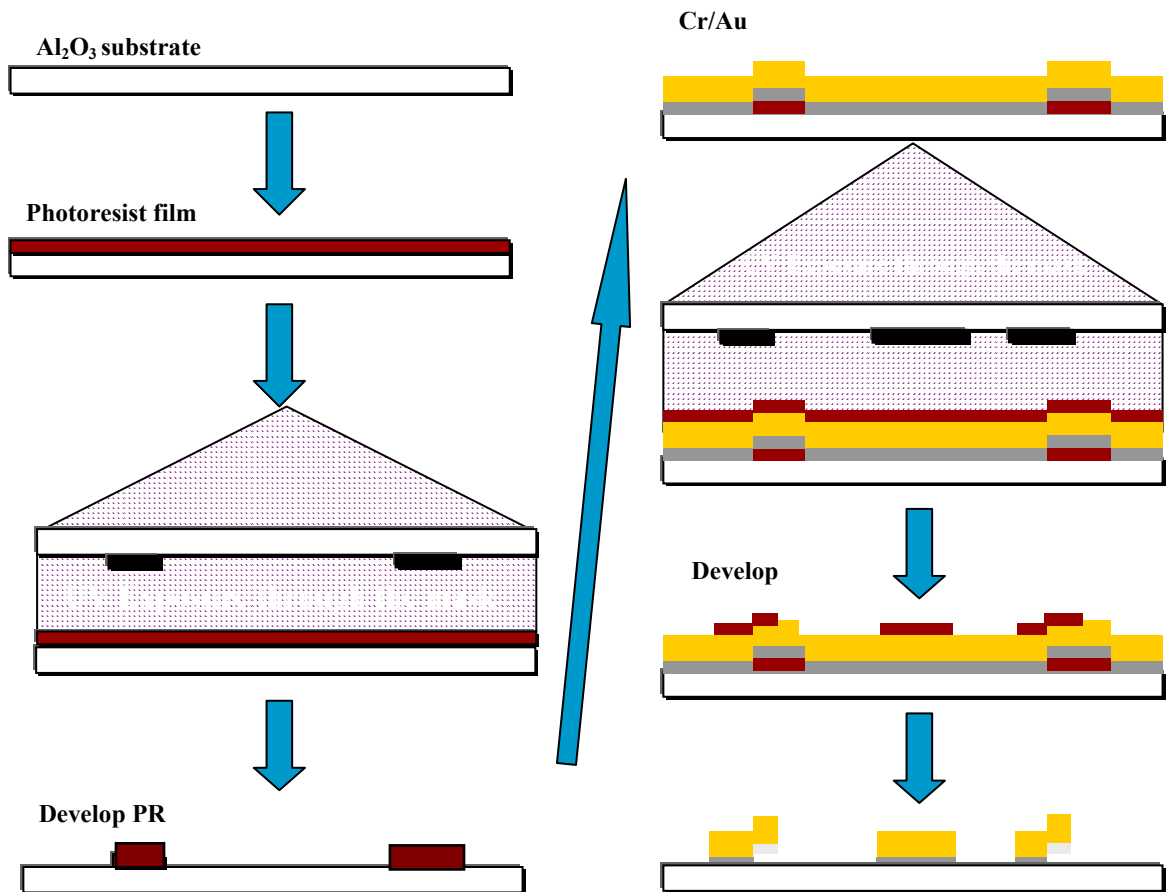


Figure 3-7 Pump with emitter overhang fabrication workflow.

Once fabricated, the electrodes were tested for shorted or broken bus lines. They were also photographed with a digital camera through a microscope in order to have a visual record of the electrode surface. These pictures could later be compared with views of the electrode surface after testing for identification of possible degradation. After visual inspection, the thickness of the electrodes was measured with a mechanical profilometer. These data were also used in monitoring deposition or removal of electrode material. Figure 3-8 presents several photographs of the microfabricated electrodes on two substrates of different roughness (alumina and silicon) made with two different masks (the glass/chrome mask and an inexpensive mask printed on a transparency sheet, which had much lower resolution).

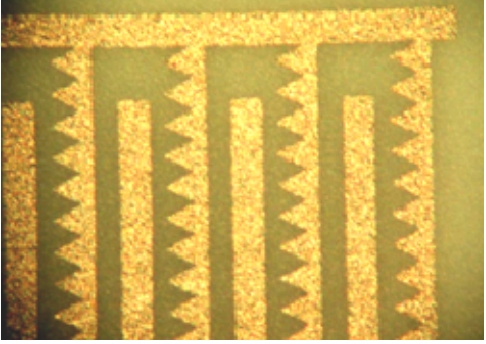
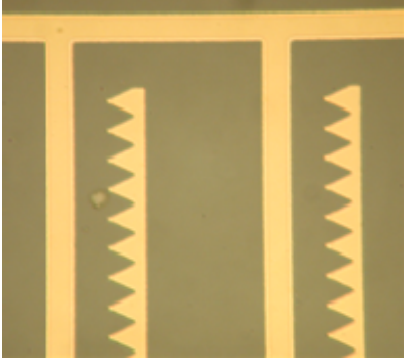

	<p>Electrodes on an alumina substrate made using a chrome mask.</p>
	<p>Electrodes on a silicon substrate made using a chrome mask.</p>
	<p>Overhang electrodes on a silicon substrate made using a transparency mask.</p>

Figure 3-8 Electrode fabrication on different substrates and using two types of masks.

3.4 Micropump test setup

3.4.1 Pump packaging

The package for this study had several requirements. The fluid flow ports had to be small enough to minimize the overall dimensions of the system, but large enough to enable the integration of commercially machined piping and connection components. In addition, the prototyping and testing involved in this study required the pumps to be un-

packaged for post-test investigation. Ability to vary channel height was also desirable, as fluid depth was one of the design variables to be investigated. Lastly, the materials needed to be chemically inert, and preferably outgas as little as possible in order to minimize the level of impurities in the working liquid and the associated unwelcome electrochemical reactions. These requirements were addressed over the entire course of the project and resulted in several versions of pump packaging.

One of the key challenges was the creation of a small pumping section volume with a minimum internal pressure drop. Project predecessors Darabi and Rada, in their first iteration, chose to glue a flat alumina top cover to the bottom electrode substrate using a thin layer of epoxy and to drill two holes into the cover for letting the fluid in and out. Such packaging, though inexpensive and relatively simple, had several disadvantages: it was difficult to control the channel height and the shape of epoxy gasket (Figure 3-10), the epoxy outgassed, and it was impossible to investigate or clean the electrodes without destructively opening the package. Darabi and Rada were aware of some of these problems and started the design of a lithographically machined 3-D polymer top cover with inline ports and a fixed channel depth. Such a top cover was the first package used in the current study. A schematic of the packaging is shown in Figure 3-9. This design suffered from several of the problems in the previous version, and the inline ports did not reduce the pressure drop significantly. In addition, the cover started softening at only 60 °C.

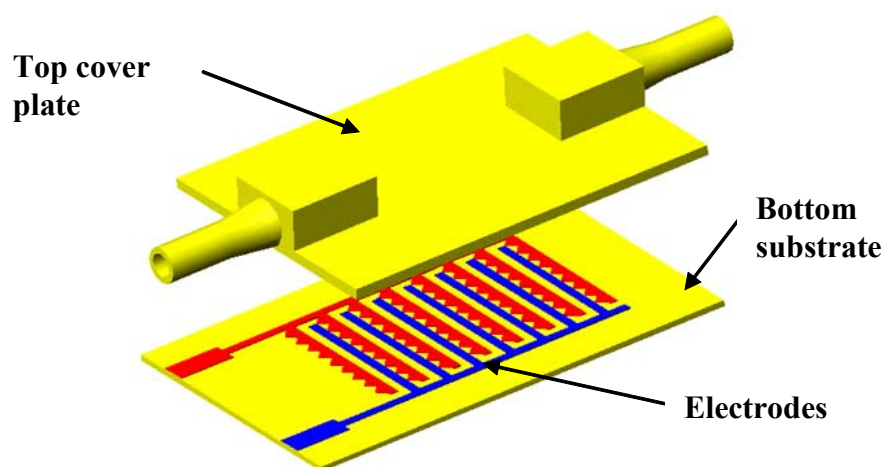


Figure 3-9 Inline pump package with epoxy gasket (not shown).

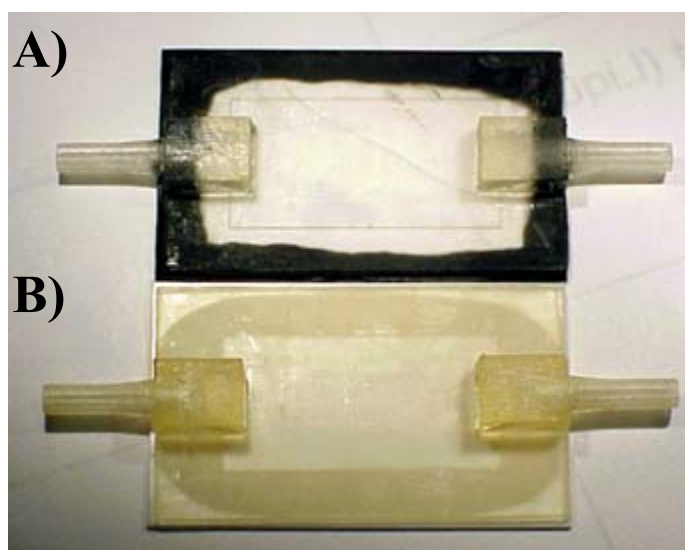


Figure 3-10 Inline top covers attached to the substrates using different epoxies. A) High viscosity epoxy leaves voids in the channel. B) Low viscosity epoxy leaks into the channel.

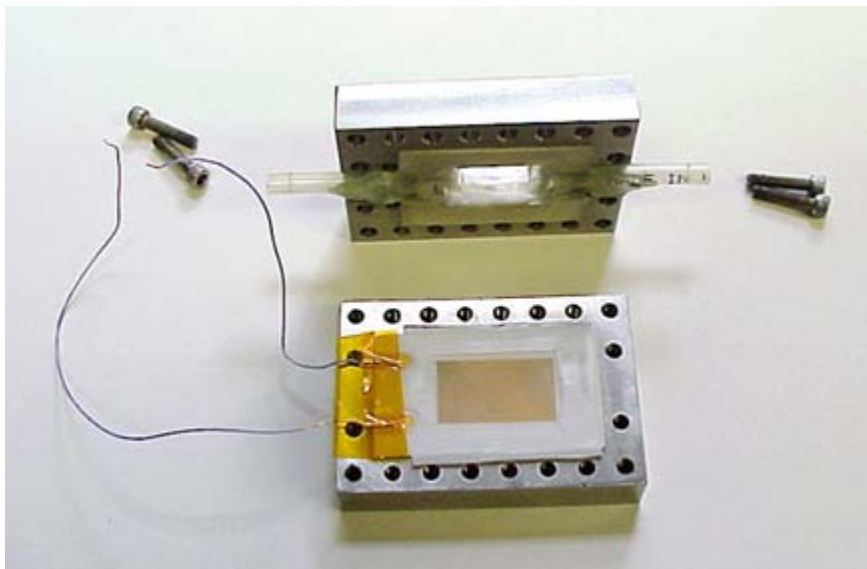


Figure 3-11 Inline pump packaging with variable Teflon gasket.

The next version is shown in Figure 3-11. The improvements consisted of variable channel heights defined by Teflon gaskets of different thicknesses that were clamped between two steel plates. Teflon is more inert than epoxy, thus reducing undesirable chemical interactions with the working liquid. The top cover remained the same stereo-lithographically produced plate with inline ports; however, this time the polymer cover was embedded in a matching stencil carved in a steel cover. Two steel plates were clamped together using evenly tightened screws. This package was able to hold 100 millitorr of pressure (low vacuum) for several days.

The majority of the tests were conducted using this package. However, a few improvements were still necessary. First, the connection of the test loop to the pump degraded the mechanical strength of the ports. Second, the polymer cover was not transparent enough to see the electrodes and fluid inside the pump. Third, this polymer was porous and could potentially outgas.

The final version of the packaging design addressed all these issues and made double sided pump designs possible. First, the polymer cover was substituted with perpendicular steel tube inlet and outlet ports. Since the highest pressure drop occurs in the channel, only a slight increase in pressure drop was observed (less than a 5% increase in pressure drop at flow rates up to 10 ml/min, as shown in Figure 3-13). Results of numerical and analytical modeling of these geometries are shown in Figure 3-12 for both the inline and perpendicular port cases. As the models show, there is only a slight increase in pressure drop for perpendicular versus inline ports for the expected flow rates (0-20 ml/min).

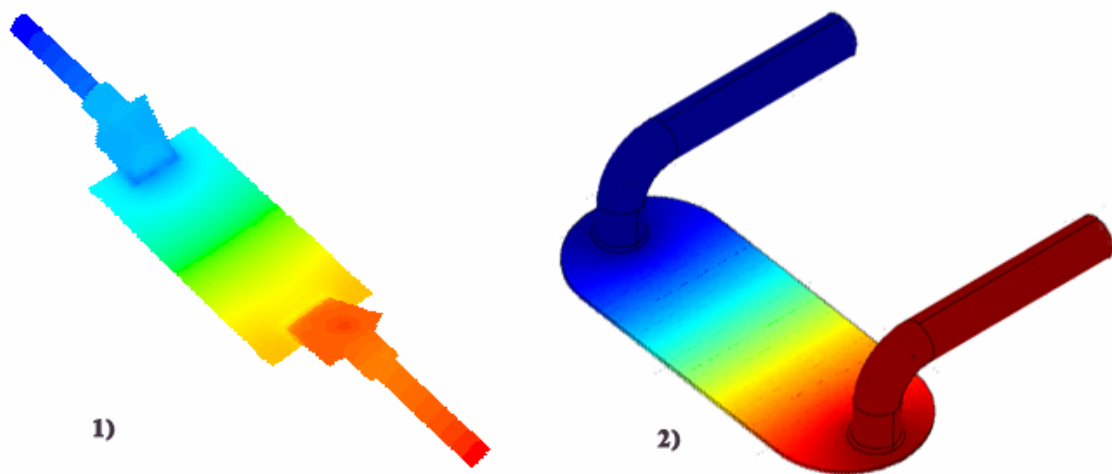


Figure 3-12 Pressure drop contours inside the micropump for 1) inline and 2) perpendicular packaging geometries. *(Figures are not drawn to scale.)*

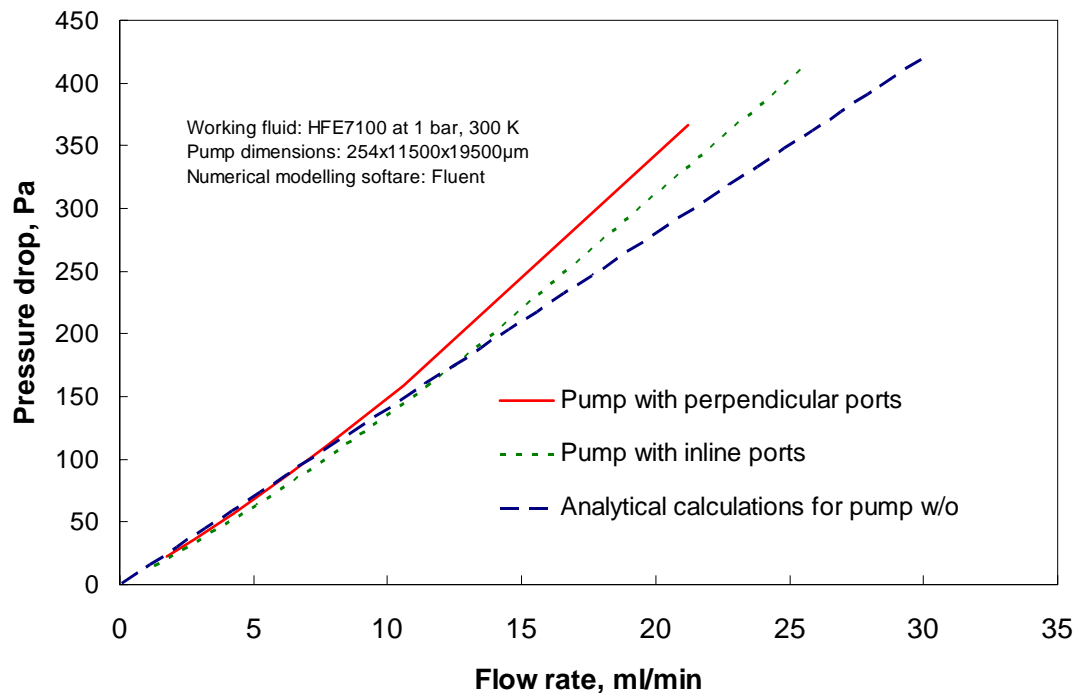


Figure 3-13 Pressure drop vs. flow rate in a micropump channel with 254x11500 μ m cross-section for different packaging designs. Numerical work was carried out using CFD Fluent software code.

Further improvements in the final micropump package included a view-port for monitoring the electrode surface and flow, adjustable torque washers for maintaining a uniform channel height, and a mirrored case block for enabling the pump channel to have two pumping surfaces. The double-sided substrate option was supposed to increase the flow rate by having twice as much pumping force acting on the same volume of liquid, but it was never actually tested in this study. Finally, the use of more durable materials increased the mechanical reliability of the package.

The final package designs are shown in Figure 3-14. The top and bottom cases are made of 7075 aluminum, the view-port is $\frac{1}{4}$ inch thick borosilicon glass, and the inlet and outlet ports are made from $\frac{1}{8}$ inch wall thickness stainless steel tubes. Rubber o-rings ensured a vacuum-tight seal between the substrate and the bottom case, where the

inlet and outlet ports penetrated the substrate. Six pins guided the proper placement of the substrate. Six screws with torque washers (stronger in the middle for balancing the bending moment) ensured tight clamping of the Teflon gasket either between the two substrates or between the substrate and glass blocks.

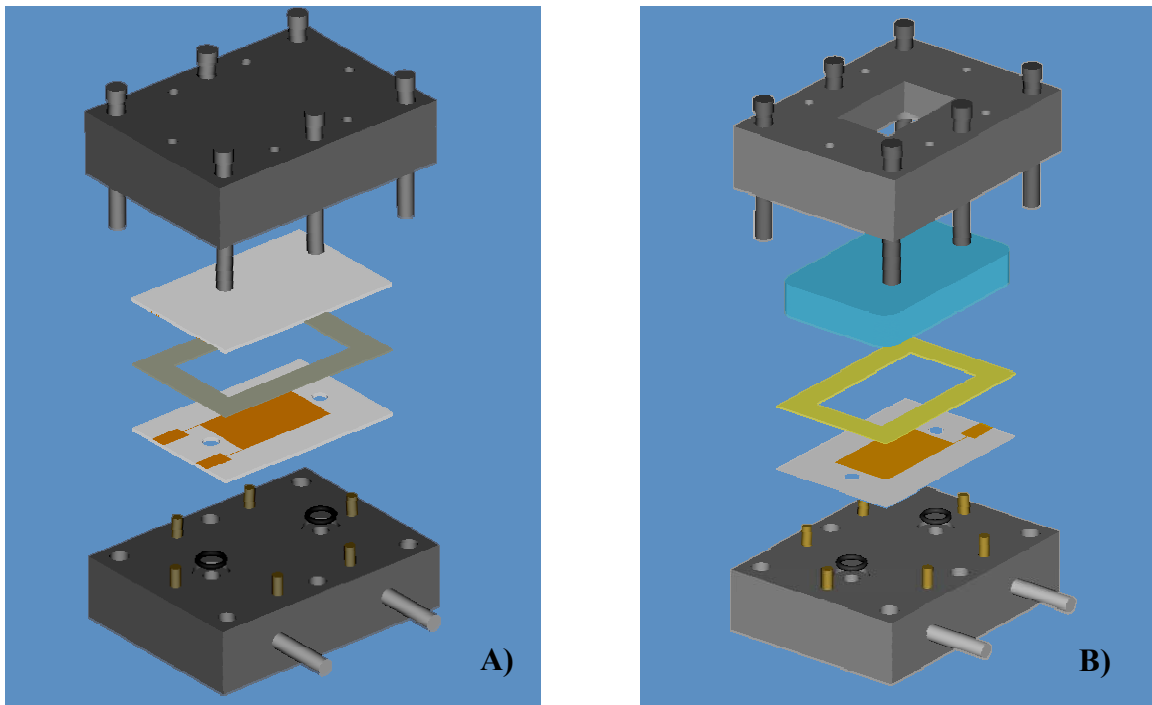


Figure 3-14 (A) Double-sided and (B) viewport pump packaging options.

3.4.2 Test loop

An instrumented test loop was built to measure pressure head, flow rate, and input power. The setup used most commonly by other researchers is an open test loop for evaluating the static pressure head. Tubing is attached to the flow ports, and the loop is open to the atmosphere. Such an arrangement enables the basic manometer principle to be used to evaluate the ability of the pump to generate pressure at zero flow rates by measuring the difference in liquid height between the inlet and outlet. This type of test system was employed at the beginning of the study and is shown in Figure 3-15.

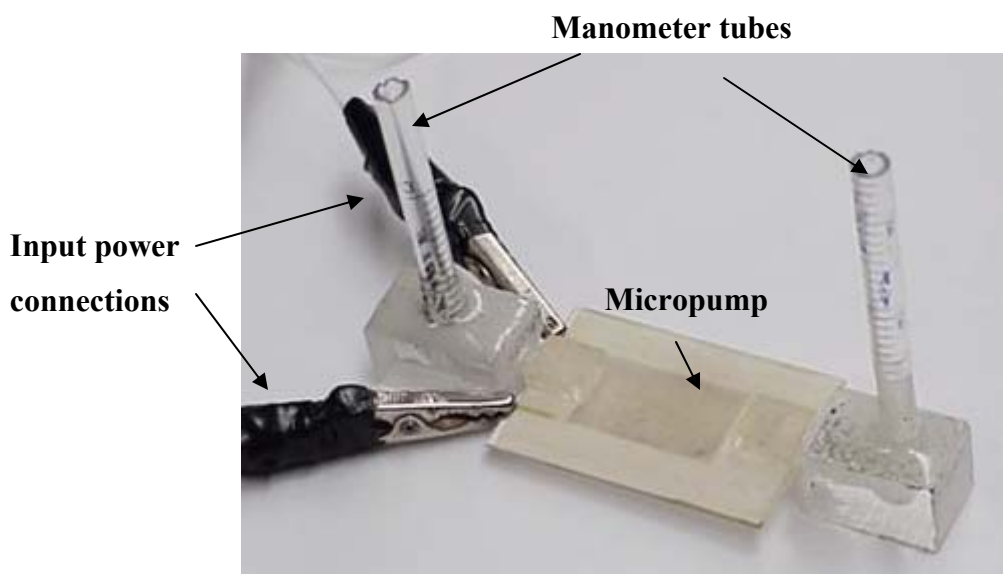


Figure 3-15 First iteration test setup.

Unfortunately, this test setup was able to measure static head only. It was also subject to measurement reading errors, did not provide transient state measurement values, and was open to the atmosphere, thus enabling water and various atmospheric gases to dissolve in our working liquid and participate in undesired electrochemical processes. These findings were based on observations made during and after testing: fluctuations in pressure head, corroded electrodes, and degradation in pump performance over time.

In order to address these deficiencies, a second-generation dynamic test loop was created as shown in Figure 3-16. Major improvements included the following.

- 1) A closed system to enable dynamic operation.
- 2) The addition of a differential pressure transducer (Validyne DP-15) for measuring dynamic pressure and the flow rate.
- 3) The capability of vacuuming and charging of ports for complete system filling with the working fluid.

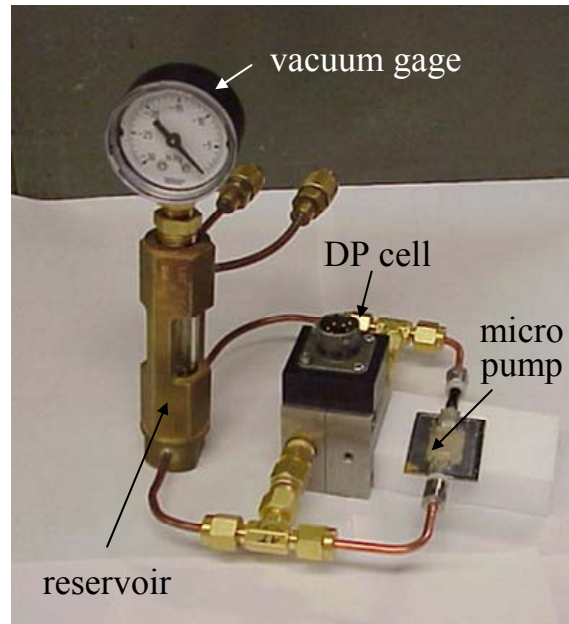


Figure 3-16 Second generation test loop.

This test setup was used to test all the pumps packaged with epoxy-glued top covers. Results, however, were not completely satisfactory. Significant issues included poor repeatability of test data for the same pump designs and instabilities in current and pressure measurements. These problems were partially associated with impurities in the test loop due to outgassing of the components. Further problems involved accurately measuring the low flow rate with the differential pressure transducer as calibration was performed only down to 4 ml/min (available in a commercial low-range mechanical gear pump). These issues were, however, addressed in the last iteration, and were applied together with development of the new pump packaging schemes discussed earlier.

As Figure 3-17 presents, various attempts were made to resolve the pump testing issues. First, the copper piping initially used was replaced with thin-wall stainless steel tubing to minimize outgassing. The loop was flushed with working liquid 3-5 times and pumped with a refrigeration vacuum pump down to 5-20 mTorr pressure. In order to

achieve such a high vacuum, the external vacuum pump was operated for several days before charging the test loop with the working fluid. The second substantial improvement resulted from calibrating the flow with a low-flow rate calibrated pressure transducer, which was also used to determine the differential pressure head for various loop resistances. The loop resistance could be controlled by a static pressure valve added to the system. Finally, the procedure for charging the loop and putting it under vacuum was improved by first boiling the working fluid in the reservoir to release the trapped gasses in it.

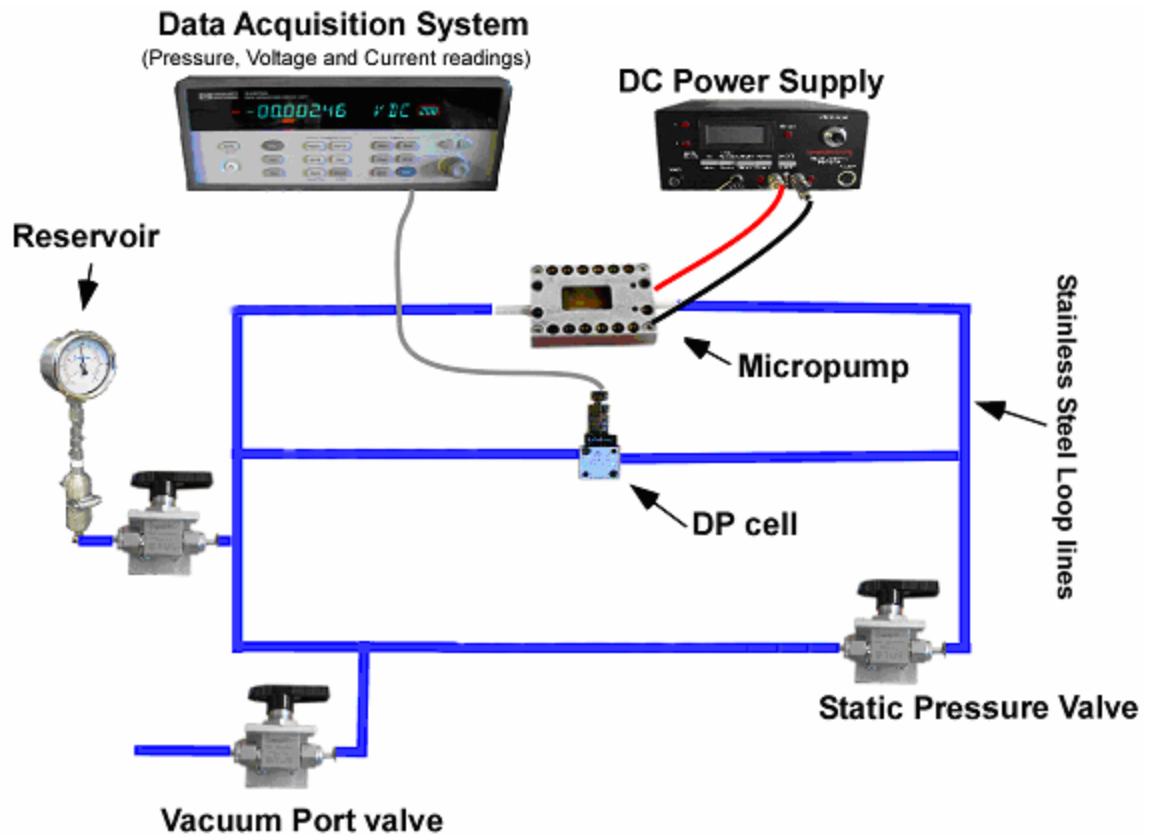


Figure 3-17 Final test setup.

3.4.3 Measurement and instrumentation

The performance of the micropump was evaluated by monitoring one input variable, voltage, and three output variables, pressure, flow rate, and electrical current. Instrumentation was either chosen from available commercial devices or custom built to suit the expected range of performance variables. Calibration of all measurement devices was performed, and the uncertainty of measurements recorded.

Differential Pressure Transducer

In order to measure the pressure difference across the inlet and outlet ports of the micropump, a differential pressure transducer was used. Since ion-drag micropumps generate relatively low pressure heads (several hundred Pascal), the pressure transducer

for the pump under investigation needed to have a range of about 2 kPa and a sensitivity of a few Pascal. In addition, a device with a quick response time was needed to monitor the transient performance of the pump.

The pressure transducer Validyne DP-15 (Northridge, CA) met all of the above demands. It is a variable reluctance-type transducer consisting of a magnetically-permeable stainless steel diaphragm, clamped between two blocks of stainless steel, between two cavities. An inductance coil is embedded in each block. The operation of the transducer is based on a magnetic reluctance variation with a deflection of the diaphragm toward the cavity with lower pressure, decreasing the width of one cavity and increasing the other. A summary of the specifications for this pressure transducer is presented in Table 3-6.

Table 3-6 Pressure transducer and output signal demodulator specifications.

Instrument and Facility	Model and Manufacturer	Specifications
Differential pressure transducer and carrier demodulator.	Variable reluctance DP15 with diaphragm -20 and carrier demodulator with 2 ports – CD 280, Validyne Engineering Corp.	<ul style="list-style-type: none"> • Pressure Range: 0- 880 Pa • Accuracy: $\pm 0.25\%$ FS • Linearity: $\pm 0.05\%$ FS • Digital output 0-10 V for FS

The pressure transducer was also used to measure flow rate by calibrating it to a specific pressure drop. The first step was to calibrate the pressure transducer. This was accomplished using a manometer and another, factory-calibrated transducer. Results, shown in Figure 3-18, indicate high linearity and repeatability. The zero offset was corrected for each experimental run, since it varied over time due to changes in ambient temperature, humidity, and previous operation conditions.

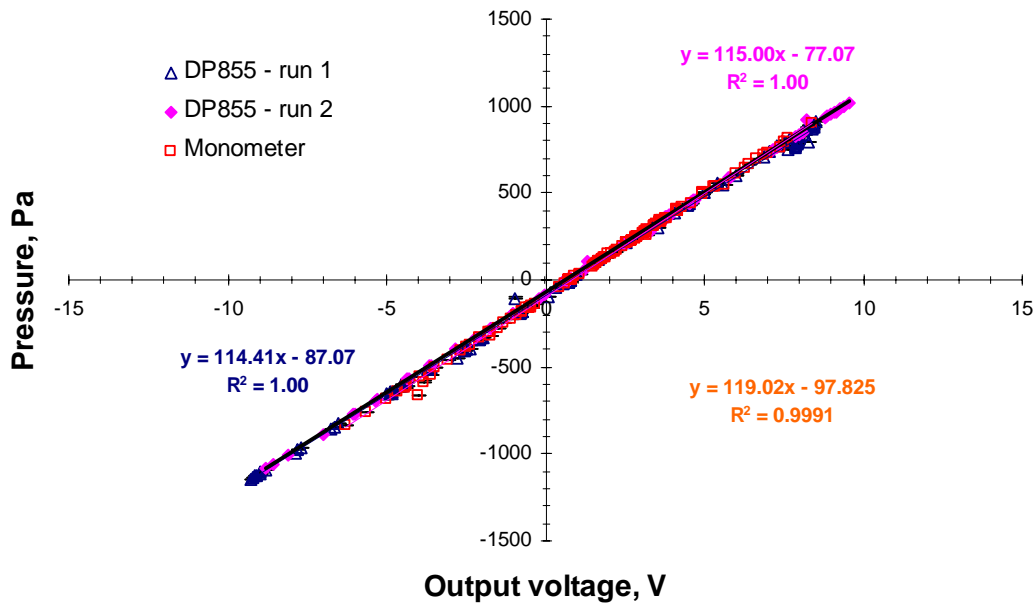


Figure 3-18 Pressure transducer DP15-20 calibration with manometer and factory-calibrated pressure transducer.

HFE7100 evaporates quickly at room temperature in an open container, and so pumping it with the external low-range pump was not possible below rates of about 3 ml/min (the minimum range of our commercial gear pump) was not possible. The challenge of establishing a known flow rate lower than 3 ml/min with HFE7100 was overcome by introducing a different fluid and relating its flow rate to that of HFE7100 through their viscosities, as shown by Equation (3-2). For the same channel geometry and a fixed pressure drop, the flow rates of two fluids are related to each other as the inverse ratio of their viscosities:

$$\dot{V}_{HFE7100} = \frac{\mu_{N2}}{\mu_{HFE7100}} \cdot \dot{V}_{N2}$$

(3-2)

Incompressibility of the measured fluids was assumed, which was justified since the temperature and velocity of the fluid were low. Assuming laminar flow, pressure drop in the channel can be approximately by:

$$dP = 32 \frac{L}{D^2 \cdot A_C} \cdot \frac{\mu}{\rho} \cdot \dot{m}$$

(3-3)

Nitrogen (N₂) gas was chosen for calibrating the flow rate to the DP-15 pressure transducer using the flow meter specified in Table 3-7. The ratio of N₂ to HFE7100 viscosities is 30.5.

Table 3-7 Specifications for gas flow meter.

Instrument and Facility	Model and Manufacturer	Specifications
Gas flow meter	GF-2060, Gilmont Instruments (Barnant, Inc)	<ul style="list-style-type: none"> • Flow range: 0- 80 ml/min • Accuracy: ± 25% or ± 1 scale division (whichever is greater)

Calibration results for five different loop resistances were performed and are presented in Figure 3-19. Results displayed high repeatability for up to 3 runs: measurement uncertainty was determined to be 0.8 Pa for pressure head and 0.1 ml/min for flow rate.

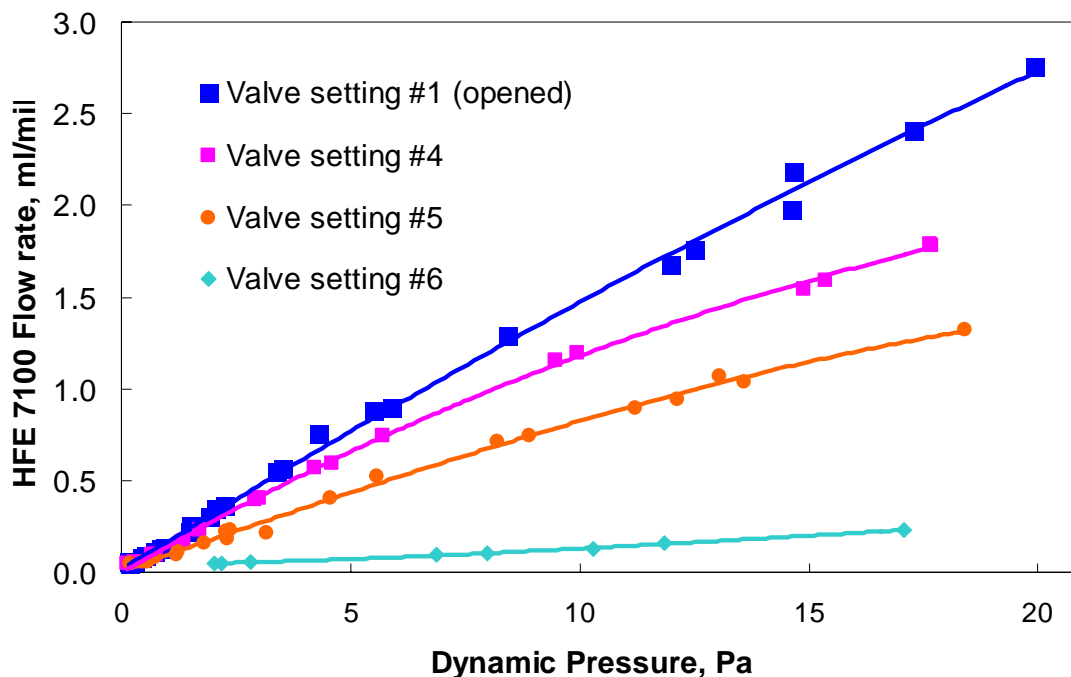


Figure 3-19 Calibration of the pressure transducer with the flow rate in the loop using various loop resistances.

Data Acquisition Unit

A data acquisition unit was used to measure and record the thermocouple signals, the electric current applied to the micropump, and the output signal of the pressure transducer demodulator. The specifications of the data acquisition unit are presented in Table 3-8.

Table 3-8 Data acquisition unit specifications

Instrument and Facility	Model and Manufacturer	Specifications
Data acquisition unit	34970A, Agilent Technologies, Inc.	<ul style="list-style-type: none"> • Best range of accuracy for thermocouple type T: 1.0 °C • DC voltage measurement accuracy for a range of 10 V: \pm (0.0035% of reading + 0.0005% of range) • Resolution: 1 ppm

DC Power Supplies

Based on preliminary tests and reports in the literature, the power supplied to the EHD micropump was expected to be on the order of milliwatts. For an electrode spacing of 50 μm , voltages up to 600-700 V were reached before electric breakdown occurred in HFE7100, so a Brandenburg 477 (Dudley, UK) power supply with low current and precise voltage regulation ratings was chosen. The specifications of the DC power supply are presented in Table 3-9.

Table 3-9 DC power supply specifications.

Instrument and Facility	Model and Manufacturer	Specifications
DC power supply for micropump operation	Brandenburg 477	<ul style="list-style-type: none"> • Rated output voltage: 0-1000 V • Output current: 0-4 mA • DC voltage ripple peak to peak: 4 mV

3.5 Summary

This chapter presented the work done on the design, fabrication, and packaging of the ion-drag micropump. In addition, an accompanying test setup for evaluation of the micropump's performance parameters was designed, built, and calibrated. The test loop enabled isolation of the pump from water vapor and oxygen present in the environment. Until this work, no reported studies on the EHD pumping phenomenon isolated the corrosive variables in test conditions to the extent presented here. In addition, packaging with varying channel heights and a surface monitoring viewport were engineered to allow more in-depth investigation of the pump prototypes. Finally, innovative electrodes building on Darabi's previous work were designed and fabricated, providing a good

number of designs to be tested and analyzed, with the ultimate objective of identifying the role of pump design parameters.

CHAPTER 4 EXPERIMENTAL RESULTS

4.1 Introduction

One of the main contributions of this work was the systematic experimental identification, characterization, and analysis of several micropump geometric design parameters on the performance of the ion-drag micropump. This chapter summarizes and analyses this experimental work.

4.2 Classification and nomenclature of the micropump prototype designs

The design parameters that were tested are listed in Table 4-1 and visually displayed in Figure 4-1. Micropump prototypes were assigned a code name according to the following template, with units of μm : d_{el} -shape- $d_{\text{pel}}/t_{\text{el}}$. For example, a micropump with a 50 μm electrode spacing and a 200 μm distance between neighboring electrode pairs having a flat emitter was designated 50f200. Electrode thickness t_{el} was usually omitted, as only a few prototypes were manufactured with different t_{el} .

Table 4-1 Micropump design variables

Geometric parameters	Designation/Description
Channel height	h_{ch}
Electrode spacing	d_{el}
Electrode pair spacing	d_{pel}
Electrode thickness	t_{el}
Electrode shape: <ul style="list-style-type: none"> - flat - saw-tooth - overhang - bumps 	<ul style="list-style-type: none"> f s ov b
Packaging: <ul style="list-style-type: none"> - inline - perpendicular - 	Inlet and outlet ports parallel to the flow perpendicular to the flow

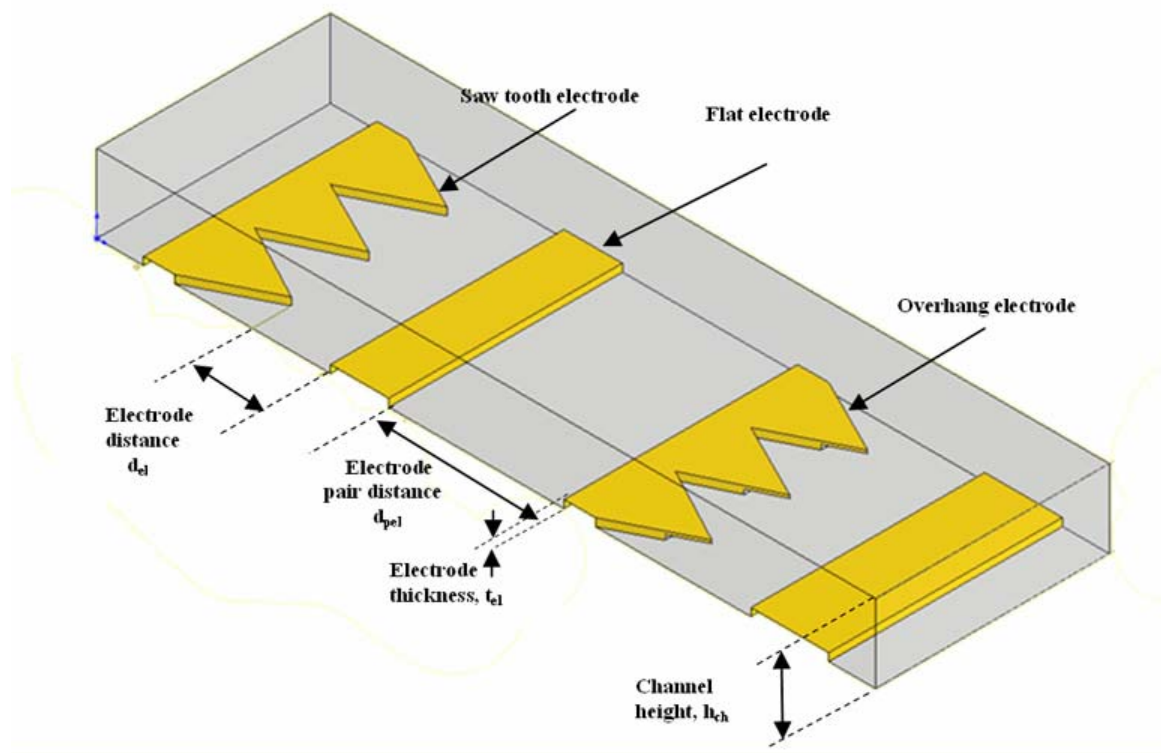


Figure 4-1 Micropump test variables.

Other code letters were included to describe the packaging. (For a description of the various packaging designs, refer to Chapter 3.) The key parameter was flow channel height h_{ch} , which is given at the end of the micropump designation. For example, the above mentioned micropump with a 220 μm channel was named 50f200-220.

4.3 Discussion and classification of the micropump design parameters

Pumps are typically optimized to either generate a high flow rate or to build a large backflow pressure. These two quantities are always inversely related, as shown by the pump characteristic curve in Figure 4-2. The operating pump point is determined from the intersection of the pump characteristic curve with the external system curve. It shows the relationship between flow rate and pressure *loss*, and it depends on both the fluid and the physical layout of the path. Losses are introduced by friction, protrusions, and changes in channel diameter. The curve is parabolic because friction losses vary as \sqrt{q} .

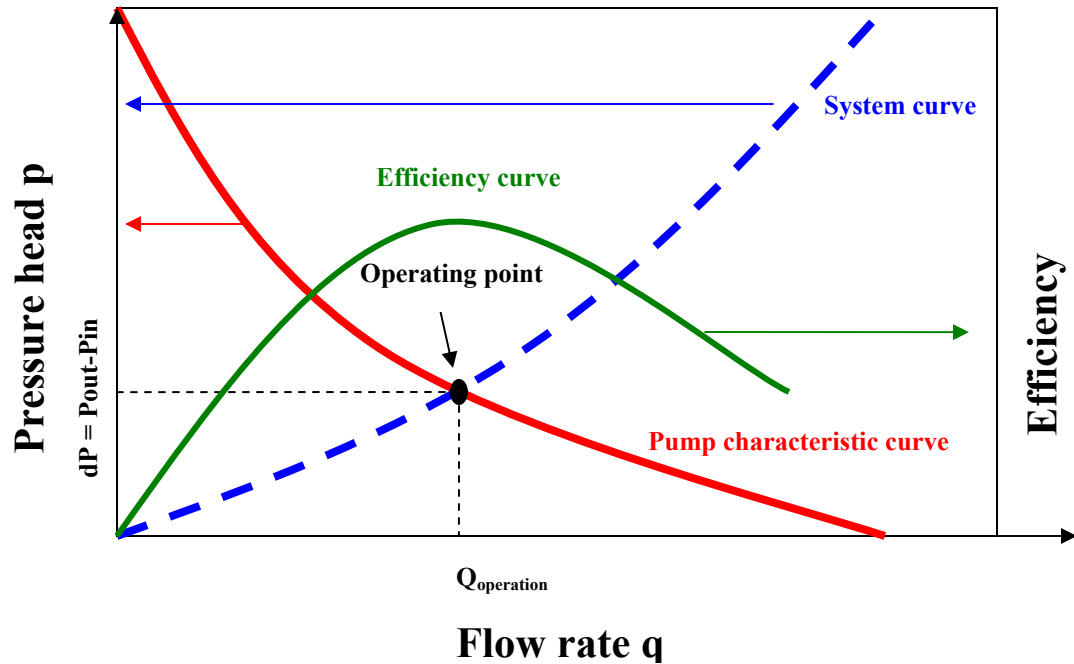


Figure 4-2 Typical pump operating curves.

In this study, the performance parameters are of two types (Table 4-2): mechanical/electrical and reliability. (Detailed descriptions and definitions were offered in Chapter 2.) To show the effects of geometric design variables on performance parameters, the data were presented in different ways (Table 4-3).

Table 4-2 Micropump performance parameters.

	Parameter	Designation/Description/Units*
Mechanical/Electric	Flow rate	q (ml/min) or q_m (g/min), can be volumetric or mass averaged
	Differential pressure head	dp (Pa)
	Backflow pressure head	P_s (Pa)
	Electric current	I (μ A)
	Voltage	V (V)
	Electric power	P (mW)
	Mechanical power	P_m (mW)
	Mechanical efficiency	H (%)
Reliability	Electrode degradation	Visual evaluation of the electrode shape and color. For some pumps scientific instrumentation was used to determine chemical composition and electrode thickness.
	Operational lifetime	An approximate evaluation of the steady performance of the micropump.
* These units are used in the charts and in comparative studies. SI units are used for the calculations.		

Table 4-3 Description and explanation of frequently used types of plots.

Full description	Code	Significance
Current vs. voltage	I-V	1) Used in numerical modeling to obtain emitter charge density. 2) Used to find voltage onset point. 3) Used to estimate current operational regime (ohmic, saturation, injection).
Pressure vs. voltage	P-V or P_d - V	1) Shows dependence of backflow pressure on the input voltage to electrodes. 2) If used for dynamic case, P_d represents differential pressure drop.

Power vs. voltage	P_w -V	Shows the power consumption $P_w = I \cdot V$ for different input voltages.
Flow rate vs. voltage	q-V	Shows the dependence of flow rate to the input voltage. Typically closely resembles the shape of I-V or P_d -V if test loop pressure drop curve has close to linear dependence.
Efficiency vs. voltage	Eff-V	Relation between the efficiency and voltage allows comparison of various designs at given input voltages.
Efficiency vs. flow rate	Eff-q	Shows pump mechanical efficiency dependence on flow rate. This graph is useful if most efficient flow rate is desired.
Flow rate vs. power	q- P_w	Allows comparing pump designs based on power input, not only voltage levels.
Channel height vs. maximum efficiency	h_{ch} - eff_{max}	Useful way to find the most efficient channel height.
Flow rate vs. channel height	q- h_{ch}	Indication of the most optimum channel height for maximizing flow rate.
Static pressure head vs. channel height	P- h_{ch}	Backflow pressure characterization in terms of channel height.
Static pressure head vs. electrode spacing/electrode pairs	P- d_{el}/d_{pel}	Pressure effect of varying electrode distances.
Flow rate vs. electrode spacing/electrode pairs	q- d_{el}/d_{pel}	Flow rate effect of varying electrode distances.

In order to compare the ion-drag micropump with other pumps, universal performance metrics are needed. For this reason, characteristic pump curves were generated, which provided the flow rate and pressure head between the pump's inlet and outlet for a particular input power, as shown in Figure 4-2. When superimposed on the external system curves, the operating point was located. The efficiency curve was superimposed to determine whether the pump was operating at its maximum effectiveness. Finally, the characteristic curves allowed comparison among pump designs for a given external loop, which was the purpose of this study.

As was discussed in earlier chapters, the EHD ion drag phenomenon relies on high electric fields to strip charges from the electrode. Such aggressive charge injection unavoidably affects the chemical bonding in any material, including electrodes. The present study attempts to describe these destructive phenomena and their effects on the performance of the ion-drag micropump quantitatively with the reliability factors.

4.4 Summary of the micropump prototypes

This research investigated numerous ion drag micropumps. As our understanding of the pumps' performance-influencing variables matured and the experimental settings were improved, the prototypes needed to be retested under the new operating conditions to provide a common baseline for comparison. However, because of project time and budget constraints, it was impossible to do this at full scale. With this limitation, only a few key design variables were identified, and micropump prototypes were built to enable evaluation of those variables while holding the remaining variables constant (as illustrated in Table 4-1). The data are labeled according to the testing conditions and the

assumptions made in reducing the data. Table 4-4 is a matrix of micropump prototypes sorted by the design variable that were tested.

Table 4-4 Test matrix.

Design	h_{ch}	d_{el}	d_{pel}	shape	t_{el}
50f100	100-500	50f	100, 2x	F	0.15-0.3
50s100	100-500	50s	100, 2x	S	0.3
50s200	100-1100	50s	200, 4x	S	0.3
20s80	100-500	20s	80, 4x	S	0.3
20s40	100-220	20s	40, 2x	S	0.3
10s20	220	10s	20, 2x	S	0.3
10s40	100-220	10s	40, 4x	S	0.3
20s40-26deg	100-220	20s	40, 2x	S-26deg	0.3
50sov100	100-220	50sov	100, 2x	sov	0.3

4.5 Testing procedure consistency

Experiments with EHD pumps require high accuracy and sensitive instrumentation, consistent and careful data logging, and of course, a well designed and built pump. Furthermore, to add another challenge, the EHD phenomenon causes irreversible electrochemical processes that affect the molecular structure of the dielectric liquid. In order to ensure the trustworthiness of the experimental data, repeatability of results is necessary. Previous researchers, especially those working with microscale EHD mechanisms, observed some degradation in their pumping cell performance; however, their published data do not reflect any major challenges associated with this damage. No systematic and quantitative study has been reported on this issue to date. Although it may seem strange, this is not surprising given the complexity of this highly irregular and variable-dependent electrochemical phenomenon.

The scientific way to address the problem of repeatability requires identifying, monitoring, and controlling the variables in the problem. If this is done properly, one is aided in identifying and understanding the underlying physics. EHD potential fields exceed, by a few orders of magnitude, those in other processes such as electroplating, electro-osmotic separation and mixing, electrochemical polishing, coloring, and machining. Superb cleaning, degassing, and filtering of the system is required to reduce the effects of undesirable electrochemical processes competing with the sought-after EHD pumping phenomenon.

To minimize uncertainty, the pumps in this project were tested with freshly purified liquid for every run, unless otherwise noted, and the total number of runs for each of the pumps was recorded and monitored. To better understand the importance of doing this, Figure 4-3 and Figure 4-4 show how test repeatability suffered with continued use of the liquid (compare curves A1, A2, and A3, which are for the first, second, and third runs with the same liquid). It can be seen that a subsequent run with fresh liquid, B1, yielded somewhat similar I-V and P-Q curves to the first run, A1. This indicates that the decrease in current for runs A1-A3 was mainly due to changes in the working liquid, rather than in electrode surface chemistry.

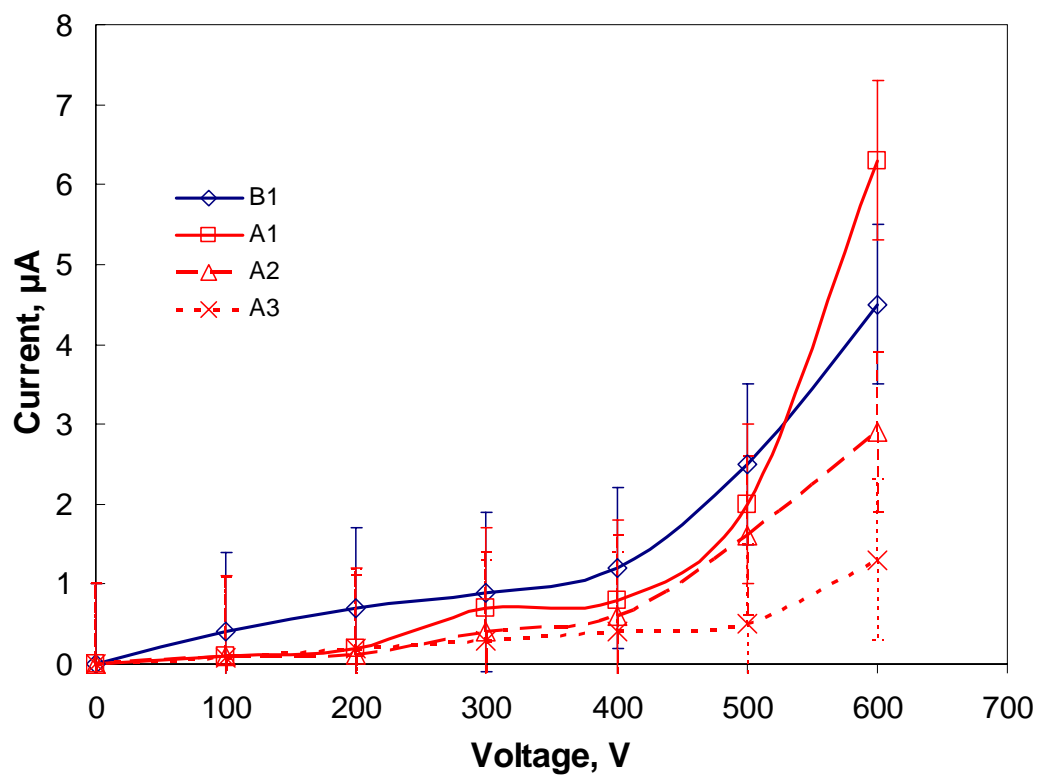


Figure 4-3 Current-voltage (I-V) curves for three sequential runs with the same working liquid (A1-A3) followed by a run with fresh liquid (B1) in pump 50s200-h380.

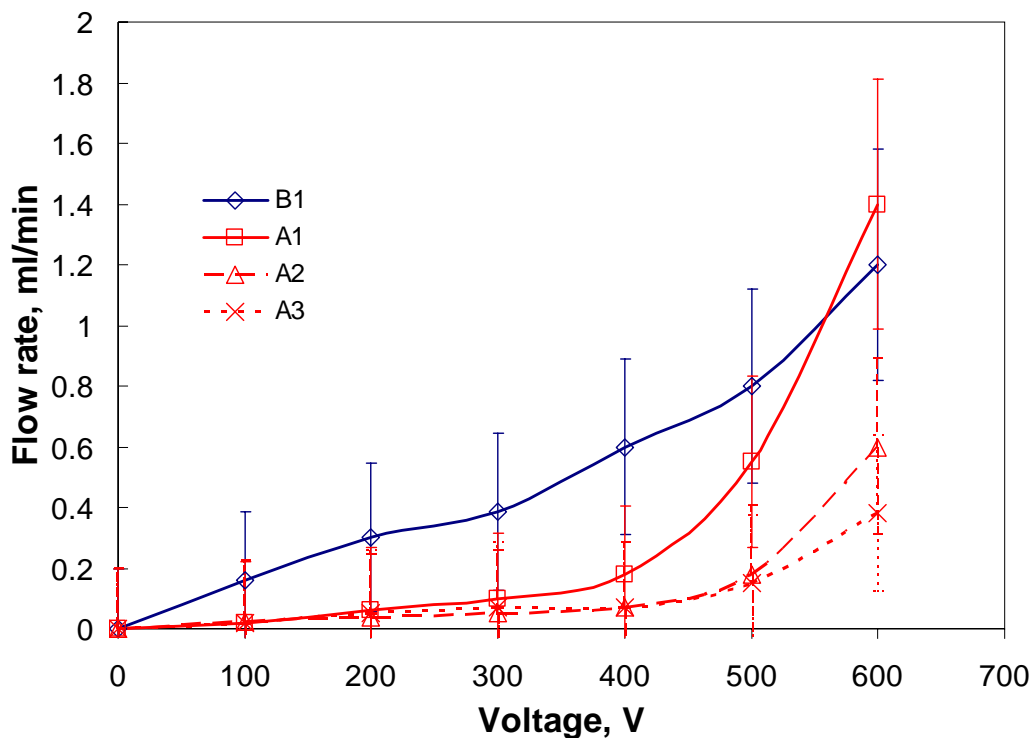


Figure 4-4 Flow rate-voltage (Q-V) curves for three sequential runs with the same working liquid (A1-A3) followed by a run with fresh liquid (B1) in pump 50s200-h380.

These results, however, do not imply that the electrodes are not affected and do not play a role in the pump's reliability. On the contrary, prolonged experiments and higher voltages violently change the electrode surface. The electrodes in this study were monitored visually, and at the end of testing, height measurements were taken and compared to the initial metal thickness. A more in-depth discussion on electrode degradation is presented in section 4.8.1.

4.6 Data reduction workflow

The experimental work involved processing half a dozen input variables and almost twice as many output parameters. Manipulating and controlling such a large amount of data required a carefully planned and coordinated processing path.

Furthermore, results had to be presented clearly, as otherwise it would be easy to get lost among the plethora of data.

The data reduction workflow consisted of multiple tests on isolated variables while maintaining constant the other pump geometric variables within fabrication tolerances. Data collection included recording the history of a particular pump's performance. The raw data (as shown in Table 4-5) were then further processed by taking the average values and calculating standard deviations, which were included in the overall uncertainty of the data together with the instrumental accuracy.

Table 4-5 Typical raw data from a micropump.

208(Time stamp)	208(Seconds)	208(VDC)	Pressure (Pa)	222(Time stamp)	222(Seconds)	222(ADC)
02:33.6	0.019	-4.90E-02	0.0	02:33.9	0.359	-1.55E-07
02:43.7	10.076	-4.90E-02	0.0	02:44.0	10.416	-1.29E-07
02:53.7	20.133	-4.89E-02	0.0	02:54.1	20.473	-1.03E-07
03:03.8	30.189	-4.89E-02	0.0	03:04.1	30.529	-7.80E-08
03:13.8	40.25	-4.84E-02	-0.1	03:14.2	40.59	-7.80E-08
03:23.6	50.003	-1.98E-01	10.2	03:23.9	50.343	2.42E-05
03:33.6	60.057	-2.59E-01	14.4	03:34.0	60.397	2.41E-05
03:43.7	70.112	-2.69E-01	15.1	03:44.0	70.452	2.31E-05
03:53.8	80.171	-2.73E-01	15.4	03:54.1	80.511	2.23E-05
04:03.8	90.228	-2.75E-01	15.5	04:04.2	90.568	2.19E-05
04:13.6	100.003	-2.75E-01	15.5	04:13.9	100.344	2.17E-05
04:23.6	110.062	-3.66E-01	21.8	04:24.0	110.402	4.60E-05
04:33.7	120.125	-3.13E-01	18.1	04:34.1	120.465	4.51E-05
04:43.8	130.182	-3.10E-01	17.9	04:44.1	130.522	4.44E-05
04:53.8	140.242	-3.08E-01	17.8	04:54.2	140.583	4.42E-05
05:03.6	150.003	-3.08E-01	17.8	05:03.9	150.344	4.40E-05
05:13.6	160.061	-3.07E-01	17.7	05:14.0	160.401	4.38E-05
05:23.7	170.118	-3.70E-01	22.0	05:24.0	170.459	9.99E-05
05:33.8	180.177	-7.32E-01	47.0	05:34.1	180.517	1.33E-04
05:43.8	190.238	-5.66E-01	35.6	05:44.2	190.578	1.31E-04
05:53.6	200.003	-4.89E-01	30.2	05:53.9	200.344	1.31E-04
06:03.6	210.057	-4.76E-01	29.4	06:04.0	210.397	1.34E-04

4.7 Test results of the geometrical design parameters

4.7.1 Overview

The overabundance of test data and the large amount of reduced data are reported, as mentioned previously, according to the following design variables: electrode

thickness, flow channel height, electrode spacing, electrode pair spacing, and electrode shape. Other factors were kept uniform, including ambient temperature (about 21°-25°C), working liquid (3M[®] HFE7100[™]), packaging materials, and liquid charging procedure.

4.7.2 Electrode thickness

All micropump prototypes were manufactured using microfabrication techniques as described in Chapter 2. This significantly limited the electrode design variations in terms of shape and materials. After a literature review and some preliminary tests, gold (Au) was chosen as the electrode material. Thermal evaporation was used to deposit films of various thicknesses. Due to internal stresses, which are intrinsic, the film thickness was limited to about 0.5 μm . Further deposition of the metal yielded poorly-adhesive and/or crack-prone films.

As discussed previously, emitting electrode geometry plays an important role in creating space charge at the metal/liquid interface, with the injected charge a function of electric field near the electrode surface (Mirotvorsky and Stishkov 1996). It was speculated that greater electrode thickness could result in a larger electric field. To test this hypothesis, three different electrode thicknesses were deposited on the same ceramic substrate: 0.1, 0.3, and 0.5 μm . Figure 4-5 shows that electrode thicknesses did not affect the performance of the micropump.

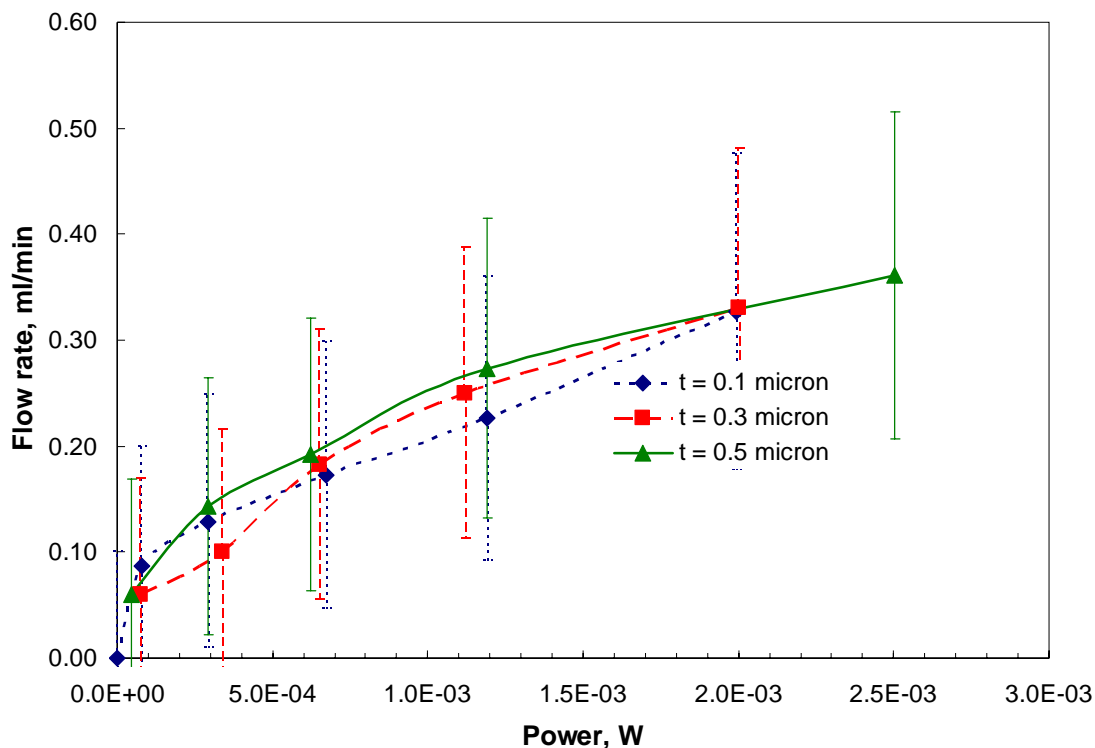


Figure 4-5 Flow rate vs. power for pump 50f100-h220 with three electrode thicknesses.

4.7.3 Surface roughness

The electric field created at the surface of the emitting and collecting electrodes is affected not only by the overall geometrical shape of the electrode, but also by surface microscopic irregularities. Surface roughness can change not only the electric field, by introducing points with high curvature, but also the amount of emitted charge through a larger metal/liquid interface area.

Though there is great potential for exploration and application of the surface roughness variable to ion-drag pumping, the difficulty of controlling, measuring, and monitoring roughness prevented us from studying it in depth. Therefore, instead of varying this design factor, surface roughness was isolated by choosing only three substrates throughout the experiments. (A brief attempt was made to use electroplating to

increase the roughness, but the lack of apparent improvement in the pump's operation, the difficulty of establishing proper sizing methodology, and a shortage of resources stopped this work from further development.)

Thermal evaporation of metals replicates the surface relief of the substrate. Three surfaces with different roughness were used in this work: alumina (Al_2O_3) blocks, polished to 0.2 and 0.02 μm levels, and silicon wafers with thermally deposited silicon dioxide, which had a roughness of about 5 \AA . Highly polished alumina was chosen as the main working substrate since it provided the best combination of durability and smoothness.

Initial experiments were performed with all three substrates. Figure 4-6 shows that changing substrate had no measurable effect on the performance of the pump.

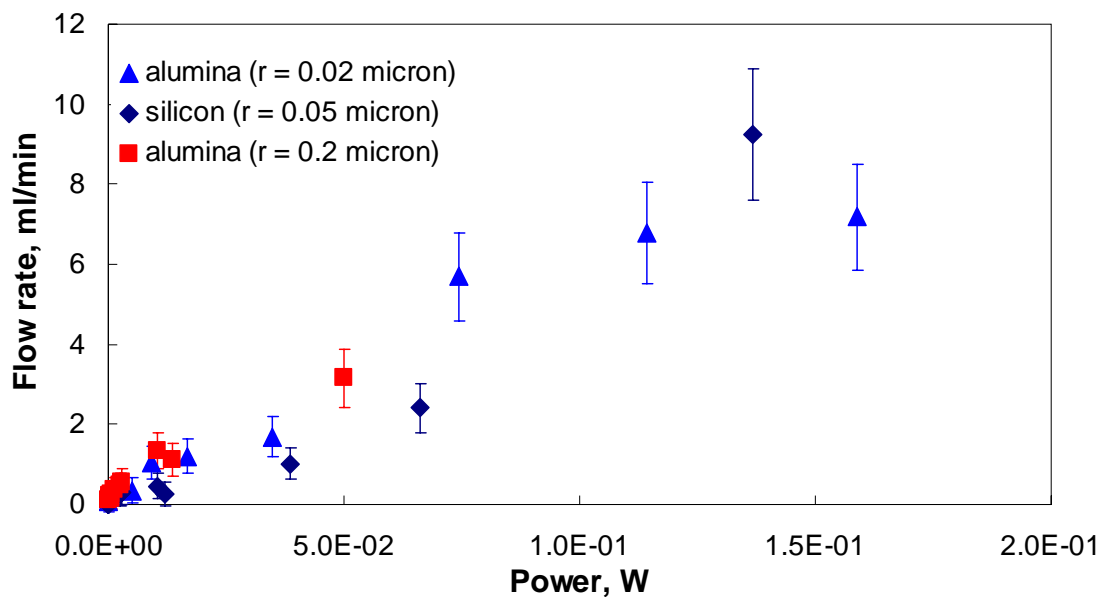


Figure 4-6 Effect of surface roughness (20s80-h220) on flow rate.

4.7.4 Flow channel height

The pump must overcome not only external, but also internal flow resistance. For these ion-drag micropumps, internal wall friction was comparable, if not greater than, the external loop resistance. Assuming laminar flow and neglecting inlet and outlet flow transitions, a simplified analytical model of the micropump results in an exponential increase in pressure drop with diminishing channel height (Olson 1980). This result is illustrated with expected flow rates and realistic micropump design parameters in Figure 4-7. More details on this model are available in Appendix B, where EES code with an explanation of each equation is given.

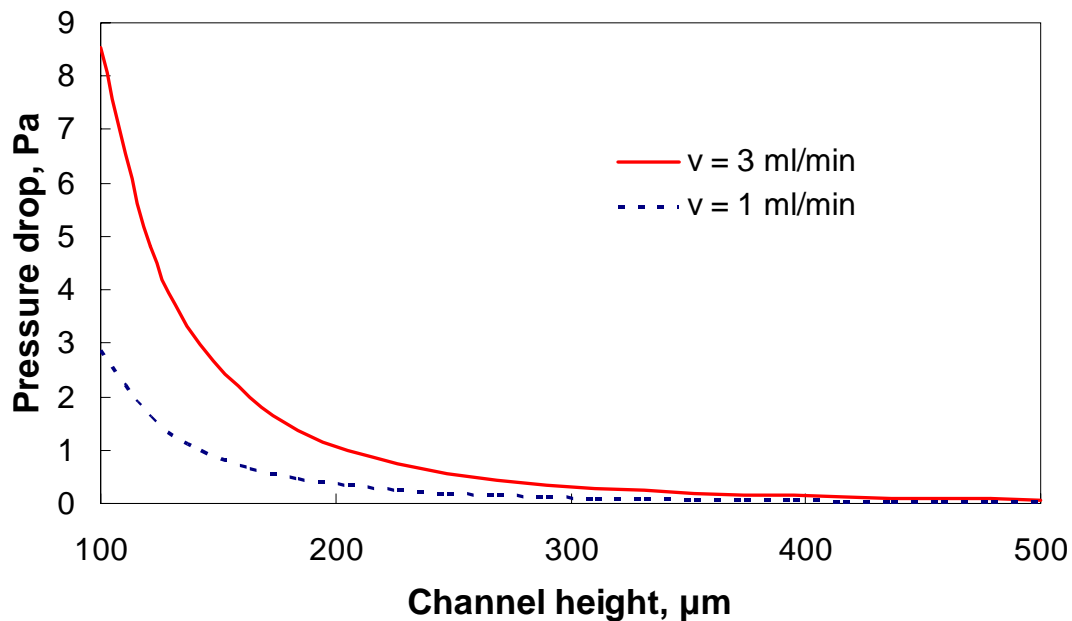


Figure 4-7 Effect of channel height on pressure drop in the micropump (analytical model).

Consideration of channel height is important in trying to achieve maximum flow rate. As discussed above, an optimum channel height is expected to exist for a particular pump design. Figure 4-8 shows comparative pressure drops in the external test section

and in a channel of average height ($250\ \mu\text{m}$), indicating that the highest flow resistance occurs in the micropump channel. Obviously, a deeper channel is needed if high flow rate is the chief goal. It is also appropriate to note that, to our knowledge, no researcher has investigated channel height effects on EHD micropump performance, and only one study even recognized it as a design variable (Ahn and Kim 1998).

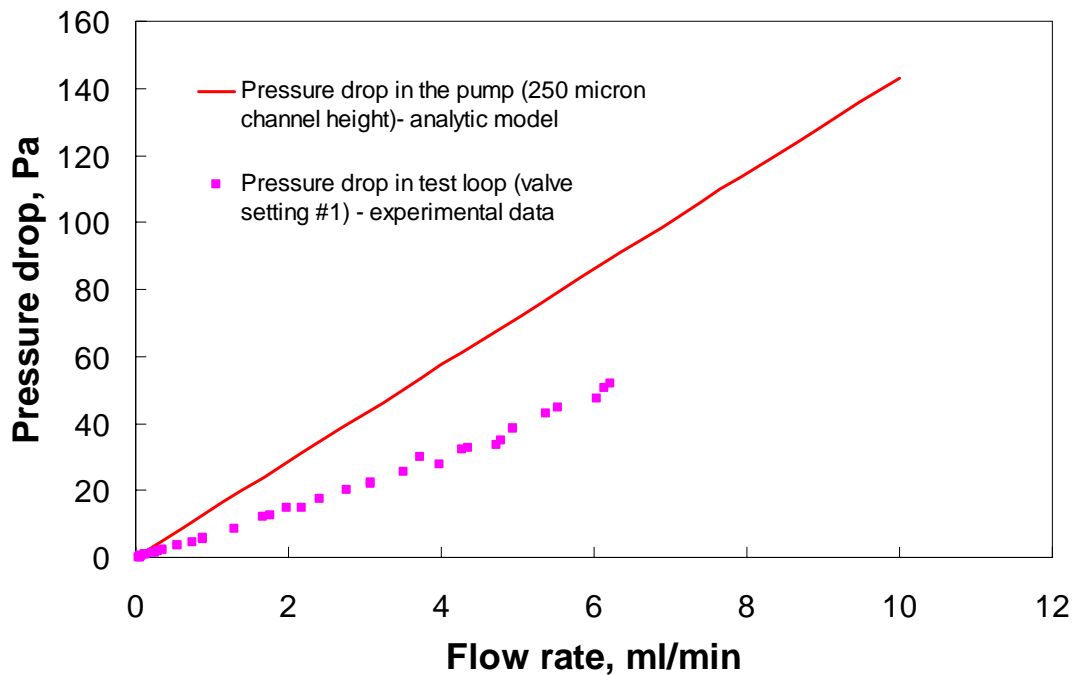


Figure 4-8 Comparison of experimental pressure drop vs. flow rate for the external test loop and calculated pressure drop for a micropump with a $250\ \mu\text{m}$ high channel.

In practice, evaluating a wide range of channel heights is impossible. Therefore, a few fixed gasket thicknesses were tested: $127\ \mu\text{m}$ ($0.005''$), $254\ \mu\text{m}$ ($0.01''$), $381\ \mu\text{m}$ ($0.015''$), and $508\ \mu\text{m}$ ($0.02''$). After packaging, these Teflon gaskets were measured to shrink by $10\text{-}20\ \mu\text{m}$, and thus reported channel heights were assumed to be: $120\ \mu\text{m}$, $240\ \mu\text{m}$, $360\ \mu\text{m}$, and $500\ \mu\text{m}$, respectively. A couple of tests were also performed with $762\ \mu\text{m}$ and $1,016\ \mu\text{m}$ gaskets, but they were not studied as extensively. Packaging the

micropump with gaskets of less than 100 μm was exceedingly difficult because the gaskets did not maintain uniformity in their thickness.

For numerical modeling purposes, an I-V curve is needed to determine the charge density boundary condition for the emitting electrode. The effect of channel height, for a given design, is expected to be evident for flow passages that do not have a fully developed charge distribution. Such is the case for channel heights less than 100 μm , as shown in Figure 4-9. This graph, plotted from numerical model-generated data, is for the static case, which has no convective current. Similar trends were observed for the dynamic case, in which the flow field does affect the electric current. The curve can be understood by looking at the charge density and electric field distribution within the channel (see Chapter 5). Migration current (the largest current component for the static case) is defined as the product of charge density, mobility, and electric field integrated over the cross-sectional area, and it reaches a constant value as the charge becomes negligible farther from the electrodes.

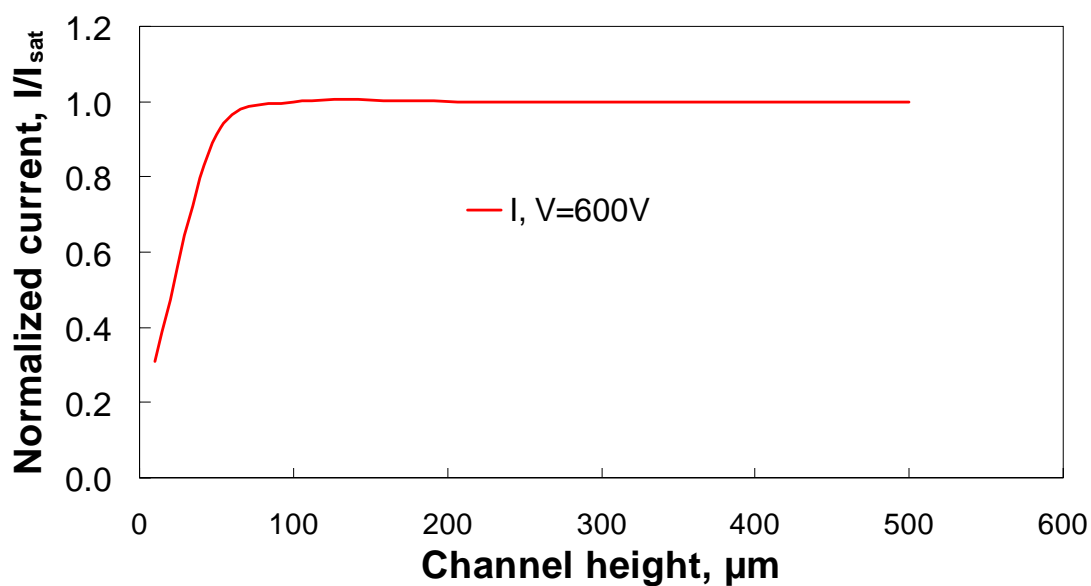


Figure 4-9 Numerical model of the dependence of electrode current on channel height ($V = 600 \text{ V}$, $\rho_{em} = 0.16 \text{ C/m}^3$).

Experimental static pressure data confirmed the current plateau. Figure 4-10 shows that for channel heights of 100, 220, and 450 μm , current values were within 15% of each other (current measurement accuracy was 0.5 μA).

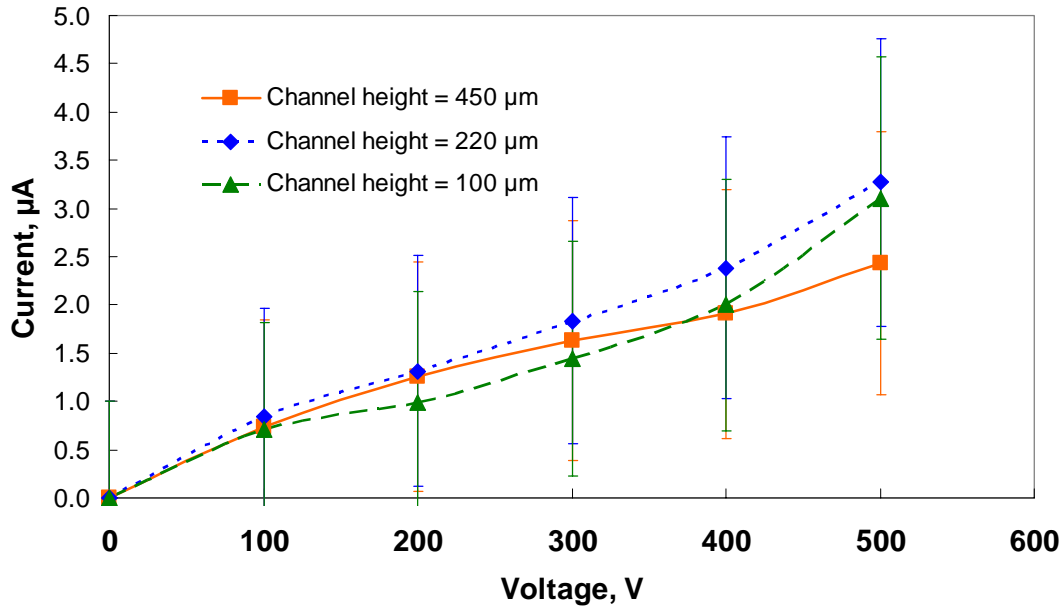


Figure 4-10 I-V curves for three channel heights under static pressure for 50f100 pumps.

Channel height also had little effect on the I-V curves, as Figure 4-11 illustrates.

The only other study that presented two channel heights claimed that electric current increased for higher channels as the convective current moved away from the electrodes (Ahn and Kim 1998). This statement is contradicted by our data and by our numerical simulations (Chapter 5), which show that current is independent of the channel height above 100 µm. Furthermore, Ahn's reported current data converge at higher input voltages, thus contradicting the author's claim.

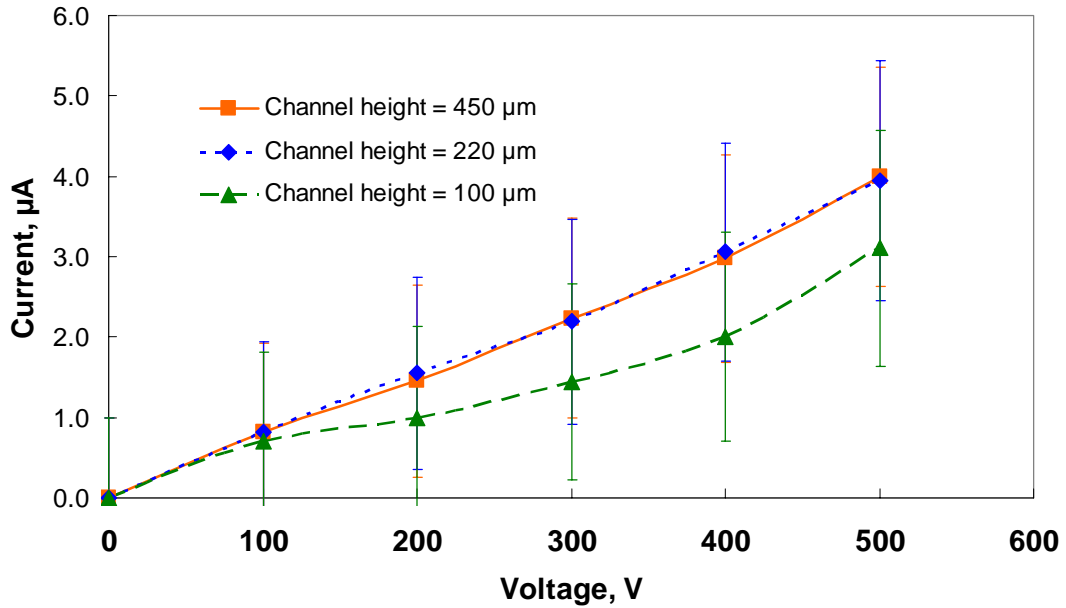


Figure 4-11 Effect of channel height on I-V curve under dynamic testing conditions (50f100).

Although channel height had little effect on the I-V curve, it is of importance to backflow pressure and flow rate. There exists an optimum channel height for maximum flow rate, since there are two competing forces that conversely depend on h_{ch} : flow resistance and the electric body force. This relationship is schematically presented in Figure 4-12 and is explained in Appendix B in more detail.

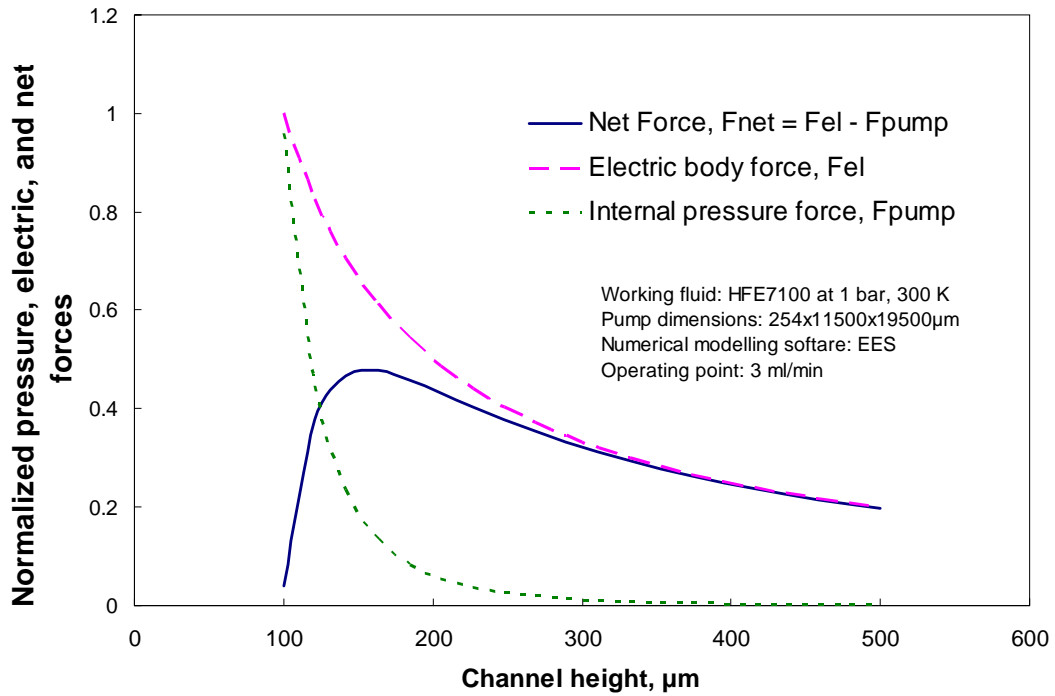


Figure 4-12 Calculated effect of channel height on the forces acting on the pumping fluid.

The experimental data verified the existence of an optimum channel height for maximum flow rate. The value was independent of the applied voltage and was close to 200 μm for the 50f100 micropump design. The exact value was not determined experimentally because of the impracticalities mentioned above.

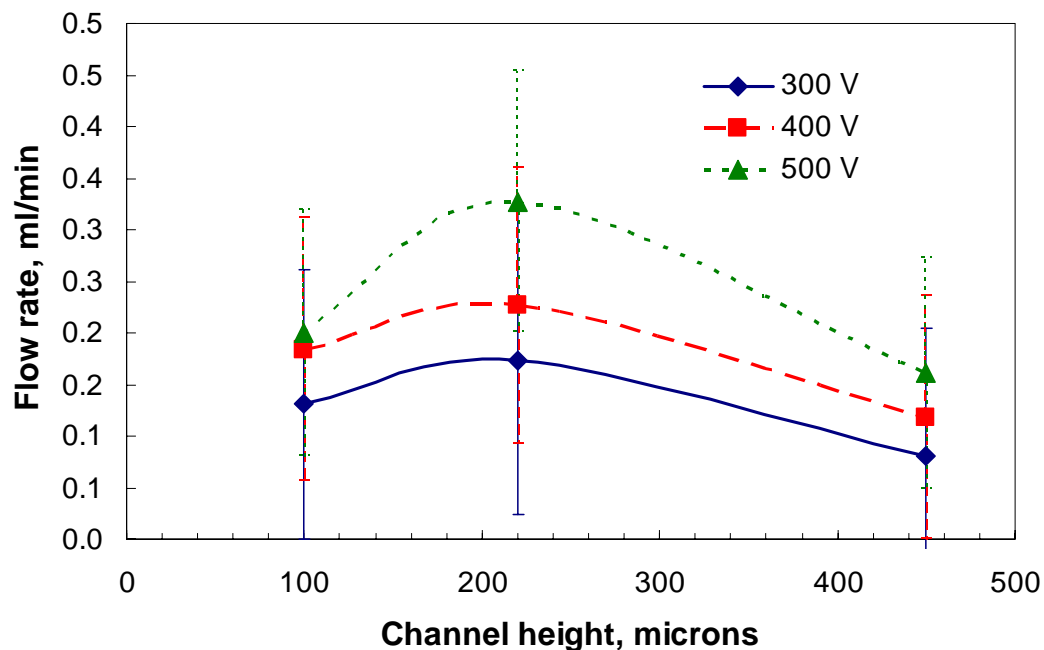


Figure 4-13 Flow rate vs. channel height (50f100), measured for different input voltages, showing an optimum channel height for maximum flow.

Assuming negligible circulation in the pump, backflow pressure is expected to decrease with channel height because with increasing distance from the electrode, both the electric field and charge density diminish. Such a trend was, in fact, observed experimentally, as shown in Figure 4-14.

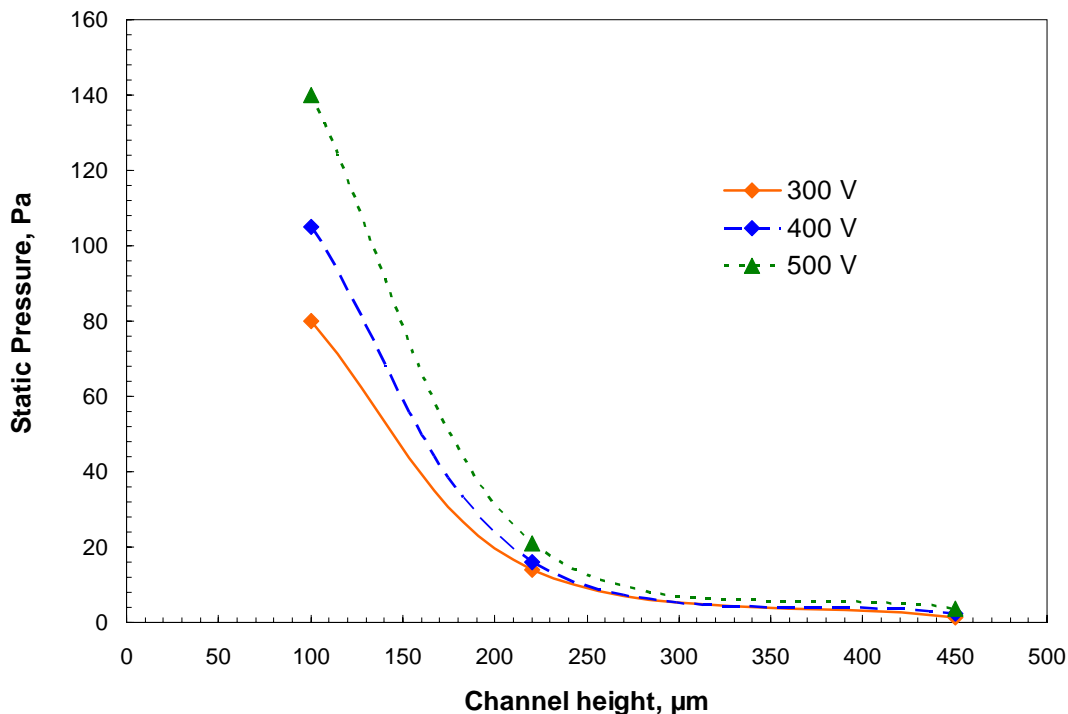


Figure 4-14 Effect of channel height on backflow pressure (50f100).

4.7.5 Electrode gap and spacing between electrode pairs

Electrode spacing has frequently been reported to be an important ion-drag pump design variable in the literature. The distance between the emitter and collector directly affects the magnitude of the electric field. For a fixed potential difference, electric field intensity is inversely proportional to the electrode gap.

This study found that for multi-stage electrodes, the electrode gap parameter alone could not account for the electric body force. The spacing between neighboring electrode stages had to be included in the calculations because the neighboring electrodes produce a force in the opposite direction, with collecting electrodes acting as emitters.

The local electric field can be calculated exactly only for ideal, flat-plate electrodes. For electrodes with curvature and surface roughness, the local micro-geometry can yield significantly different electric field distributions than would be

calculated using the average distance between the electrodes. Not only the average, but also the maximum electric field plays an important role in the generation of charge and body forces (Washabaugh, Zahn et al. 1989; Richter, Plettner et al. 1991; Darabi, Rada et al. 2002; Shooshtari 2004). A separate numerical simulation study was done to analyze maximum and average electric fields for the tested micropump geometries. Comparisons of the numerical and experimental data are presented in Chapter 5.

Results for the effect of electrode spacing on micropump performance were presented by considering performance factors for the same length of pump. Only one channel height (220 μm) was considered.

The dependence of current on electrode spacing will be discussed first. The issue is not trivial, as various investigators have reported contradicting information. For example, Rada (Rada 2004) showed that in static pressure tests, current was independent of electrode spacing. Yanada et al. (Yanada, Hakama et al. 2002) reported the same result for needle-mesh electrodes in a meso-scale ion-drag pump with six different oils. On the other hand, Stuetzer, Ahn, and Kojevnikov found that current increased with smaller electrode gaps (Stuetzer 1959; Ahn and Kim 1998; Kojevnikov, Motorin et al. 2001). Such contradictions need clarification. One possible explanation for the discrepancy could be that there is a difference between closed and open loop test systems, where the convective current component in the former affecting the total current. However, this explanation is negated by the work of Hakama and Kojevnikov, who worked with dynamic systems and reported similar currents for both the dynamic and static test conditions. Since researchers have used different working liquids and different electrode geometries (especially for the emitters), that could account for the difference in

their results. Explanation of this phenomenon could possibly be attained only by improving the understanding of charge generation process which is still a “gray-field,” as discussed in Chapters 1 and 5. In addition, the extensive work carried out by Bryan (Bryan and Seyed-Yagoobi 1990) and Barbini (Barbini and Coletti 1995) leads to the conclusion that the shape of the I-V curve depends strongly on the fluid and its purity, in addition to the electrode geometry.

For fresh pumps and liquid, the I-V curves depended on the electrode gaps. The smaller the distance between the electrodes, the lower the onset voltage (Figure 4-15). Though variations were observed, they were within the margin of uncertainty. Such a result is unexpected, as it was predicted that the dynamic case would yield an additional convective current component. The experimental data suggest that the convective current is either negligible or, more likely, constitutes less than 15% of the total current (the average uncertainty for the current measurements).

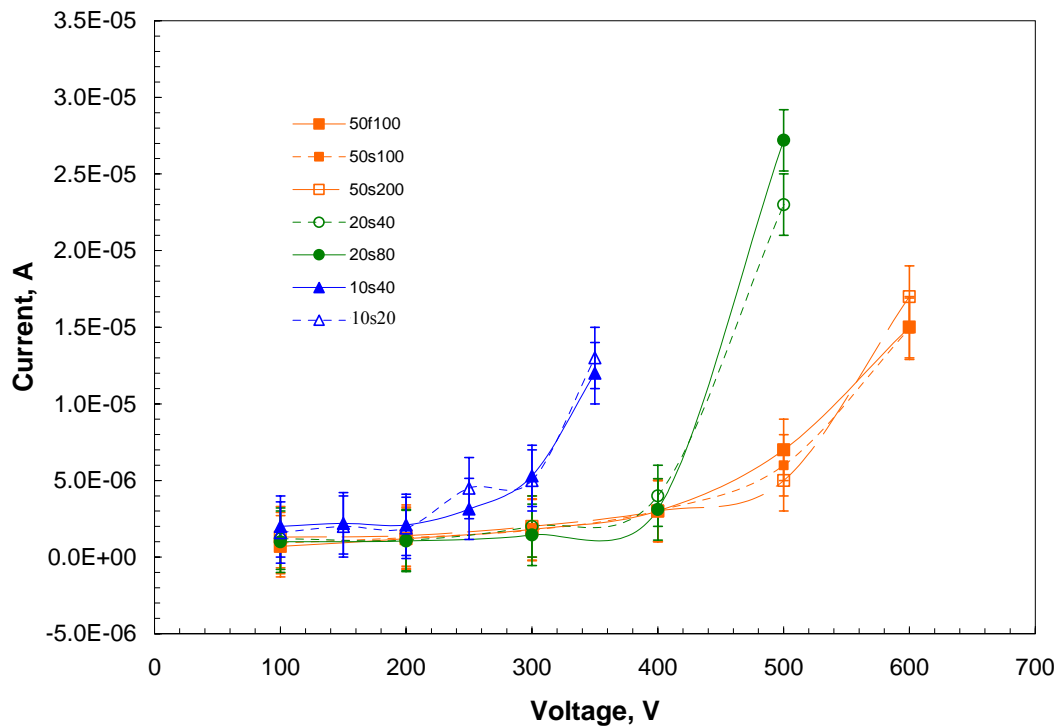


Figure 4-15 I-V curves for various micropump designs.

Results for ion-drag pumps reported in the literature show a strong linear dependence of the dynamic pressure on the current. This linear relationship was analytically predicted first by Stuetzer, Pickard, and Melcher (Stuetzer 1959; Pickard 1963; Melcher and Firebaug 1967) and later confirmed in many other experiments (Ahn and Kim 1998; Yanada, Hakama et al. 2002). The flow rate data in Figure 4-16 shows that q - V curves depend upon more than electrode gap alone. Comparing curves of the same color, which had the same electrode spacing, those with larger pair spacing (solid symbols) had higher flow rates.

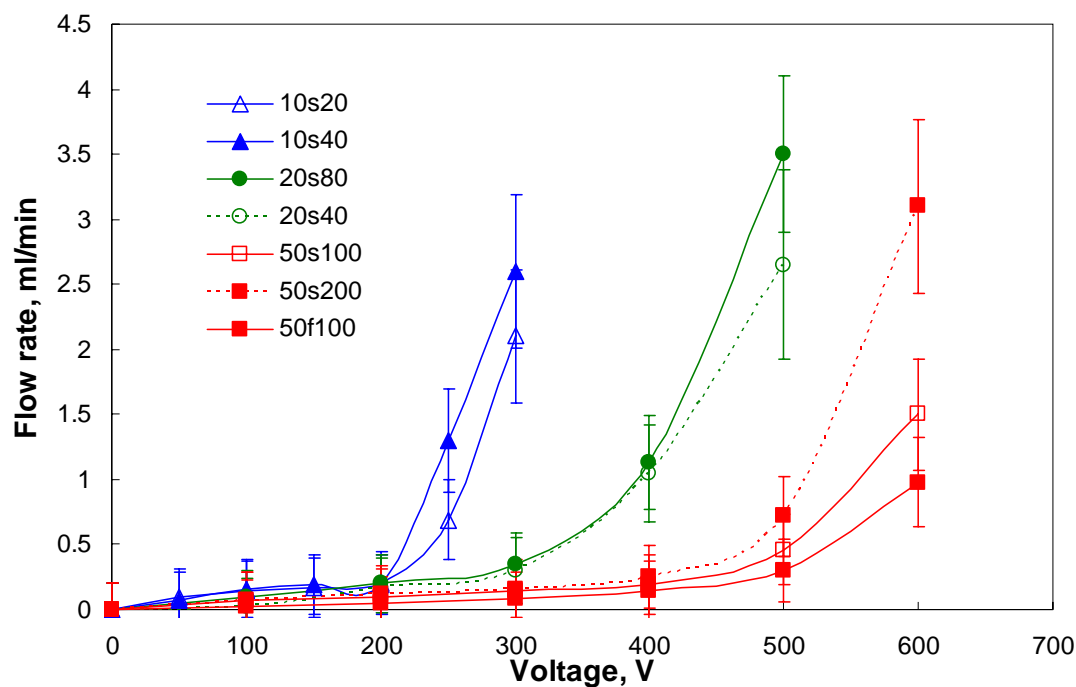


Figure 4-16 Pump design q-V curves (200 μm channel height).

Although their I-V characteristics were nearly identical, for electrode with the same spacing, the performance of saw-tooth electrodes was superior to that of flat electrodes. An increased inter-electrode pair distance enhanced performance as well, as expected from the larger maximum electric field. The electrode pair phenomenon is further investigated in the next subchapter.

The q-V curves in Figure 4-16 are for pumps of a fixed length (1.95 cm), so varying electrode spacing gave pumps with a different total number of electrode pairs. The dependence of flow rate on the number of pairs and pump length still needs to be elucidated, so the comparison in Figure 4-17 is for the same total input power.

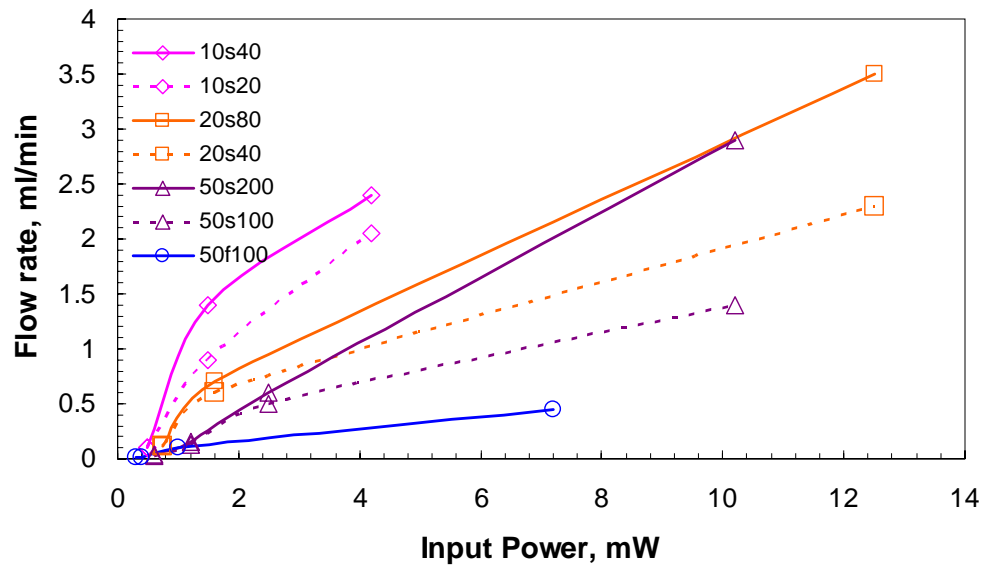


Figure 4-17 Flow rate vs. input power for various pump designs.

Table 4-6 Micropump design comparison for different methods of evaluation (1-best, 7-worst).

Pump design	Total flow rate vs. voltage	Total flow rate vs. power
10s20	2	2
10s40	1	1
20s40	4	4
20s80	3	3
50f100	7	7
50s100	6	5
50s200	5	6 (4 for high power)

The data in Figure 4-17 allow us to draw several conclusions.

- 1) Smaller electrode gaps provide higher flow rates for a given power input.
(This was expected as higher electric fields can be created between the electrodes under the same voltage.)
- 2) Larger electrode pair spacing improves the maximum flow rate by reducing the backflow pressure effect caused by electric fields opposite to the main flow direction.
- 3) Sharpened emitters increase flow by locally concentrating the electric field.

So far the test results have been shown for both static and dynamic cases.

However, several studies reported in the literature based their evaluation of ion-drag pumps on open loop test conditions. Such experiments are significantly easier to perform but provide an incomplete picture. Further conclusions about effectiveness, power, and flow rates based on these data are not correct, as this study and several others show (Kojevnikov, Motorin et al. 2002; Yanada, Hakama et al. 2002). The difference in pump performance under static and dynamic cases may result from two factors. First, in the dynamic case, convective current consists of the free charges present in the liquid. Second, the electro-convection circulatory flow patterns change from static to dynamic test conditions. To complicate things further, channel height plays a significant role in electroconvection flow, as was reported in several papers (Atten, Elouadie et al. 1989; Castellanos and Agrait 1992).

Even though this study focuses on the dynamic performance of ion-drag micropumps, static tests were carried out for estimation of maximum head generation and a quick evaluation of the pump's operability. These tests suffered low repeatability for different samples of the same design and from inadvertent variations in channel height. Such erratic performance is not unique to this study. Researchers investigating electro-convection indicated various flow instabilities in the EHD phenomenon. As numerical

work below will indicate, significant recirculation occurs under static conditions, while it is dampened under dynamic conditions. Backflow pressure data that were repeatable in a micropump with a $220\ \mu\text{m}$ channel are shown in Figure 4-18. Unlike for flow rate, pumps with larger electrode pair spacing had worse performance (compare 20s80 with 20s40 and 50s100 with 50s200).

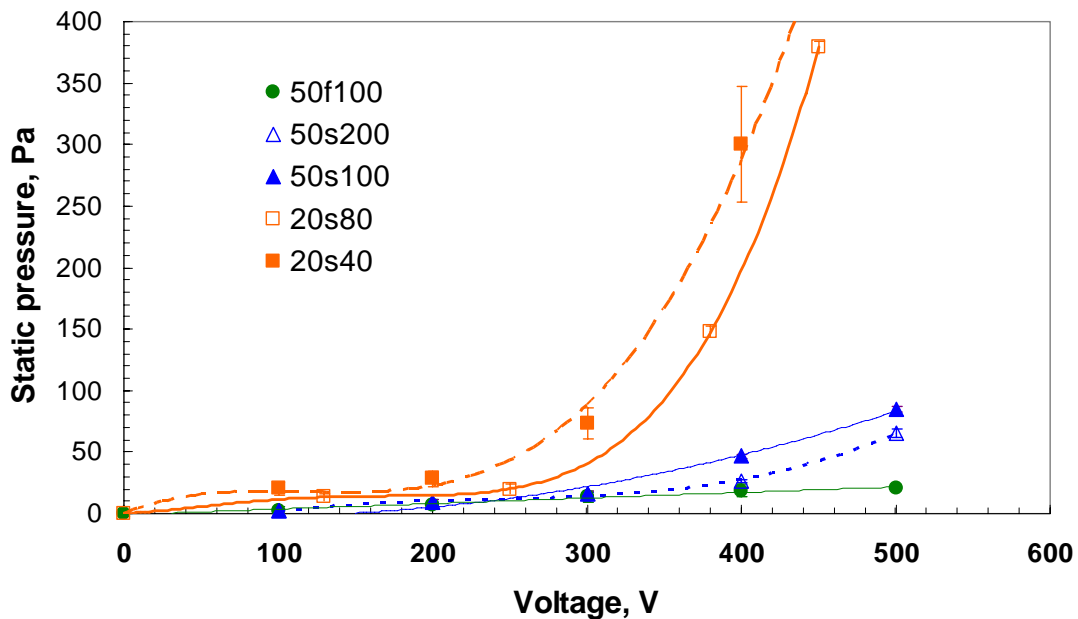


Figure 4-18 Backflow pressure dependence on electrode spacing (channel height $220\ \mu\text{m}$).

4.7.6 Electrode pair spacing, further investigation

Distance between electrode pairs is reported using two approaches: as a multiple of electrode spacing and as the absolute distance in micrometers. For example, 50f100 had 2x and $100\ \mu\text{m}$ electrode pair spacing.

In the region between the emitter and collector, the physics is understood, in brief, as follows: charge is injected at the emitter electrode and is propelled by the electric field to the collector, where it is reduced. However, the experimental results suggest that if the

emitter edge facing the previous collector is sharp, a large enough field can be created to enable charge to be injected in a reverse direction to that of the fluid flow. An opposite-direction pumping force is thereby generated. A graphical example of this phenomenon is presented in Figure 4-19. In addition, the charge might not be fully reduced, and the remaining charge may reverse direction and travel to the previous neighboring collector, subject to the reversed electric field (which is weaker because of larger distance). The net effect is reduced overall flow rate and pressure head.

A single stage ion-drag micropump is impractical for most commercial applications, as it generates insufficient pumping head and flow. Thus, multi-stage pump designs are required, which suffer from the backflow effect. Backflow cannot be eliminated while operating with DC input power, but it can be reduced by increasing the gap between stages. The fixed length of the pump and fluid viscous forces, which dampen the motion, control how much it can be increased. Based on such reasoning, an optimum electrode pair spacing exists. Furthermore, since the net force takes into account both the electrode gaps (emitter-collector and emitter-neighbor collector), it is wiser to monitor the ratio of these distances.

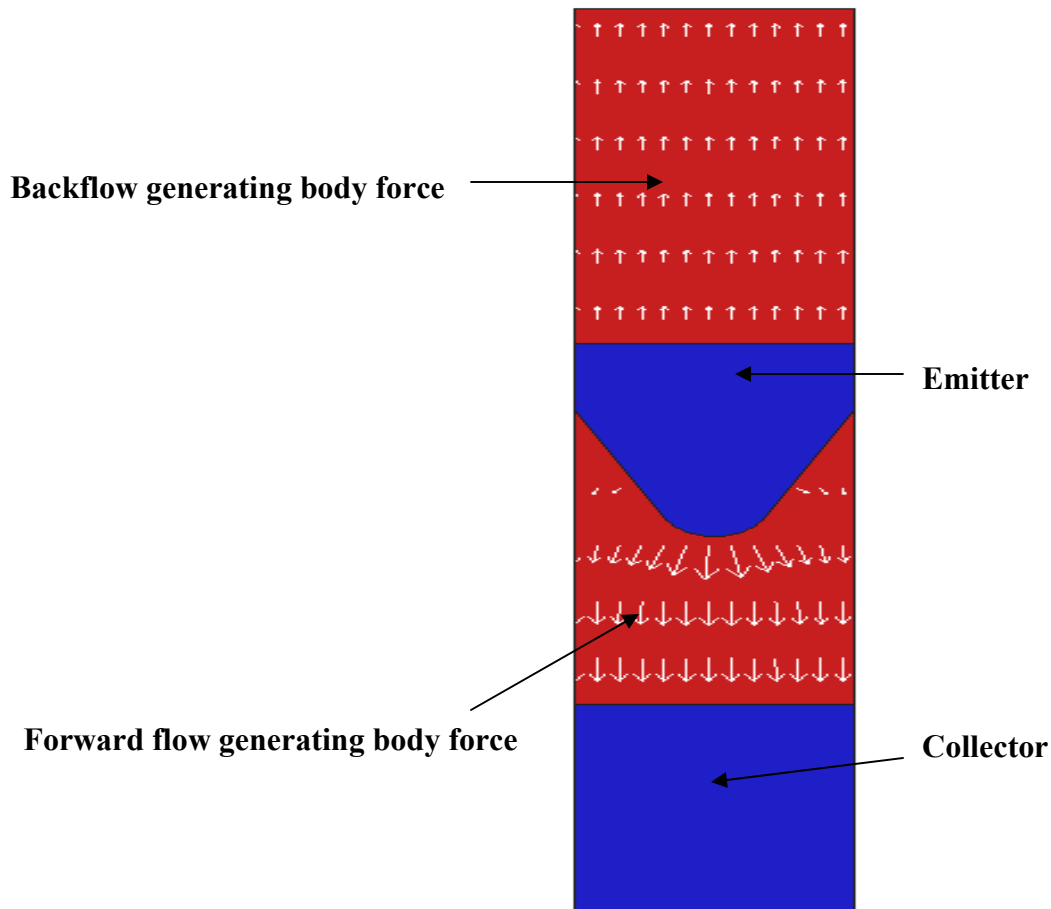


Figure 4-19 Backflow force illustration for a section of a saw-tooth electrode pair (not to scale).

As further evidence for the theory of an optimum d_{pel} , a normalized flow rate curve based on numerical modeling of the 50f100 design (later presented in Chapter 5) is shown in Figure 4-20. The data in Figure 4-18 would suggest that this optimum was not reached in these designs. Based on the numerical model, the maximum should occur for a ratio of electrode pair spacing to electrode gap of 8. This would require our designs to be 50s400 and 20s160.

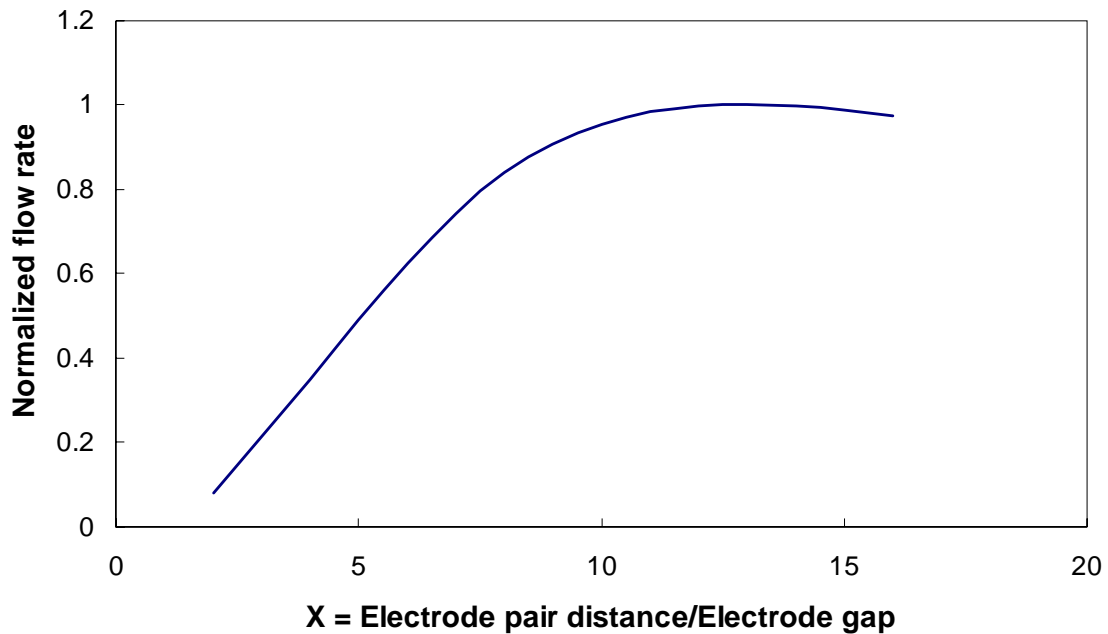


Figure 4-20 Predicted dependence of non-dimensionalized static pressure and flow rate on the electrode pair gap (based on numerical modeling of the 50f100 design with a 200 μm channel height).

4.7.7 Electrode shape (2D and 3D)

Electrode shape is the design factor that has received the most attention from EHD researchers. To increase the electric field, they have created needle-tip, razor-edge, or thin wire electrodes spaced at distances down to tenths of a millimeter (Pickard 1963; Barbini, Bozzo et al. 1993; Asano and Yatsuzuka 1999).

With microfabricated pumps, full scale 3-D features are limited, since microfabrication techniques only allow features to protrude out-of-plane in one direction. Therefore, Darabi (Darabi, Rada et al. 2002) proposed saw-tooth emitters.

It is important to understand the concept of small curvature geometries. In theory, a 90° edge would have sufficient sharpness to create a field of infinite magnitude. Electrostatics theory does not consider microscale structure and assumes infinite electric fields at any discontinuity. However, in reality no perfect edge exists. Curvatures can be

on the submicron scale, but they still have some finite radius. (This notion will be further discussed in Chapter 5.)

As various graphs have already shown, the saw-tooth electrode came out as a winner over the flat one in all aspects of performance: pressure head, flow rate, and efficiency. The effect did not depend on channel height, electrode thickness, or substrate material. This was in a good agreement with experimental results on ion-drag pumps reported in the literature.

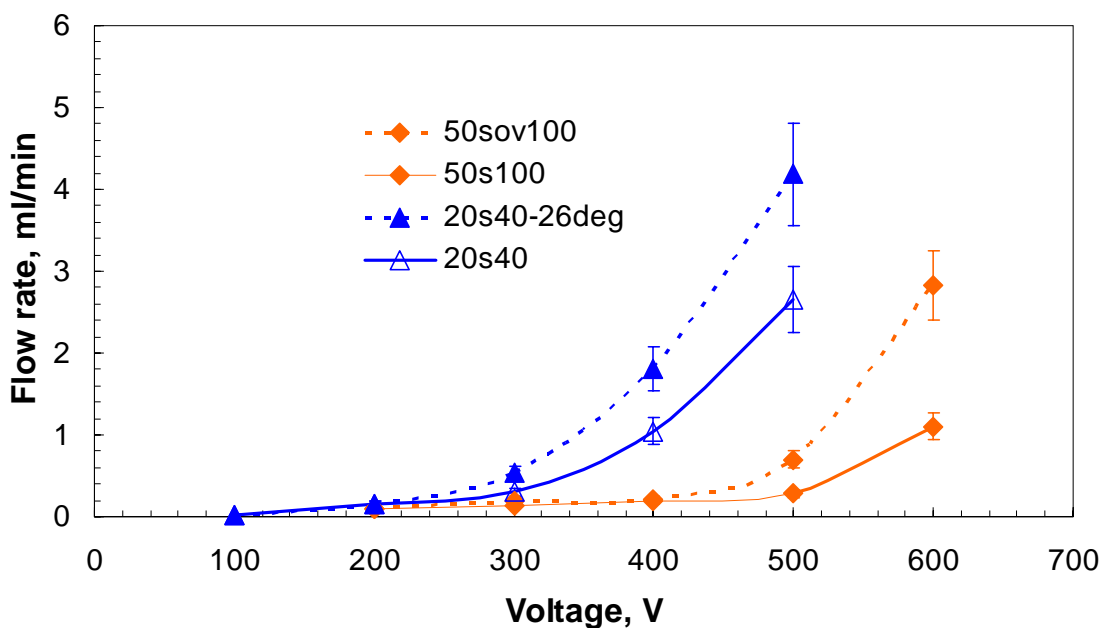


Figure 4-21 Effect of emitter shape on flow rate for the four electrode shapes (channel height = 200 μm).

Next, saw-tooth overhang (sov) and planar saw-tooth (s) electrodes were compared. Only one channel height was tested, as overhang electrode fabrication and reliable operation proved to be challenging. Results for the dynamic case are shown orange in Figure 4-21 and for the static case in Figure 4-22. The overhang electrodes

performed twice as well for flow and approximately 25% better for pressure, presumably from a sharper emitter tip.

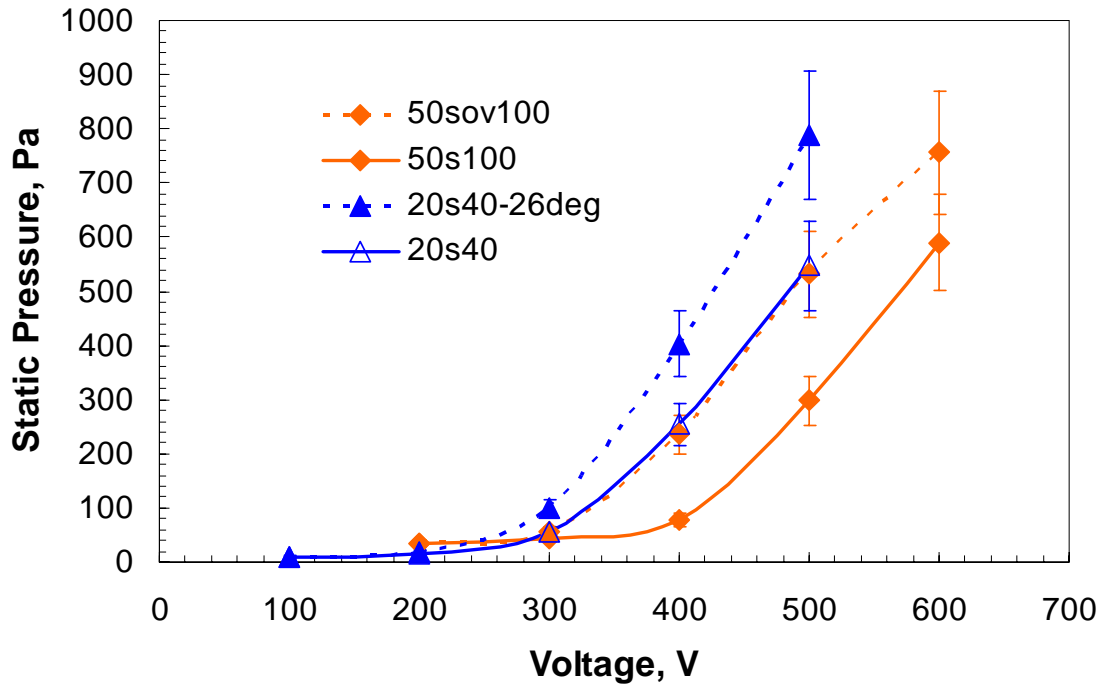


Figure 4-22 Emitter shape effect on static pressure (overhang and sharper tooth)

Saw tooth electrode angles were chosen based on electric field simulations that took into the account the pump's fixed width. A sharper electrode tip (smaller angle) should create more charges and larger maximum fields, and, in addition, there would be more injection points per unit width. The number of thin needle-like electrodes is limited by fabrication and mechanical durability. Figure 4-22 and Figure 4-24 show that the 26-degree tooth electrode outperformed the 53-degree one. Fabrication of sharper teeth was not successful. On top of that, it was observed that further narrowing the electrode tip did change the actual radius of curvature at the tip because of the limited resolution of the microfabrication mask.

4.7.8 Characteristic curves and efficiency optimization

As was discussed at the beginning of this chapter, characteristic curves are essential for the comparison of pumps whose operation is based on different physical phenomena. They represent the capability of the pump to deliver flow and overcome external flow resistance (pressure drop). A typical characteristic pump curve is created at a fixed level of input power. However, due to the complexity of harvesting data which had the same input power levels, the input voltage is held as the argument for the output variable curves.

Figure 4-23 shows the flow and the pressure for a series of voltages, connected by a straight line, and overlays the efficiency curve. The improved performance of the pump with increasing input voltages is at the cost of an increase in power consumption, which results in a flattening of the efficiency. (The definition of efficiency was given in equation (2-19)). Note that efficiencies in ion drag pumps are low. (The notion of useful power does not include overcoming the internal pressure drop, which has been shown in Figure 4-8 to be of the same order of magnitude or larger than the external flow resistance.)

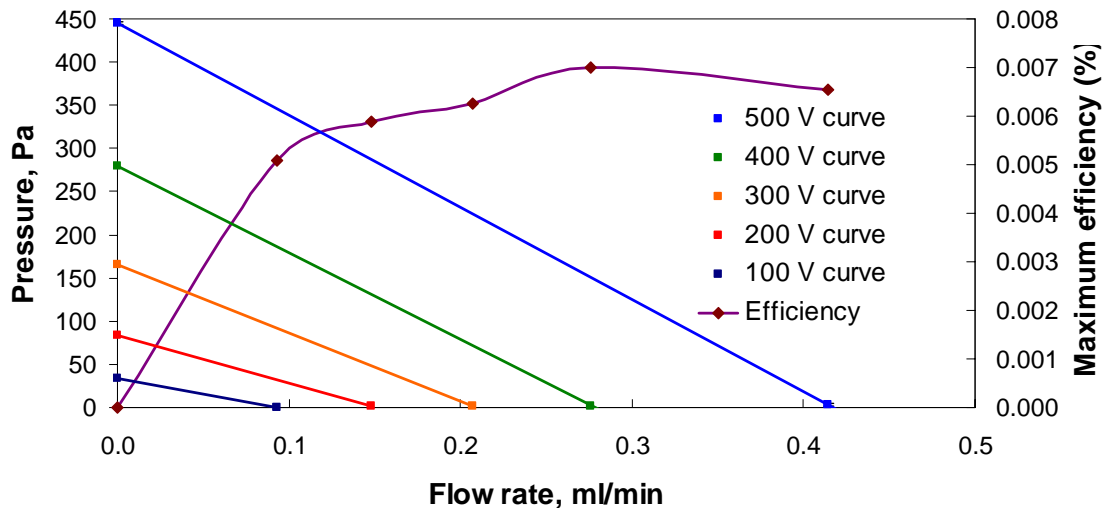


Figure 4-23 Typical characteristic curves for the ion-drag micropump (50f100-100)

In the present work, 9 tested designs with an average of 3 channel heights per design yielded a total of 27 curves. They are helpful if used in the context of some specific application but are utterly confusing if pump designs have to be compared. The solution to this problem is to fix all of the design variables and compare one parameter at a time. An example of such an evaluation is presented in Figure 4-24, where a fixed input voltage and channel height were used for five pump designs. The downside for this method is the limitation in operational input voltages. Pumps with smaller electrode gap need a lower voltage to reach dielectric breakdown of the working liquid, and thus only a limited range of input voltages overlap (electric field cannot be used, since both maximum and average electric fields play a role).

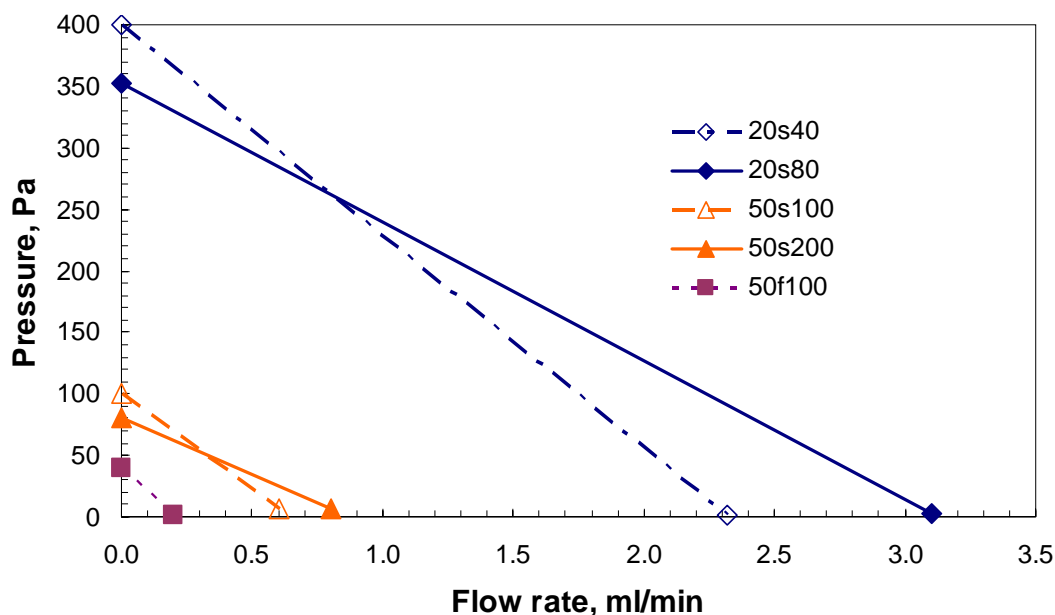


Figure 4-24 Characteristic curves for 5 designs with a fixed input voltage (500 V) and channel height (100 μm).

Figure 4-24 states that decreasing the electrode spacing significantly increases the performance of the pump. Optimization of the gap between electrode pairs has to be done for either flow rate or pressure head, not both.

4.8 Pump reliability issues and analysis

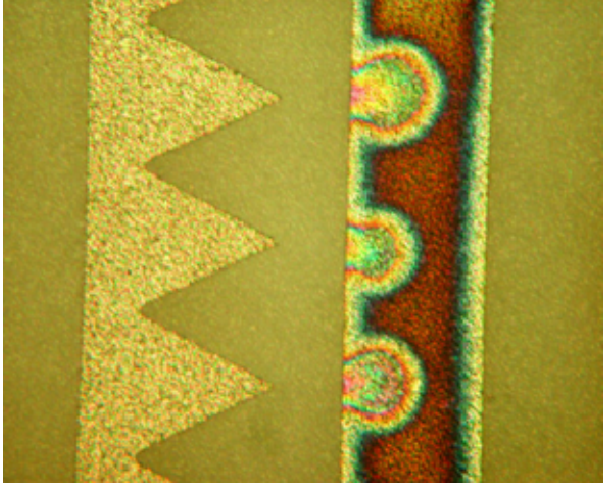
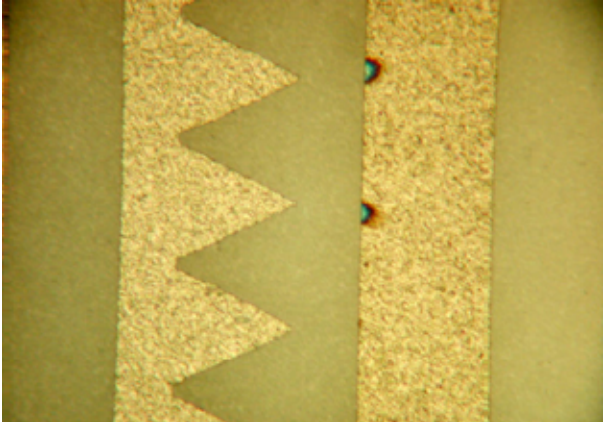
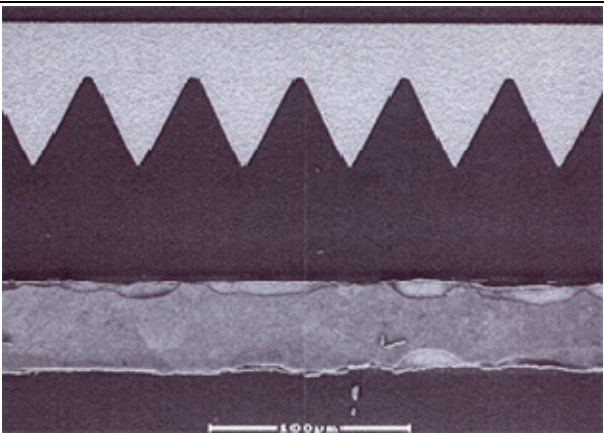
In EHD, the electrical, chemical, and mechanical worlds influence each other through coupled variables such as electric potential, charge density, temperature, and fluid velocity. These interactions are modeled as described in Chapter 2. However, our fundamental understanding of EHD is still limited, especially where microscopic level phenomena are concerned. Several of the processes that still require clarification are: charge injection under high electric fields, electrochemical processes on the surface of electrodes and in the bulk liquid, charge assimilation on the collecting surface, electric

fields near small radii of curvature, and EHD flow instabilities. This study carried out careful monitoring and investigation of the electrochemical processes taking place on the electrode surface and combating unstable performance of the pumps.

4.8.1 Electrode degradation

Ion-drag pumping requires > 100 kV/m, which can alter liquids and solids on the molecular level, creating barriers to charge injection and reduction. At the beginning of this study, experimental results showed large variations in pump performance over time, even for the same device. When opened after operation, the pump electrodes had visual markings of various shapes and colors, mostly situated on the collectors, directly in front of emitter saw-teeth. Electrode surfaces were photographed with a digital camera attached to a microscope. Several samples were investigated using environmental scanning electron microscopy (ESEM). The resulting pictures are displayed in Table 4-7.

Table 4-7 Deterioration of electrodes.

Electrode surface	Notes
 <p data-bbox="565 821 602 852">#1</p>	<p data-bbox="911 317 1430 737">Taken with digital camera and 40x microscope objective. Electrode is Cr/Au on alumina. Pump operated with negative polarity on the emitter (saw tooth) electrode and a grounded collector. Emitter electrode displays the same color and texture as before the test. Total test length 10 hours.</p>
 <p data-bbox="565 1318 602 1350">#2</p>	<p data-bbox="911 877 1425 1024">Taken with digital camera and 40x microscope objective. Same conditions as #1 except that test lasted only 1 hour.</p>
 <p data-bbox="565 1833 602 1864">#3</p>	<p data-bbox="911 1367 1430 1570">Electrode surface taken with the ESEM. Electrode material: niobium. Same test conditions as #1. Collector damage visible in two directions.</p>

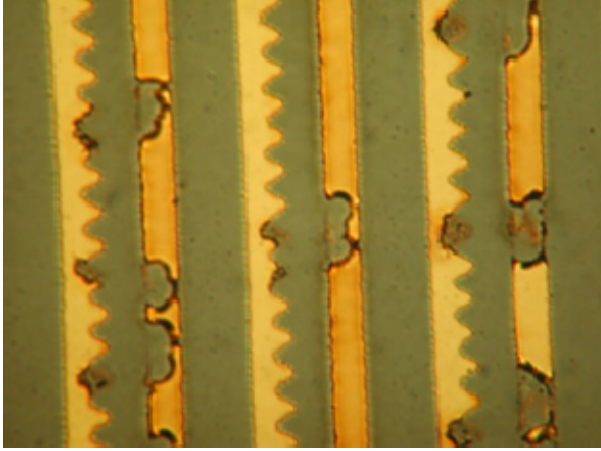
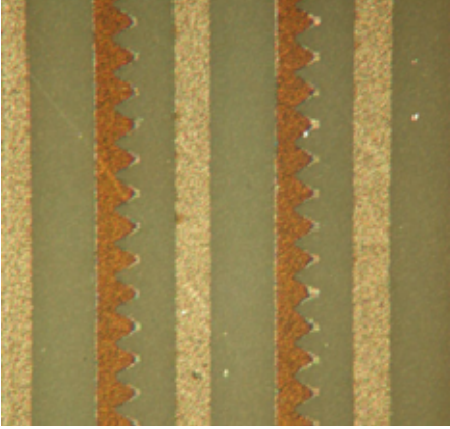
 <p style="text-align: center;">#4</p>	<p>Test conditions and materials same as #1 except for operational power, which was 200 V higher. Shorting and discharge yielded high temperatures that melted parts of the electrodes.</p>
 <p style="text-align: center;">#5</p>	<p>Test conditions and material the same as in #1 except that the polarity of the electrodes was reversed. Damage observed on the saw-tooth electrode.</p>

Table 4-7 illustrates the damaging nature of the EHD ion-injection phenomenon. Though the existence of “some electrochemistry” was acknowledged by several authors (Bologa, Kozhukhar et al. 1999; Shoostari 2004), no work was carried out to identify or even to observe the damage. This is the first known study to offer a discussion on this phenomenon (see the ion-drag summary table in Chapter 2).

Sample #1 display some deterioration on the collecting electrode right in front of the emitter tips. The extent of damage is represented by variation in color and shape of the corrosive spots. Several investigators claim that electrochemical reactions take place during ion emission (Zhakin 1999; Darabi, Ohadi et al. 2001), which would be expected

to damage the emitter. Our results show damage on the surface of the collector, where charges carried from the emitter are recombined. The fact that only the collecting electrode displayed the deterioration suggests that occasional electrons, instead of being returned to the electric current path, instead participate in chemical reactions with the impurity molecules like oxygen or cause dissociation of the working liquid into reactive fragments.

The degree of damage depends on both the input power and the test time. Sample #2 shows how much smaller the damage was on the electrodes that underwent testing for 1 hour instead of the 20 hours for sample #1. Sample #5 shows that when voltage polarity is reversed, corrosion switches from one electrode to the other. In this case, damage on the saw-tooth shaped electrodes was more uniform because the emitting electrode was straight.

Sample #3 was viewed using ESEM, which helped us to better understand the nature of the damage. The picture of #3 shows that the profile of the collector electrode had changed. Profilometer readings indicated that also, and are sketched in Figure 4-25 (the profilometer did not have a digital output). A substantial increase in collector height was observed, confirming the hypothesis of material deposition rather than material removal from the electrode.

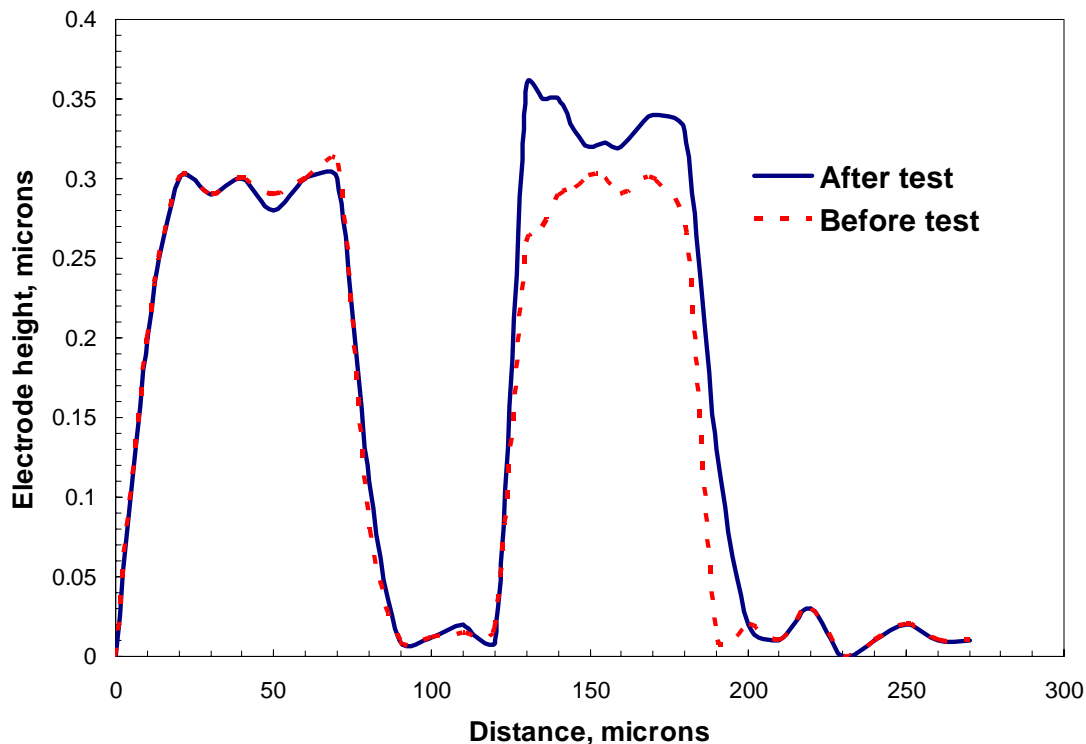


Figure 4-25 A sketch reproducing a scan taken with a mechanical profilometer of the electrodes before and after pump operation. The first bump represents the height of the emitting electrode and the second that of the collector.

Finally, picture #4 had another important message: high input power for extended periods of operation can result in dielectric breakdown within the liquid, leading to uncontrollable discharge between electrodes. This was actually observed in the form of sparks. The high level of energy released as heat melted parts of the electrodes.

Further analysis of electrode degradation was carried out using energy dispersive spectroscopy (EDS) on the niobium electrodes. EDS bombards the sample with electrons and counts the resulting X-ray photons at each energy level. The energies are characteristic of each element, allowing elemental analysis. Spectra taken from the collector electrode before and after pumping are shown in Figure 4-26 for two channels with impinging electron energies that best excited the elements present on the surface. Channel 1 (LDE1) clearly displays the presence of oxygen (O), fluorine (F), and carbon

(C) after the test, which were absent before. The HFE7100 molecule includes one oxygen atom. However, it is more likely that the source was oxygen dissolved in the working liquid. On the other hand, fluorine and carbon are unlikely to be present in any impurity and arise from the HFE7100. The presence of two highly reactive oxidizing agents, fluorine and oxygen, well explains the reactions occurring on the electrodes.

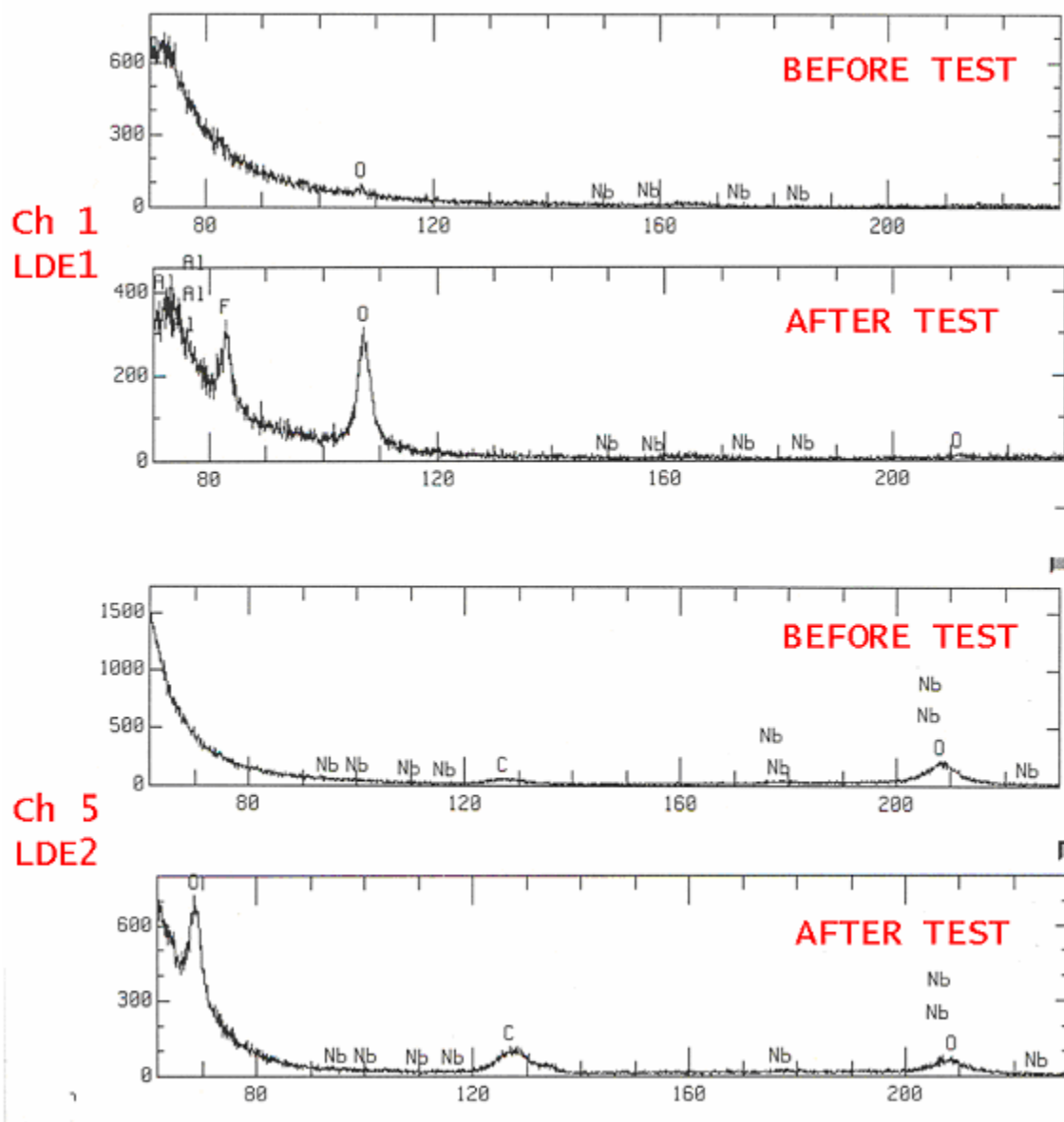


Figure 4-26 Elemental analysis of the collector electrode using EDS. Two channels using different excitation energies show the relative abundance of specific elements on the substrate.

Another quantitative elemental analysis was performed with wavelength dispersive spectroscopy (WDS), which also identifies and counts X-rays based upon their wavelengths. Results are tabulated in Table 4-8.

Table 4-8 Elemental analysis for emitter and collector electrodes obtained with WDS. All values are relative percentages by weight.

	Emitter (%)		Collector (%)			
	Nb/Al	O/C/F	Nb/Al	O	C	F (%)
Before the test	97.4/2.6	0/0/0	98/2	0	0	0
After the test	92.6/0.4	5.4/1.6/0	78.2/0	15.8	2.1	3.9

Table 4-8 presents the relative amount of each element on the emitting and collecting electrodes before and after pumping. Values are presented in weight percent. Before the pump test, the surfaces showed only the electrode metals Nb and Al. After the test, the collector displayed significant increases in O, F, and C (reducing the relative weight of Nb). On the emitter, O and C were present in smaller amounts, and F was not present at all.

Based on these results, it became clear that purification of the working liquid and isolation of the system were crucial to ensuring the reliability of EHD pumps. This influenced redesign of the test loop, fluid charging procedures, and material selection (as discussed in Chapter 3).

4.8.2 Working fluid performance with EHD phenomenon

HFE7100 favors EHD pumping due to a good balance of properties: low viscosity, relatively high dielectric constant, and moderate ion mobility (Table 3-5). It has three CF₃ moieties directly attached to the central carbon atom, and one attached

through the oxygen atom (Figure 3-1). If ionized, this molecule could potentially produce many fragments, some of which could be reactive.

The test liquid was analyzed before and after testing. High performance liquid chromatography (HPLC) was used to separate the fluid components, and a Finnigan LCQ mass spectrometer, which can detect as few as 100 ppb, recorded their mass to charge (m/z) ratios. Unfortunately, analysis of liquid before and after pump operation was unable to detect a significant difference. Thus, it may be that no large scale changes occurred on the molecular level, or that most of the fragments deposited on the electrode surfaces. Alternatively, it may be that such changes could be only temporary. Note that the samples had a 5-10 hour wait time before analysis by mass spectrometry.

A conclusion derived from electrode surface elemental analysis is that the working liquid does participate in EHD-induced electrochemical reactions, and that purification is essential to higher reliability. It should be added that two levels of purification have to be achieved: chemical and particle. For the former, the vendor plays the biggest role by manufacturing the highest purity liquid it can. Closed containers must be used for transportation and storage to prevent exposure to the ambient environment and the uptake of atmospheric gasses such as oxygen, water vapor, and carbon- or nitrogen-containing compounds. Unfortunately, complete isolation of the liquid from the ambient is not practically possible as the storage container has to be opened and fluid transferred to the test loop reservoir. To combat this, a local degassing process was performed by boiling the HFE7100 and removing separated non-HFE gasses from the reservoir prior to charging of the fluid to the test loop. The procedure took 1-2 hours, during which HFE-7100 was brought to its boiling temperature (61 °C at 1 atmospheric

pressure) and allowed to condense over a long tube connected to a second liquid reservoir located higher than the test loop charging reservoir. Dissolved gasses were released upon condensation.

The second source of trouble was particulate impurities. Though carefully filtered by the manufacturer, they were still found to deposit on the electrodes. From the theory of electrostatics, it is well known that dielectric particles, once exposed to an electric field, polarize and resist the field. In the presence of charges surrounding the particle, misbalance in charge symmetry occurs and these particles become subject to electric body forces produced by the external field. In short, these particles become attracted to the electrodes just like dust in commercial ionization air purifiers. In our study, they were attracted to the electrode where the highest electric field was present.

Impurities could have the following “side effects” which would reduce EHD pumping.

- 1) Some impurities can take up electrons from the emitting electrode and thus prevent their interaction with the working fluid.
- 2) Electrons emitted by the impurities could collide with other impurities.

The entire test loop can be a source for impurities, in addition to the ones present in the liquid. To solve this problem, various improvements in handling of materials and preparation prior to test runs were made as described in Chapter 3. Among them were: multiple flushes of the system, filtering of the liquid, and cleaning and assembly of parts in a clean room environment. Such approaches helped to improve the reliability of the pumps and to increase the repeatability of test results.

4.8.3 Charge behavior and electric breakdown

As explained earlier, electrohydrodynamics is a complex multiphysics problem. In addition to the compound nature of this problem, lack of understanding of several physical phenomena limits the derivation of a comprehensive EHD theory. The leading enigmatic issues are: charge generation, transport, and reduction. An in-depth discussion of the theories was given in Chapter 2, while this chapter offers several observations and explanations of space charge and dielectric breakdown in the current study.

During initial tests, large-scale instability in electric current was observed: for input voltages above the onset value (see description of the I-V curve in Chapter 2), current took 10-15 hours to reach a steady state that was up to one order of magnitude lower than the initial value. Results are presented in Figure 4-27. For voltages below onset, the current increased to a saturation level, as shown in Figure 4-28, and it typically took about 1-3 hours for that to take place.

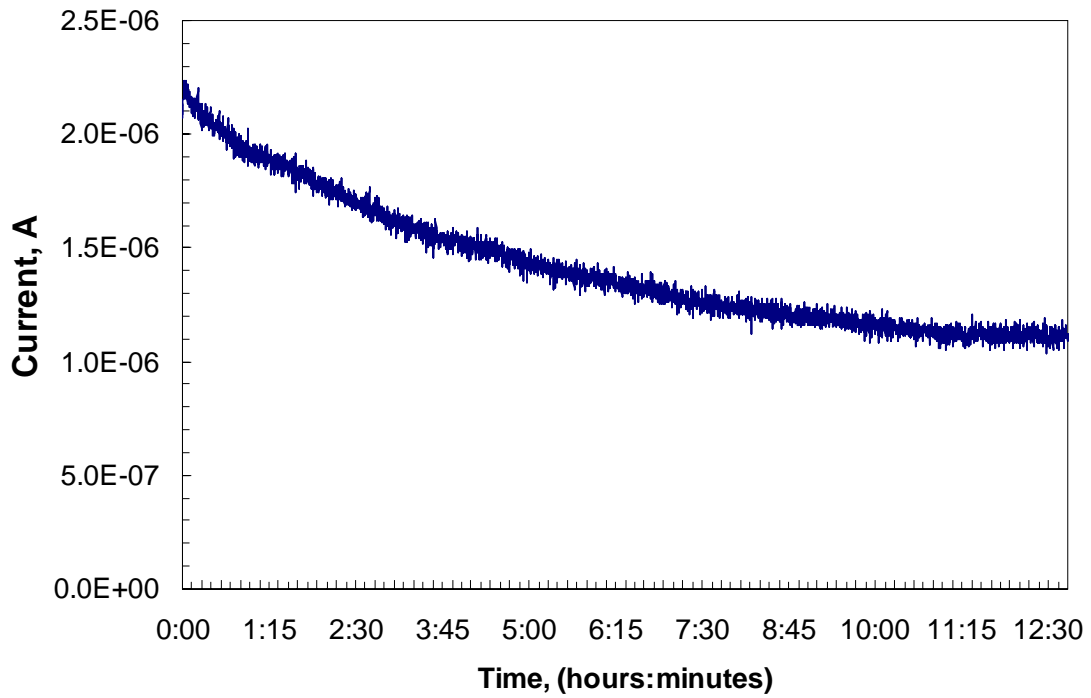


Figure 4-27 Current behavior for a fixed input voltage above the onset of EHD.

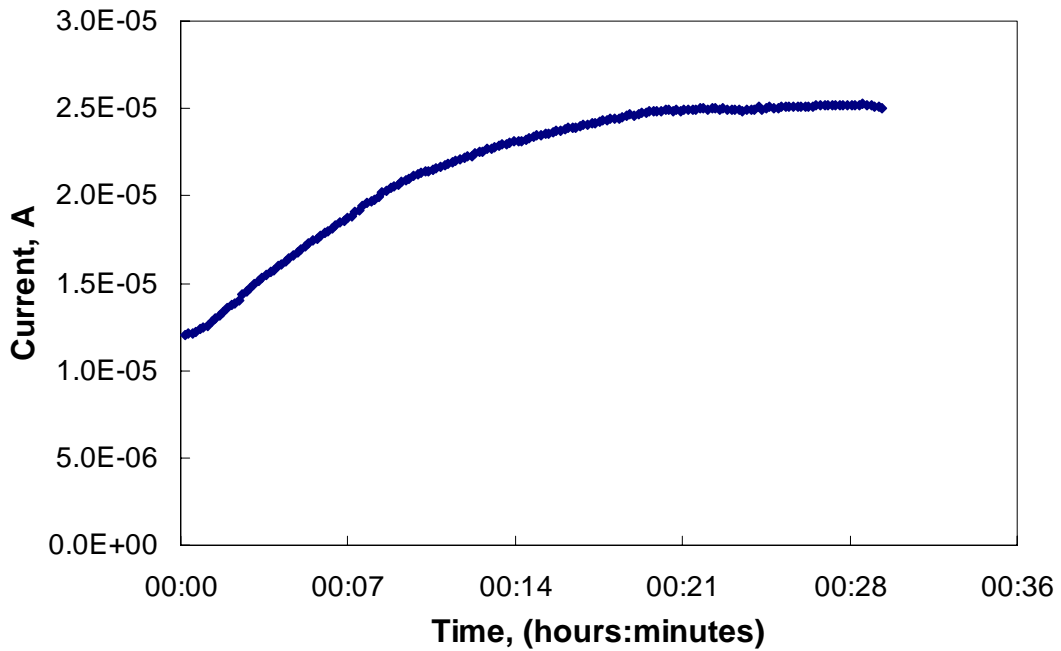


Figure 4-28 Current behavior for a fixed input voltage below onset.

There are two hypotheses to account for this behavior: one attributes these effects to impurities and another relates the phenomenon to space charge limitations. Impurities can potentially have a charge that over time gets neutralized, causing a decrease in current. Conversely, other types of impurities could charge up. This, however, that does not explain why there is an effect of the onset voltage. The other explanation is based on the fact that above the onset voltage, field emission is limited by space charge. Of course, deposition of material onto the surface of the electrodes could also significantly influence both emission and reduction of the ions participating in the EHD pumping phenomenon.

To further investigate the current decay, a test was performed that looked into how long it took for the charge to be reduced without any electric field acting on it. Results are presented in Figure 4-29 where, for a fixed input voltage, the current underwent the same decrease. The voltage was turned off for a short period of time and turned on again. After that the electric current returned to the same value it would have had if the voltage had stayed on. Extended periods with the voltage turned off continued to show the same decay. It took about 10 hours (not shown) before a powered down pump would re-produce the initial value of the current.

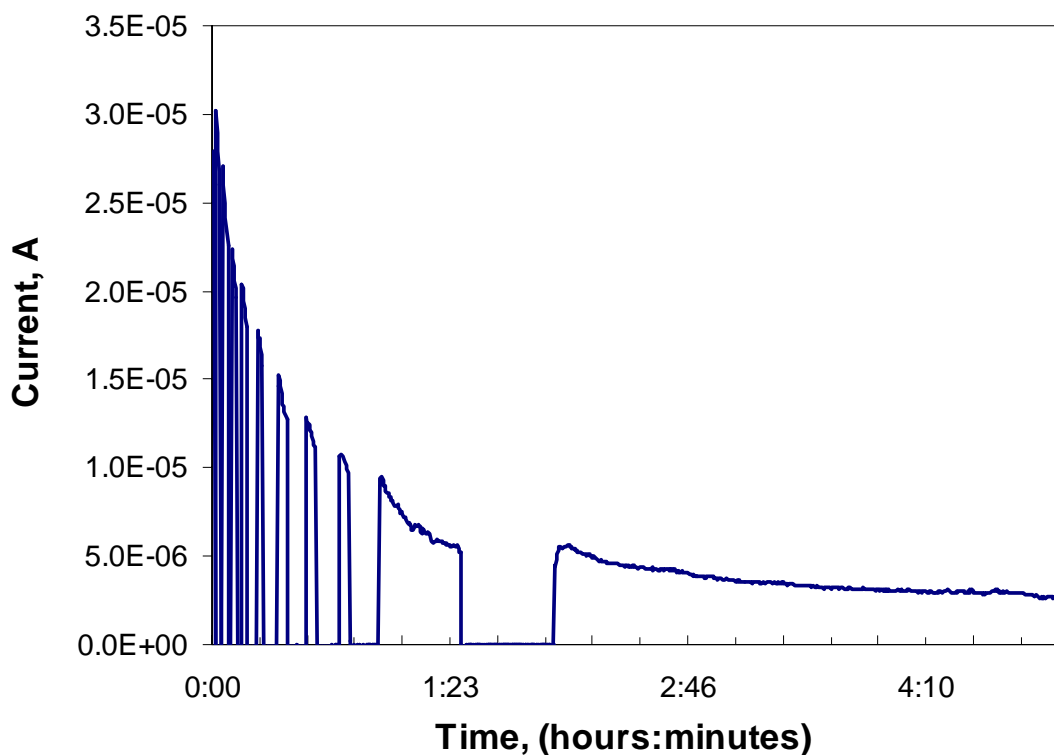


Figure 4-29 Current behavior over several hours with constant applied voltage above onset. Intermittent cuts in power that lasted up to 30 min. did not significantly change the current decay.

These results were highly surprising but also shed light on the possible charge behavior in the system. Ionization occurs in the early stages of the pump's operation. Thereafter, current decay could be mainly due to space charge effects rather than by discharge of impurities since the electric field does not exist with the pump power turned off.

In the later stages of the study, when a well-isolated test setup and degassed liquid were used in the experimental work (see Chapter 3 for more details), the time for the current to reach steady state was reduced by an order of magnitude as shown in Figure 4-29. This confirmed our theory that impurities indeed affect the space charge, but the

nature of this DC current application requires time for a steady state current value to be achieved.

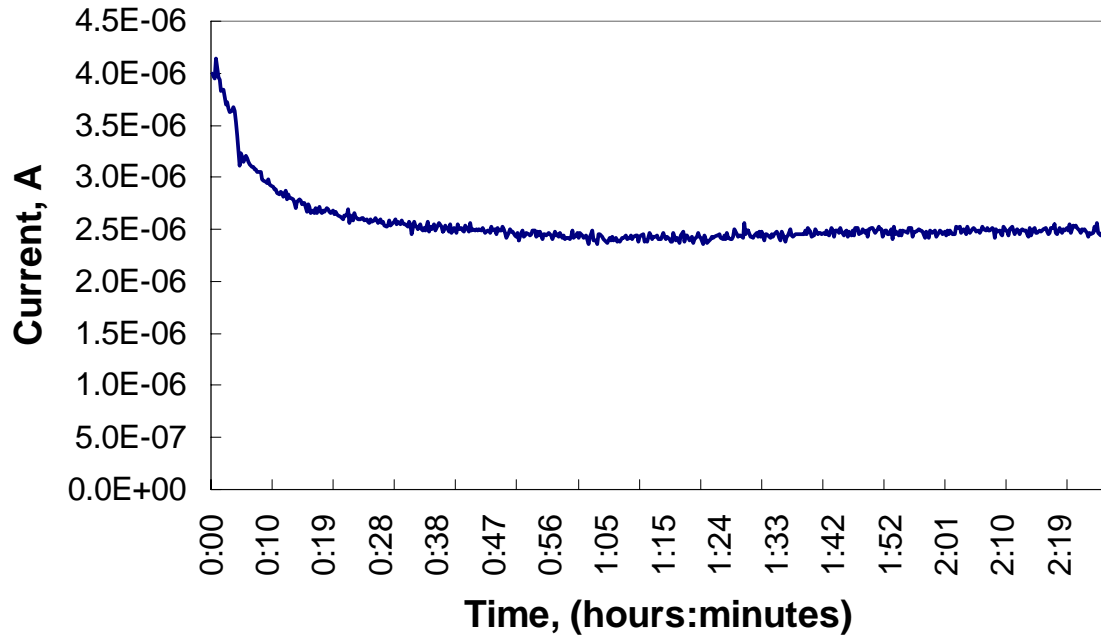


Figure 4-30 Current behavior for an isolated system and a degassed working liquid (input voltage above the onset level).

Another phenomenon that limits operation of the micropump is electric breakdown in the working liquid, as discussed above. The electric breakdown threshold is defined by the dielectric strength of the liquid, which 3M gives as 28 kV for HFE7100 at 25 °C for a 2.54 mm gap using an RMS A/C voltage. This is 11.02 MV/m in SI units. However, 3M does not specify what standard was used for the measurement, and the nominal value could only be taken as a guideline since the level of impurities, especially dissolved water, and the geometry of the electrodes can change the dielectric strength by an order of magnitude.

For the electrodes gaps of 10 to 50 μm in this study, the breakdown voltages were expected to be in the range of 110 to 550 V. As experimental results show, these values could be doubled for pure liquids and carefully designed electrodes. However, to be on the safe side lower threshold voltages were chosen, depending on the electrode spacing: 10 μm – 300 V, 20 μm – 400 V, and 50 μm – 600 V. Voltages above these levels produced irreversible damage to the electrodes, as shown in the section on electrode degradation.

4.8.4 Pump reliability and test repeatability

The previous discussion on electrode degradation and fluid breakdown set the foundation for understanding and evaluating the device's reliability and long term operability. It is important to know for how long a pump can function and to what extent its performance can be predicted under particular operational conditions. Like any other mechanical or electrical device, the ion-drag micropump is subject to various destructive forces impairing its ability to run indefinitely. Although EHD pumps do not have any mechanical components that wear out due to friction and vibration, it is subject to electrochemical processes that affect the electrodes and working fluid.

The literature on EHD pumping, reviewed in Chapter 2, suggested that despite the destructive nature of EHD, it does not stop pumps from operating. Unfortunately, almost no reported work discussed pump repeatability or longevity quantitatively, but only occasionally mentioned that some corrosive processes occur and that decay in performance is observed. Our results indicate that the destructive nature of EHD needs to be estimated and accounted for where reliability of small-scale pumps is concerned. For larger pumps (electrode sizes on the order of millimeters or greater), degradation is

slower due to the relatively smaller deposition on electrodes; however, it has also been found to be important for long-term operation, as was shown in pump service life tests by Bologna (Bologna, Kozhukhar et al. 1993).

The reliability of the ion-drag micropump was evaluated by performing several prolonged tests. As detailed above, in the first stage of pump and test loop design, performance faded significantly in less than 10 hours and was barely long enough to reach a steady state current (the pumping pressure stabilized in 2-3 hours) because of impurities. The performance of second generation pumps stabilized faster (20-30 min to reach steady state for both current and pressure), but the total operation time with a given volume of working liquid did not go much beyond 10 hours. It was difficult to distinguish the damaging effects of electrode vs. liquid degradation. Visual inspection of the electrodes after one test of 10 hours showed no significant degradation, suggesting liquid degradation. After a few more tests with fresh HFE7100, however, the electrode surfaces had visibly deteriorated.

Test repeatability was critical, as the absence of repeatability would have meant that the ion-drag micropumps under investigation could not provide any reliable correlations to use in design or in building a greater understanding of the EHD phenomenon itself. In short, the work would be useless. Fortunately, some degree of repeatability was achieved by combining careful electrode fabrication techniques with consistent and clean packaging and testing conditions, careful choice of materials, and purification and degassing of the working liquid.

In the first stage of the study, repeatability among samples of the same design was low: 50-100% variations in data were common. Same-sample repeatability was better,

but still had up to 50 % variation in current and pressure for a given input voltage. To address this worrisome situation, test procedures were changed to use a fresh working liquid for each test, which meant an extra 3-4 hours of charging and degassing work. In addition, improvements were made in material purity and cleaning procedures. At the end of the study, repeatability for samples of the same design was within 20-30%, and for the same sample it was down to 10%. In addition, for pump design optimization only the first test for each new sample was used in order to have data affected least by corrosive electrochemical processes.

4.9 Summary and conclusions

Experimental data collected during the course of the study were reduced, analyzed, and presented with the goal of identifying critical geometric design parameters and physical characteristics. The results are summarized as follows.

- 1) *Electrode gap.* Reducing the gap is the most effective way to increase both dynamic and static performance. Limitations to achieving smaller gaps are given by fabrication tolerances, as well as by increasing the relative size of non-uniformities in electrode shape, which could yield an earlier dielectric breakdown due to higher local electric field values.
- 2) *Electrode pair gap.* It can be concluded that there is an optimum value for the ratio of electrode pair spacing to electrode gap. Thus, these two distances should always be considered together.
- 3) *Fluid channel height.* Channel height has a dramatic effect on flow performance because internal pressure drops are large compared to other flow resistances for micropumps. Fluid channel height also plays a

significant role in the static pressure case, possibly due to internal recirculation patterns. Different optima exists for pressure head and flow rate. Finally, there is also an optimum height for maximum efficiency of the pump (but not for electric current).

- 4) *Electrode shape.* Flat beams are inferior to saw-tooth emitters, and narrower tooth angles yield even better performance. An undercut at the tip of the emitter improves performance even more.

CHAPTER 5 NUMERICAL WORK

5.1 Introduction

This chapter describes numerical modeling of the ion-drag pumping mechanism and its application to the design and optimization of the micropump under investigation. As has been emphasized throughout this entire report, EHD is a complex phenomenon involving interacting physical effects, among which are fluid dynamics, electrokinetics, and electrochemistry. Because of this complexity, the model used various assumptions to simplify the problem.

Since the main goal of numerical modeling was to gain a better understanding of the geometrical variables that affect the micropump's performance, interactions between the electric field and fluid were examined at the macro-scale, rather than at the molecular level. This was accomplished by developing a model for single-polarity charge injection with ohmic conduction. The convective current component was simulated for simplified geometric cases only.

As the basis for this model, Shooshtari's previous work with Fluent was used (Shooshtari 2004). Shooshtari provided assistance in building the model in Femlab, making use of predefined partial differential equations (PDEs) coded into the electrokinetics mode of the software. Though the same equations as in the Fluent model were used, the solver techniques, software ease of use, setting of boundary conditions, definition of geometries, and meshing were different. For example, a separate preprocessor is required for any Fluent simulation to generate the geometry and the mesh,

while Femlab has an integrated preprocessor. This lets the user easily change geometry and mesh it within the same software. Another useful feature of Femlab is the ease of setting periodic boundary conditions, which are unavoidable for any EHD pump design with more than one electrode pair. In addition, Femlab uses finite element modeling, and Fluent uses finite difference modeling. These differences made Femlab an attractive tool for the modeling work.

The numerical work is presented in several stages. First, a simplified analytical model of ion-injection is provided with the governing equations and boundary conditions. Next, the model is applied to the micropump under investigation and verified with the 50f100 design. Finally, the model is used to predict the effects of design variations for several geometric parameters.

5.2 Modeling of ion-injection pumping mechanism

5.2.1 Model assumptions and governing equations

Assumptions

Only by making simplifying assumptions it is possible to obtain a workable model. We made the following assumptions.

- 1) Only unipolar charge was considered. This means that only one kind of charge was used (positive or negative).
- 2) Diffusion of the charges was assumed to be zero. This assumption was based on the dominance of the charge migration process.
- 3) The fluid's conductivity, dielectric constant, and ion mobility remained constant. This assumption was one of the weakest, as some properties

are believed to depend on the electric field. However, no data are available on the dependence.

- 4) The emitter electrode was the only injection electrode, and its surface charge density was independent of electric field.
- 5) Only electrophoretic force drove the liquid (gravity and other electrical body forces were neglected).
- 6) The fluid flow was steady-state and incompressible.
- 7) In the three-dimensional models, side wall effects and entrance effects were ignored because of limited computational power.
- 8) Convective charge transport was ignored for most problems. This assumption is valid only for cases that have strong migrative charge fluxes, and it can lead to an estimated 5-10% error for certain operating conditions and electrode geometries. This hypothesis saved substantial computational resources (in many cases the problem was not solvable with the inclusion of convection current).

General Equations

The full set of equations has been presented in Chapter 2. Given here is a list of simplified equations under the given assumptions. For an incompressible fluid with Coulomb electric body force:

$$\nabla \cdot \mathbf{u} = 0 \tag{5-1}$$

$$\rho(\mathbf{u} \cdot \nabla)\mathbf{u} = -\nabla p - \mu \nabla^2 \mathbf{u} - \rho_e \nabla \phi \tag{5-2}$$

Next, the Poisson equation (also known as Gauss's Law) and conservation of charge describe the potential field and charge distribution within the control volume for steady-state conditions:

$$\varepsilon \nabla^2 \phi = -\rho_e \quad (5-3)$$

$$\nabla \cdot \mathbf{J} = 0 \quad (5-4)$$

where for the unipolar charge injection with the ohmic conduction, the current density is defined as

$$\mathbf{J} = \mu_e \rho_e \mathbf{E} + \sigma_e \mathbf{E} + \rho_e \mathbf{u} \quad (5-5)$$

Finally, the electric field is related to the electrical potential by:

$$\mathbf{E} = -\nabla \phi \quad (5-6)$$

Since HFE7100 is relatively conductive, the conduction component $\sigma_e \mathbf{E}$ cannot be neglected. The convective component can be neglected only if $\nabla(\mu_e \rho_e \mathbf{E})$ is of the same order of magnitude or larger than $\nabla(\rho_e \mathbf{u})$.

Equations (5-1)-(5-5) consist of five equations in five unknowns, i.e. \mathbf{u} , p , ρ_e , ϕ , and \mathbf{J} , so it is possible to obtain a solution. In fact, the current density \mathbf{J} can be eliminated by substituting (5-5) into (5-4). A closer look at the equations reveals that the equations are related as schematically shown in Figure 5-1. The convective current coupling between the flow fields and charge conservation is shown as a dashed arrow to represent its incomplete implementation in the model.

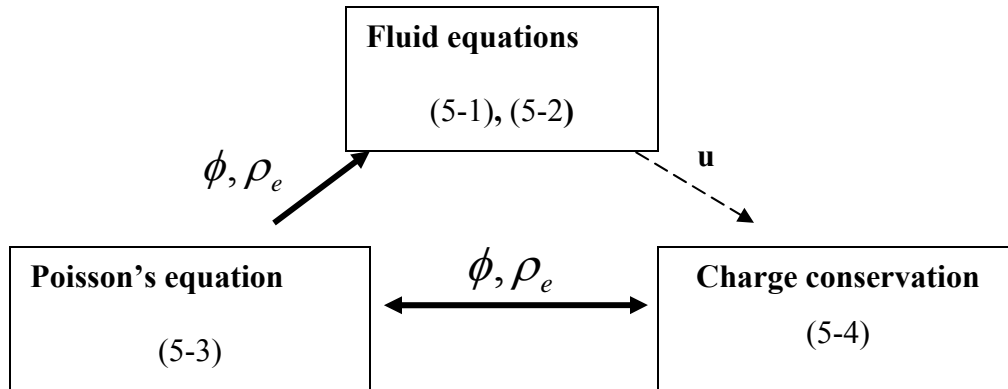


Figure 5-1 Coupling among equations, where arrows indicate the coupling direction. The dashed arrow indicates modeling of convective current that was implemented only for some geometries.

The continuity, momentum, Poisson, and charge conservation equations could be solved simultaneously. However, assuming negligible convective charge effects, the Poisson and charge conservation equations are independent of the fluid flow and can be numerically solved in advance.

Two more key output variables can be defined and solved using the independent variables. Integration of the current density \mathbf{J} over the cross-sectional area yields total current,

$$I = \int_A \mathbf{J} \cdot d\mathbf{A} \quad (5-7)$$

and integration of the velocity field over the flow cross-section yields the flow rate,

$$Q = \int_A \mathbf{u} \cdot d\mathbf{A} \quad (5-8)$$

5.2.2 Boundary conditions

Boundary conditions must be set for all three sets of physics. The first set comprises the conservation of mass and momentum equations, and the boundary conditions are trivial: no slip on the physical walls of the EHD device, and inlet and outlet set according to the desired flow conditions of the device. Similarly, setting up the electric potential problem is straightforward and is described in detail later. The challenge is to resolve the charge boundary conditions, as there is no complete understanding of charge generation at the emitting electrode. In his doctoral thesis, Shooshtari provided a good summary of available models for charge density boundary conditions (Shooshtari 2004). In the present study, a decision was made to use the autonomous charge injection model, which states that

$$\rho_e = \rho_{e,emitter} \text{ on the emitter electrode} \quad (5-9)$$

Unfortunately, $\rho_{e,emitter}$ is not explicitly available, and either some analytical expression should be used, as proposed by Castellanos (Castellanos and Gonzalez 1998), or the value should be based on the experimentally measured current I_{exp} . The latter was adopted for this work, matching the experimental electric current with the current calculated by (5-4).

$$\rho_e = \rho_{e,emitter} \text{ on emitter so that } I_{exp} = \int_A \mathbf{J} \cdot d\mathbf{A} \quad (5-10)$$

The charge condition on the collector electrode is unknown as well, but for the diffusion-free problem it needs to be specified to complete the model. It is safe to assume Neumann's boundary.

$$\mathbf{n} \cdot \nabla \rho_e = 0 \quad \text{on collector}$$

(5-11)

The same boundary conditions are set for the other surfaces, with the exception of the emitter (Shooshtari 2004).

5.3 Model application to the ion-injection pump using numerical solver

The ion-drag pumping model presented in Section 5.2 can be analytically solved only for simplified geometries, such as parallel and infinitely large flat electrodes. In addition, the problem of the emitter boundary condition has to be resolved if no experimental data are available. For more complex electrode and pumping chamber geometries, numerical techniques are the only possible way to solve the coupled equations (5-1) through (5-4).

Various numerical models and software products have been used in the past. However, most of them were specialized toward one field of physics or relied on custom-written code to couple other phenomena. In this work, the numerical tools were only supposed to give insight into the experimental data. For this purpose, FEMLAB (Comsol, Inc., Burlington, MA) was chosen. For the ion-drag micropump model, it provided seamless coupling of electric and flow fields with a minimal amount of custom coding. While limited in processing power by the hardware, FEMLAB still enabled processing of some 3-D models with asymmetric geometries.

5.3.1 Problem setup

Two approaches were used. One used the cross-sectional symmetry of the planar strip electrode configuration to set up the problem in 2-D space, and the other used a 3-D computational domain for more complex electrode geometries, as illustrated in Figure 5-2. In both cases, symmetry was exploited to save computational power.

Only one of the electrode pairs was modeled. Since electrodes are connected in parallel, the total electric current was obtained by multiplying the current by the total number of stages. Similarly, since channel stages are in series, cell pressures have to be added to obtain total pressure. The physical properties of HFE7100 used in the numerical model are listed in Table 5-1.

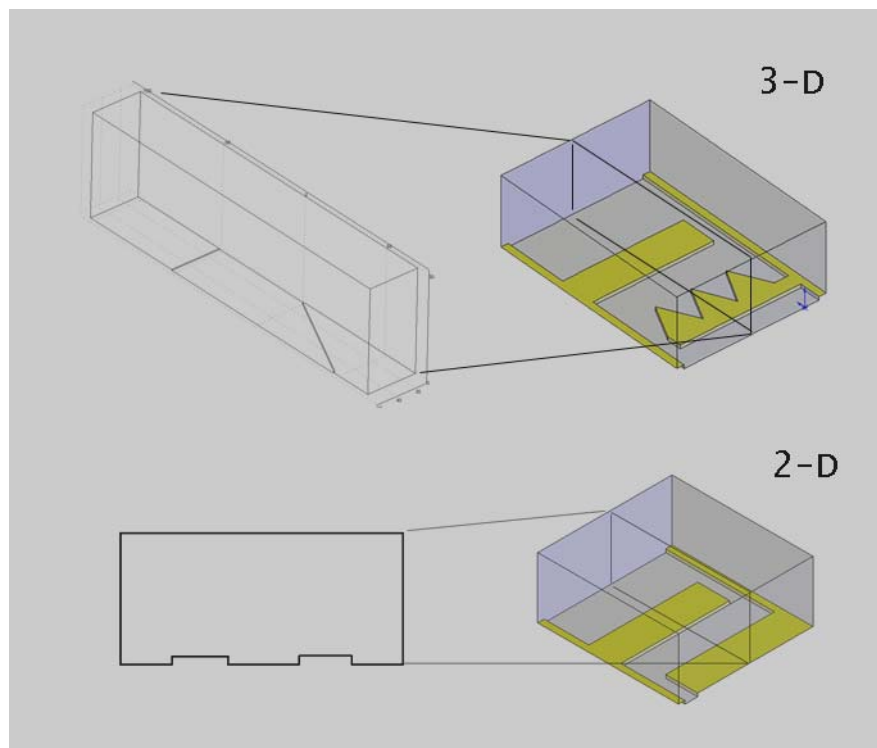


Figure 5-2 The computational domain was 2-D for strip electrodes and 3-D for more complex geometries like saw-tooth and overhang.

Table 5-1 HFE7100 physical properties reported by 3M®.

Physical property	Value for HFE7100
Density (kg/m ³)	1481.6
Dynamic viscosity (kg/m-s)	5.46e-4
Dielectric constant	7.39
Ion mobility (m ² /V-s)	1.56e-8*
Liquid bulk conductivity (S/m)*	3.08e-8**·***

* Ion mobility was calculated using Walden's rule.

** Bulk conductivity and ion mobility were later adjusted to match the experimental results.

***At 1 kHz A/C current and 25 °C.

First, the computational domain geometry was set up. For the 2-D case it was drawn with FEMLAB drawing tools, and for the 3-D case it was imported from Solid Works, since FEMLAB tools were not sufficient to draw the complex electrode tip curvatures with the desired accuracy. Next, the three sets of physics modes were assigned and set up for the drawn geometry. Each mode is briefly summarized in the following sections.

Electrostatics

The FEMLAB electrostatics mode models the electrostatics of dielectric liquids, which are governed by Equation (5-4). For the current problem, an isotropic dielectric constant was used, and the charge density was set to the variable Rho (a name chosen to represent charge density within the model, which was later solved for in the electrokinetics mode). The electrostatics mode solved for one variable, the electric potential V. The initial value for V was set to zero. Boundary conditions are given in Table 5-2. Through the input of potential boundary conditions and media properties, the

electrostatic mode resulted in the potential field distribution, which helped to resolve the electric field within the computation domain using Equation (5-6).

Table 5-2 Boundary conditions for the electrostatics mode.

Collector	Grounded (zero potential)
Emitter	Specified fixed voltage V_{exp} as used in experimental setup
Other walls	Insulating ($\frac{\partial V}{\partial n} = \mathbf{n} \cdot \nabla V = 0$)

Electrokinetics

The FEMLAB chemical module has a convenient, built-in electrokinetic mode that models the Nernst-Planck equation:

$$\frac{\partial c_i}{\partial t} + \nabla \cdot (-D_i \cdot \nabla c_i - z_i u_i F c_i \nabla \varphi) + c_i \mathbf{u} - R_i = 0 \quad (5-12)$$

where c_i is concentration, D_i the diffusion coefficient, u_i the mobility, and R_i the reaction coefficient of species i . This equation is similar to the charge conservation equation (5-4) under the transient condition, where concentration c_i would be substituted by charge density ρ (named Rho in the FEMLAB setup). The diffusion coefficient and reaction rates were set to zero. Only migration charge flux was investigated, with several attempts to introduce the convective flux $c\mathbf{u}$.

Table 5-3 Boundary conditions for the electrokinetic mode.

Collector	Neumann boundary condition* setup by specifying the charge flux to be equal to $\text{mobility} \cdot \text{Rho} \cdot \nabla \cdot \text{E}$
Emitter	Specified fixed voltage (designated by Rho_em in the FEMLAB model) determined by matching numerical and experimental currents
Other walls	Insulating

*Note: A trick had to be performed in order to set Neumann b.c. ($\frac{d\rho}{dn} = 0$) in FEMLAB as no option for that was given. Instead, a flux condition was chosen and the reaction rate chosen so that Neumann b.c.s were satisfied on the collector.

The Nernst-Planck equation allowed us to include the conduction current using a method similar to the one we used for setting up the Neumann boundary condition on the collector surface. A conductive charge flux was defined in the reaction rate $R = -\sigma \cdot \text{Rho} / (\text{de} \cdot \text{epsilon0_es})$, where σ is the liquid conductivity, de the dielectric constant, and epsilon0_es the permittivity of vacuum.

Once the electrostatics equation was solved, the potential field was fed into the electrokinetic pump model and solved again simultaneously with the electrostatics. A nonlinear solver was used to obtain accurate values of the charge density and potential field.

Fluid dynamics

As shown in Figure 5-1, electric potential and charge density fields were combined to produce the electric body force, which was fed into the flow model based on the Navier-Stokes equations. Static and dynamic flow conditions were both considered. The former case sets a zero flow rate through the micropump ports. The dynamic flow condition was achieved by allowing flow to pass through the micropump ports. External flow resistance could be set to be a function of flow rate to obtain a specific operating

point. By varying this point, the pump characteristic curve could be obtained (for more discussion on this topic see Chapter 4). The other channel walls were given non-slip conditions. Doubts have arisen in the literature on whether the no-slip condition is valid for micro-geometries (Lee, Wong et al. 2002; Shou-Shing Hsieh 2004), but the channel dimensions investigated in this work were considered to be large enough for continuum physics and macro-scale correlations for pressure and flow rate to be valid.

Additional setup steps

Since only one pair of electrodes was modeled, it was important to model inlet and outlet boundary conditions correctly so that the entrance effects for fluid flow, potential, and charge density distributions were accounted for. For laminar flow, the channel entrance length (the distance from the fluid inlet to the point in the channel where the velocity profile is fully developed) is defined as (Incropera and DeWitt 2002):

$$L_e = D_H * Re * 0.06 \tag{5-13}$$

Where D_H is hydraulic diameter of the channel and Re is Reynolds number. For our pump geometries (width = 1.15 cm, channel height up to 1 mm) and flow rates, the entrance length is on the order of 1 mm. Considering that the total length of the pump is 20 mm, entrance effects were considered negligible and not modeled. Similarly, wall effects on the sides of the electrodes were neglected as their relative sizes were small compared to the channel width. Analytically calculated entrance lengths and Reynolds numbers are presented in Figure 5-3.

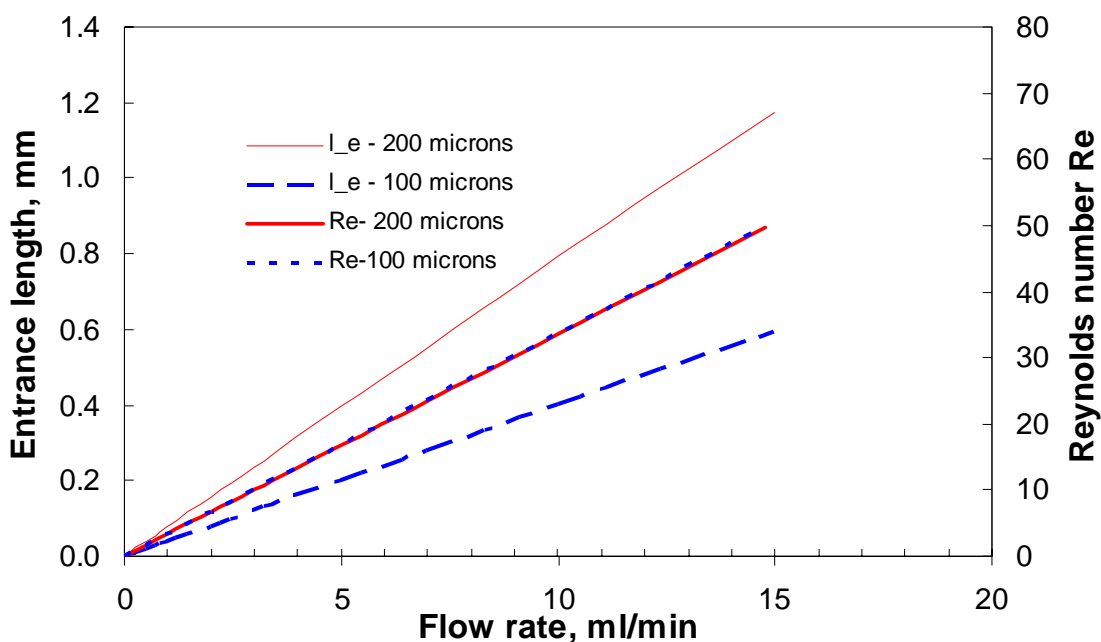


Figure 5-3 Entrance length l_e and Reynolds number Re vs. typical flow rates for two channel heights and a 1.15 cm micropump width and a rectangular channel. Total length of the pump was 20 mm.

Since fully developed flow was assumed, periodic boundary conditions were used to match inlet and outlet velocity profiles. Similarly, periodic boundary conditions were used for the potential fields and charge density distribution to account for the effect of neighboring pump stages. The tricky part was evaluation of the pressure head, as matching the flow rates at the inlet and outlet did not specify anything about the pressure. The solution to this problem required setting up a periodic pressure difference which could be changed to represent different external circuit flow resistances, or which could be defined as a function of flow rate to obtain a specific operational point.

Numerical solvers are not perfect. In general they rely on a good computational mesh, cleverly guessed initial conditions, and some artificial damping parameters. Since the micropump model neglected diffusion, the solver struggled to obtain a stable, charge-density converged result unless some “help” was introduced in the form of an artificial

diffusion parameter. This parameter was varied to find the smallest value that provided a convergent result. The final selection was a Petrov-Galerkin streamline artificial diffusion with a value of 0.2.

5.3.2 Model verification

The model was verified using the 50f100-220 pump design (50 μm electrode spacing, 200 μm electrode pair spacing, 220 μm channel height, rectangular-shaped electrodes). Differences between results from the numerical model and the experimental data were within the uncertainty of the experimental measurements. The procedural sequence of the modeling steps is presented below.

First, the 50f100-220 model was drawn into the FEMLAB software. A 2-D computational domain was used as shown in Figure 5-9. The mesh was focused around the electrode edges, where the largest field gradients were located (Figure 5-4).

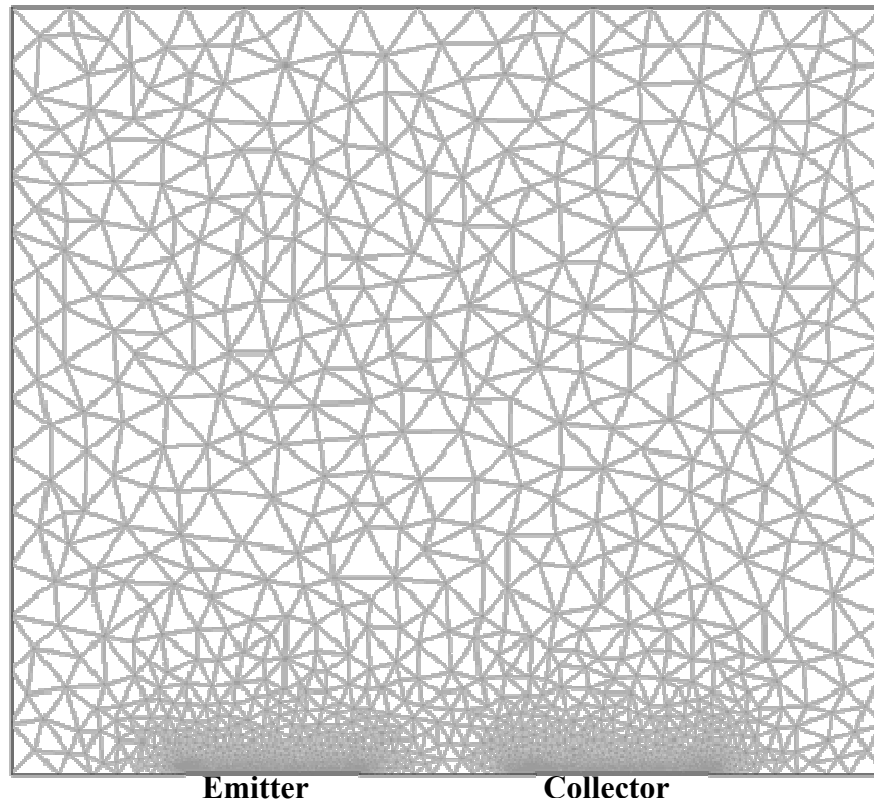


Figure 5-4 Computational mesh for the 50f100-220 pump design.

Once the geometry and the mesh were set up, material properties and physical constants in Table 5-4 were entered. Note that conductivity of the HFE7100 varied from the value provided by 3M[®] by an order of magnitude. The value provided by 3M[®] was measured with a 1 kHz A/C power source, while the current study exploited DC power. According to observations by 3M[®] and a literature review for various refrigerants (American Society of Heating Refrigerating and Air-Conditioning Engineers. 2003), DC conductivity is anywhere from 1 to 3 orders of magnitude lower than that of AC conductivity. In addition, varying conductivity does not affect the numerical model significantly: one order of magnitude change resulted in only a 5% change in current.

Table 5-4 FEMLAB input variables and constants for the 50f100-220 pump model.

Name	Expression/value	Description
Rho_em	Varied from 0.01 to 0.16	Emitter charge density
Vexp	100-600	Input voltage
Pressure	0 to static pressure for a given design	Total differential pressure for the device (used to obtain pump characteristic curves)
N_stage	78	Number of pump stages (electrode pairs)
dp	Pressure/N_stage	Differential pressure for one stage
De	7.39	Dielectric constant
Mobility	2e-7	Mobility of the HFE7100. This value was used to match the experimental I-V curve.
Sigma	1e-9	HFE7100 bulk conductivity. This value was used to match the experimental I-V curve.
W_channel	0.0115	Width of the channel. Used in conversion from 2-D to 3-D model.

Next, the boundary conditions were set up as described in Section 5.3.1. Since the model was to be compared with the experimental data, differential pressure was set up to reflect the pressure dependence on the flow rate for valve setting #1 (test loop flow resistance calibration according to the static valve settings were offered in Figure 3-19) and governed by the function $DP = (0.4388*Q^2+6.0979*Q)/n_stage$ obtained in Chapter 3. The total pressure was divided by the number of the stages, as only one electrode pair was modeled.

The electrostatics equation was solved to obtain a potential field distribution as seen in Figure 5-5. Next, the electrokinetics mode was coupled with the electrostatics mode to acquire the charge distribution. Because of the coupling with the charge density, the electric field experienced some changes as well. In addition, a Coulombic electric body force was calculated by taking the product of the electric field and charge density. Results are shown in Figure 5-6, where white arrows display the electric force and the color gradient shows the charge density distribution.

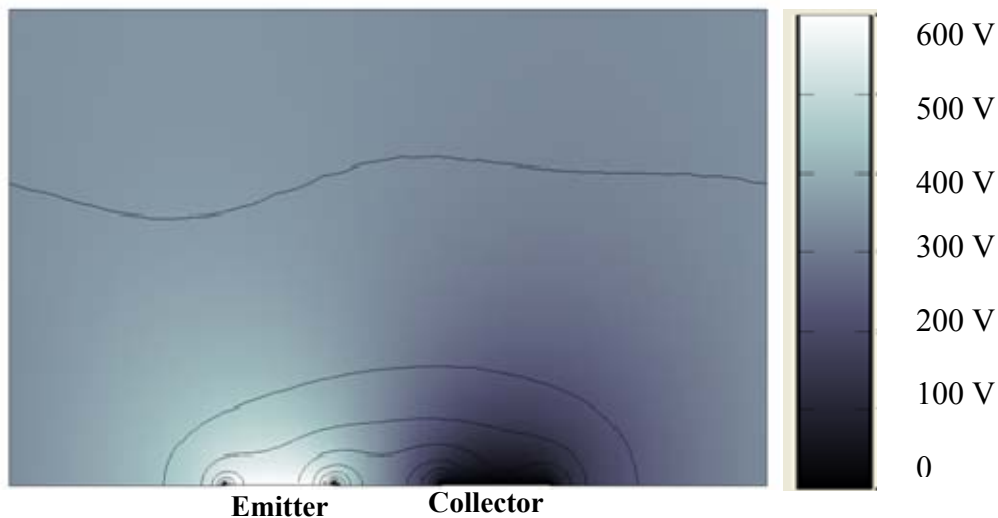


Figure 5-5 Potential field distribution and electric field contour lines for the electrostatics problem with an emitter voltage of 600 V and a grounded collector. Pump design: 50f200-220.

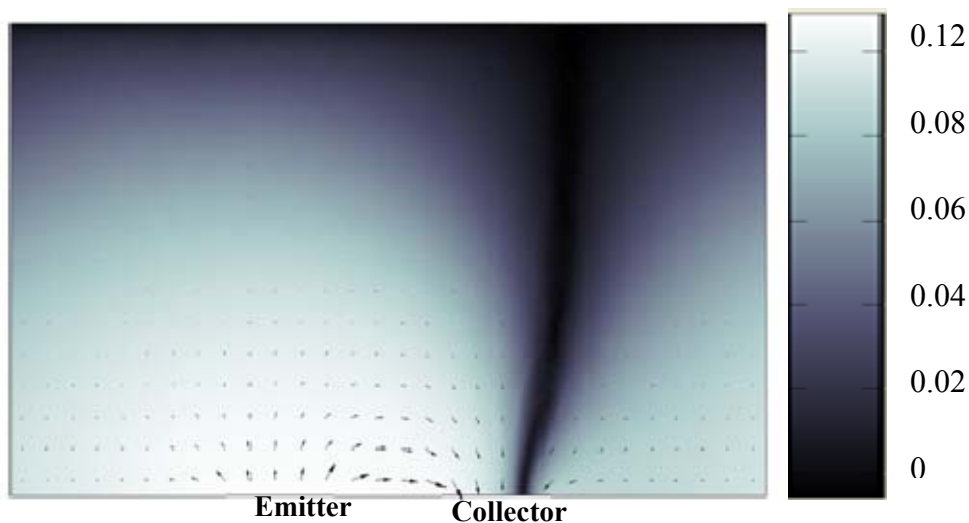


Figure 5-6 Charge density distribution and electric body force vectors for 50f200-220. Input voltage is 600 V.

Note that the electric body force is strongest between the emitter and the collector, but that there are also force vectors pointing back to the previous stage. This effect is indicative of unavoidable multi-stage electrode pair interactions, which results in a weakened net body force.

At this point it was important to impose the emitter charge density boundary condition such that the current in the pump (equal to the integral of the current density on the surface of the emitter electrode) matched the experimental current. This was done by trial and error. Initially, only the charge density emitter boundary condition was varied. However, it soon became clear that there was an unavoidable mismatch with the fluid conductivity and mobility. Once the conductivity was adjusted to $1\text{e-}9 \text{ } \Omega^{-1}\text{m}^{-1}$, as discussed at the beginning of this section, I-V (current-voltage) experimental and numerical curves were in good agreement for the ohmic part of the curves. Next, the mobility of the HFE7100 was adjusted to match the injection-regime part of the I-V curve (Figure 5-7). This was achieved with $\mu_e = 2\text{e-}7 \text{ V}^2/\text{m-s}$. Such a change can be justified by the fact that Walden's rule for relating a refrigerant's viscosity to its ion mobility has

been reported to be valid only to about one order of magnitude (Schmidt 1990), which is within the changes made for the numerical model. Flow rate and static pressure heads were next compared to ensure the model's validity.

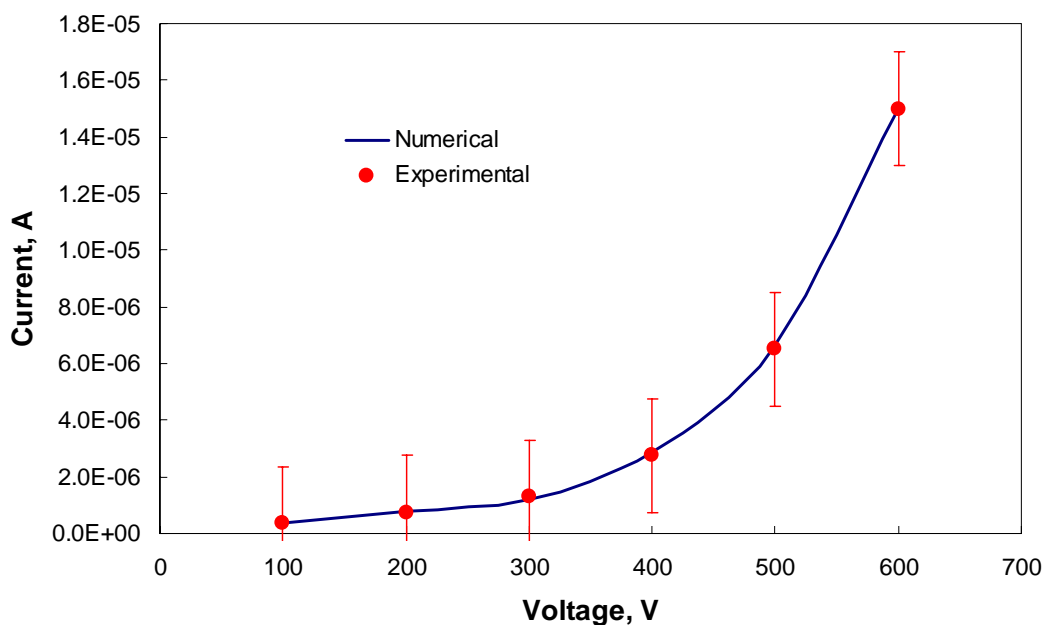


Figure 5-7 Numerical current matched to the experimental data for the 50f100-220 design.

Results agreed very well. Flow rate and the static pressure head matched the numeric model within measurement uncertainty as shown in Figure 5-8 and Figure 5-9. The external test loop flow resistance with valve setting #1 was used to obtain the flow rate. Flow rate measurement uncertainty was calculated by adding the instrumentation uncertainty of 0.2 ml/min to an estimated 15% variation obtained in experiments with different pumps of identical design.

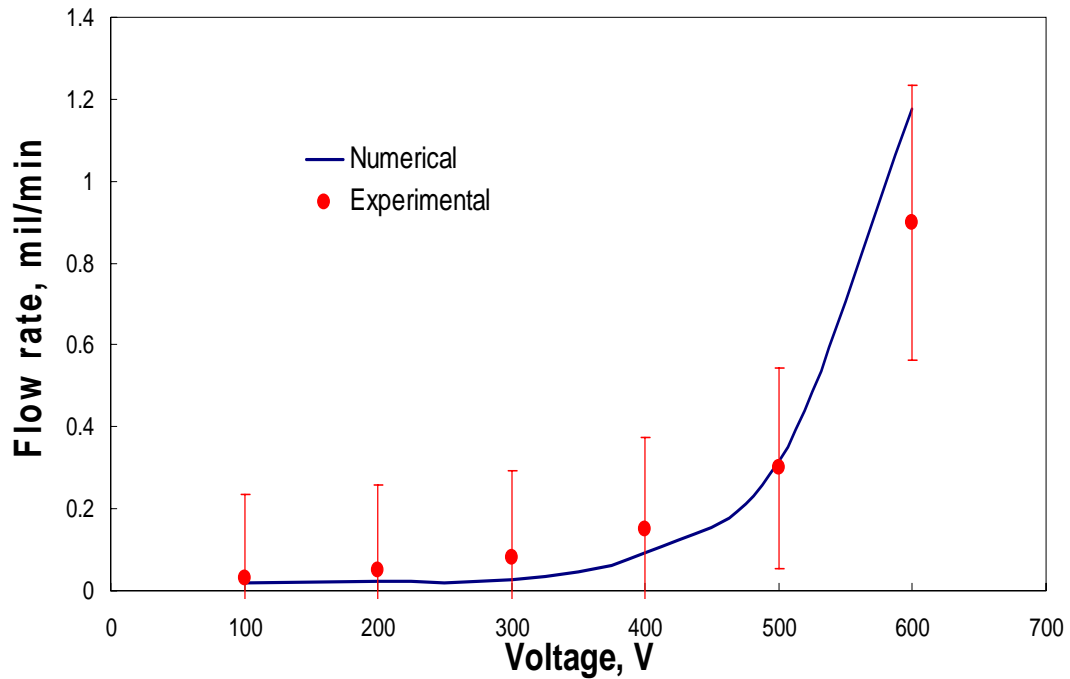


Figure 5-8 Numerical and experimental flow rates for 50f100-220 for an external loop pressure drop using valve setting #1.

Static pressure was obtained by first running the model with a low differential pressure to obtain a positive (pumped) flow rate. Then the pressure was increased to resist the electric body force-generated flow until no net flow was observed. This was static pressure, sometimes called backflow pressure, as any value above it would force flow against the pumped direction. Uncertainty in the pressure readings was established by adding the instrumentation error of 2 Pa to a 15% uncertainty from runs with different samples of identical design.

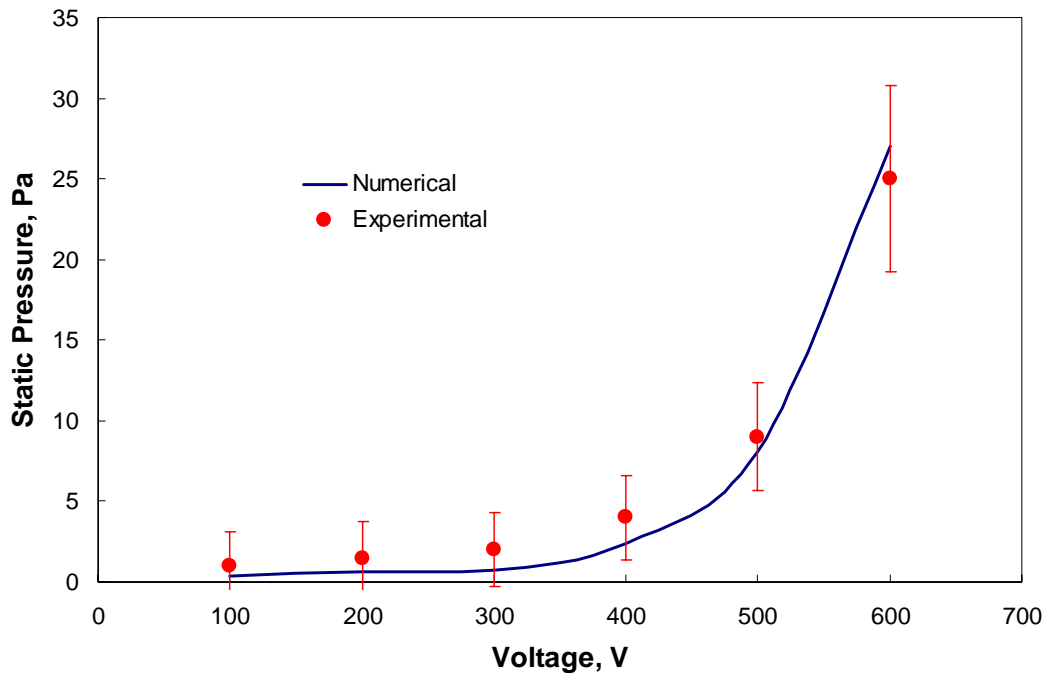


Figure 5-9 Static pressure vs. input voltage for numerical and experimental data for 50f100 – 220.

The excellent match in both flow rate and static pressure for valve setting #1 suggests that the model is valid. Further verification was obtained when pump characteristic curves were compared, as shown in Figure 5-10. In order to avoid crowded graphs, only 400, 500, and 600 V curves are plotted. The numerical results match the experimental data very well.

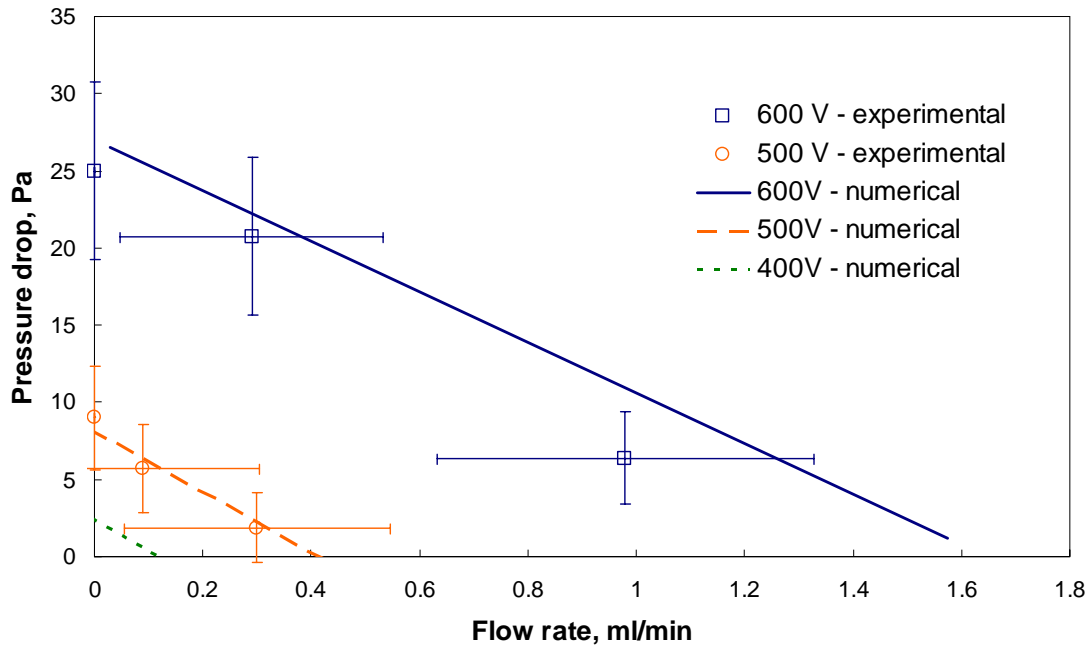


Figure 5-10 Numerical characteristic curves for several input voltages compared with experimental data for the 50f100 – 220 design.

5.3.3 Conclusion on numerical model verification

Model verification used the experimental I-V curve as input to obtain the emitter charge density boundary condition. In order to achieve this, the emitter boundary condition must be expressed in terms of some known variables and properties. Figure 5-11 displays the relationship between charge density and voltage for three channel heights that were generated numerically while matching the relevant experimental I-V curves. Two distinct regions are identified: the ohmic region (< 300 V), where ρ is independent of voltage, and the injection region, where ρ and voltage are related by an exponential function. Some prior knowledge of the onset point (regime changeover point) is needed to connect the two regions.

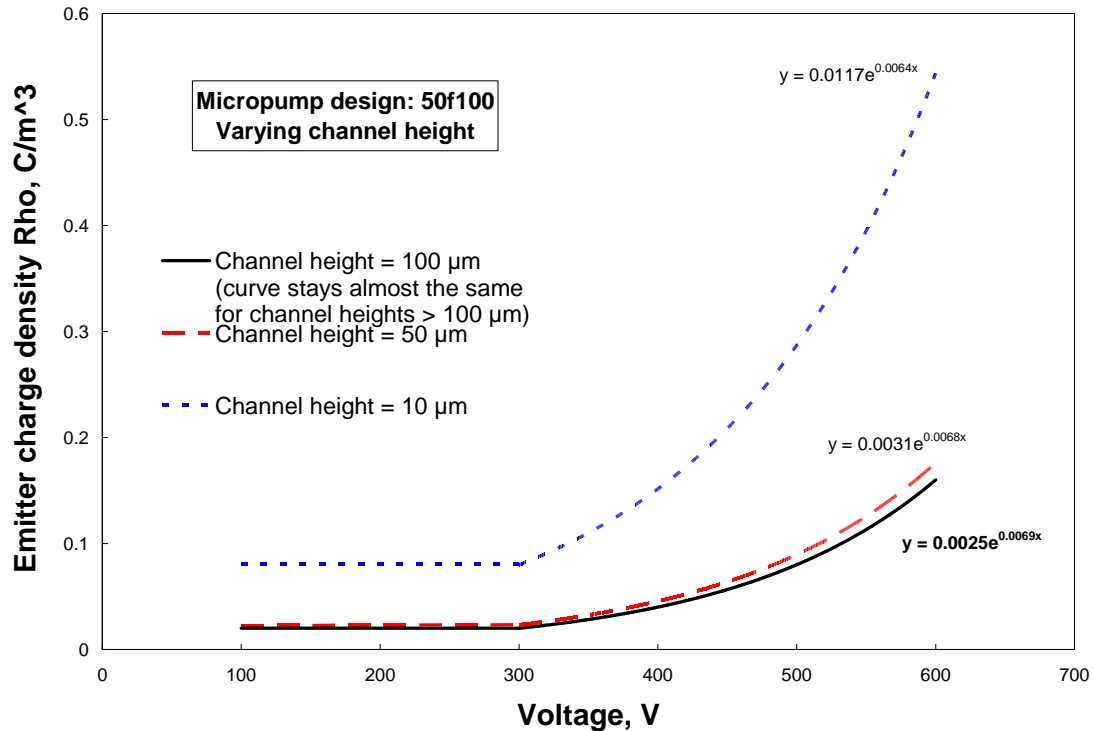


Figure 5-11 Emitter charge density dependence on the input voltage for the 50f100-pump design.

For small channel heights ($< 100 \mu\text{m}$), the emitter charge boundary condition also depends on the channel height. For flow passage depths greater than that, charge density at the emitter is constant for a given input voltage. This is consistent with the results reported in Chapter 4, which investigate channel heights above $100 \mu\text{m}$ and showed that the I-V curves were independent of shape and channel height. Therefore, this model can only be used for analysis of similar electrode designs in terms of electrode gaps. A different experimental I-V curve would be needed for resolving the charge boundary condition on the emitter if pump designs were dramatically changed.

An additional assumption of constant current was introduced in further numerical modeling. This means that independent of the channel height or electrode shape, for the same electrode spacing the current was kept constant in terms of input voltage by

adjusting the model charge density at the emitter. Another approach would have been to keep the emitter charge density constant under a given input voltage; however, this contradicts the observed trends in the experimental data reported in Chapter 4. Figure 5-12 helps to demonstrate the relationship between current and charge density at the emitter. For the constant current assumption, the emitter charge boundary condition has to be varied as shown in Figure 5-12. Similarly, in order to maintain constant Rho (the flat portion of the dashed lines), current would decrease for channel heights below 100 μm .

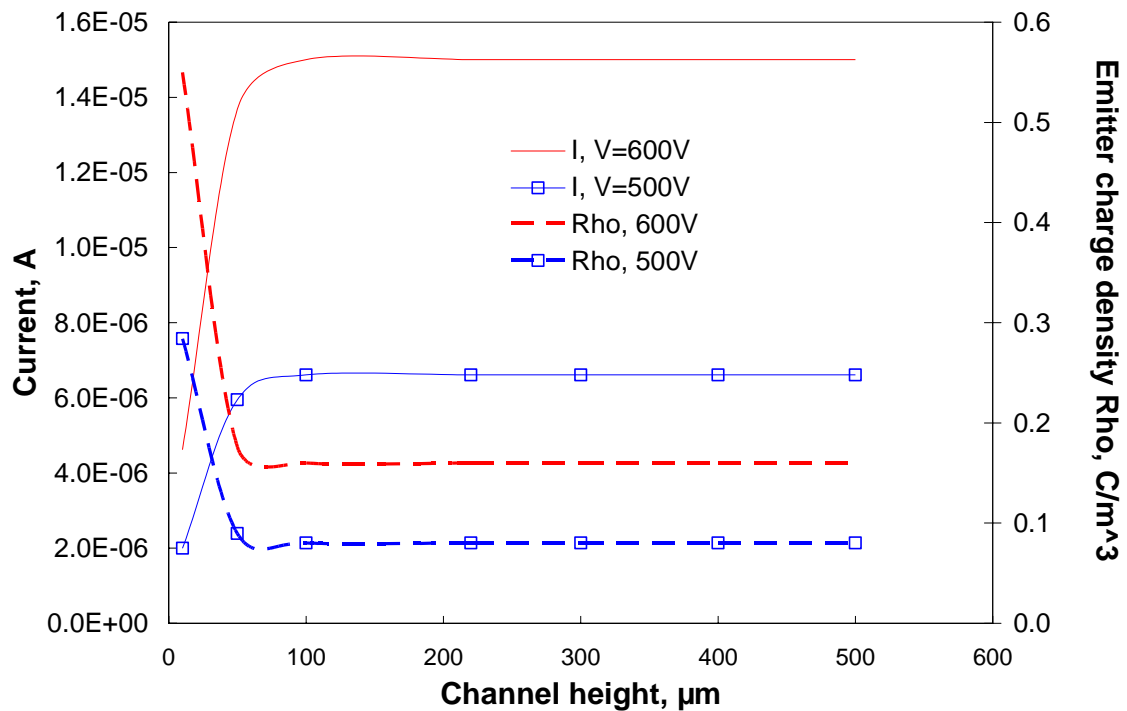
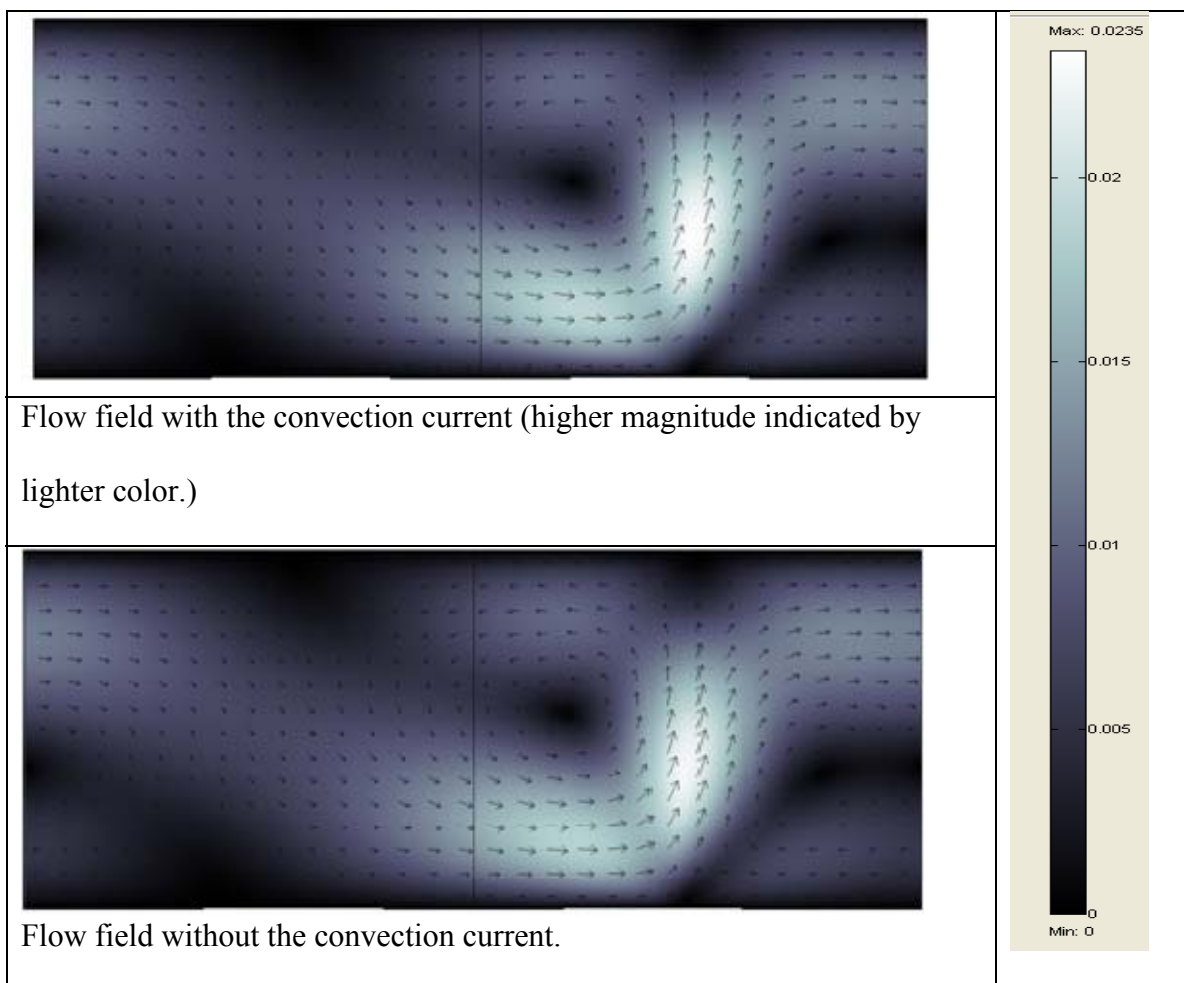


Figure 5-12 Current and emitter charge density dependence on channel height. The data was generated using numerical ion-drag pump model and keeping one of the two assumptions: constant current or constant emitter charge density for varying channel height.

5.3.4 Convection current modeling

As discussed earlier, including convection current into the current conservation law made convergence difficult due to the third coupling path between the fluid and electrical equations. Furthermore, convection current was argued to be negligible under certain conditions. To verify that assumption, a simulation of the 50f100-100 micropump design was performed that included convection. Convergence was achieved by sequentially solving the electric and fluid equations separately. The results are presented in Table 5-5.

Table 5-5 Comparison of the fluid fields with and without convection current included. 50f100-100 micropump design with test loop setting #1.



The results indicate that only a 3% increase in flow rate (from a velocity of 0.0228 m/s to 0.0235 m/s) was obtained by introducing the convective flow and current coupling. This justified the exclusion of the convection current component from the model and thus saved a significant amount of time and computational power.

5.4 Numerical results

The rest of this chapter will present numerical modeling results. First, the ion-drag model again uses the 50f100 micropump design to determine the effects of channel height and electrode stage spacing on the pump's performance. Following that, a discussion on the flow field and charge density distribution within the micropump is offered. Finally, the focus is shifted to modeling the electric field. 2-D investigation of the designs used in the experimental stage is presented using the notion of maximum electric field. These results are used for geometrical optimization.

5.4.1 Channel height effect on pump's performance

The effect of channel height on flow rate is controlled by two competing parameters: flow resistance and electric force density. Experimental data in Chapter 4 indicated that there is an optimum flow rate for a given pumping system. For test valve setting #1 (refer to Chapter 3 for specific flow rate resistance-pressure relation data), the maximum flow rate was for channel heights in the range of 278 μm to 350 μm . This value coincides with the numerical model predictions shown in Figure 5-13. Note that the optimum channel height is independent of the input voltage.

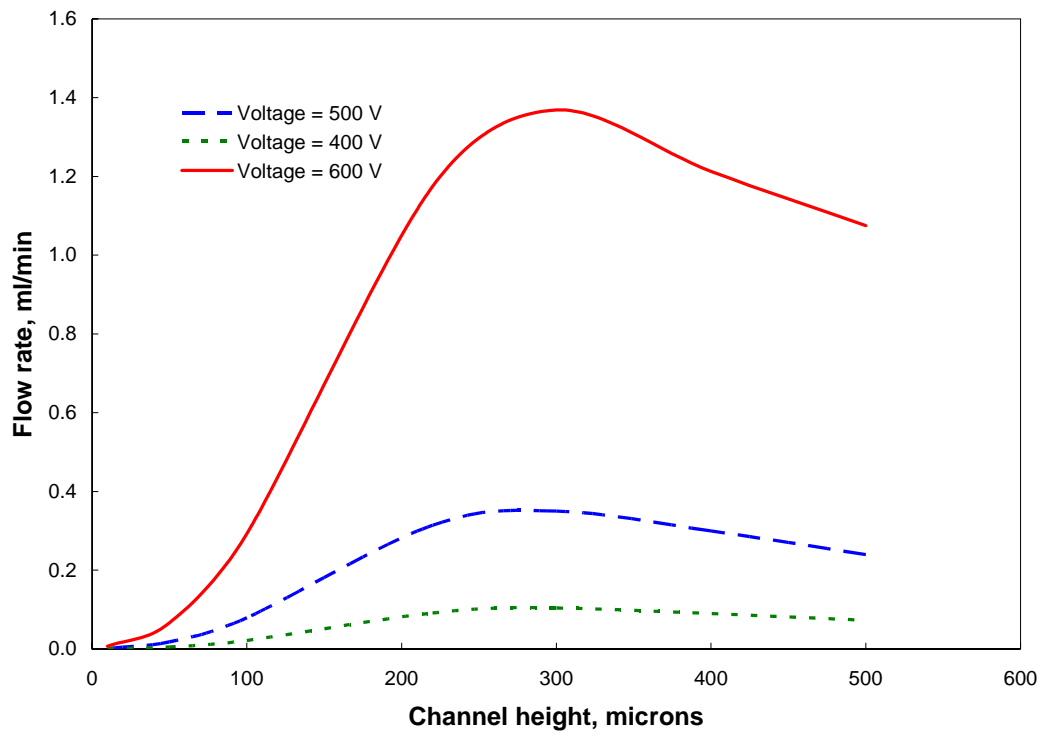


Figure 5-13 Numerically modeled flow rate vs. channel height for different input voltages with the external test loop resistance governed by valve setting #1.

For the static case, an optimum channel height does not exist. With a decrease of channel height, static pressure increases due to the larger electric body force density.

This effect has been well captured by the numerical model and is shown in Figure 5-14.

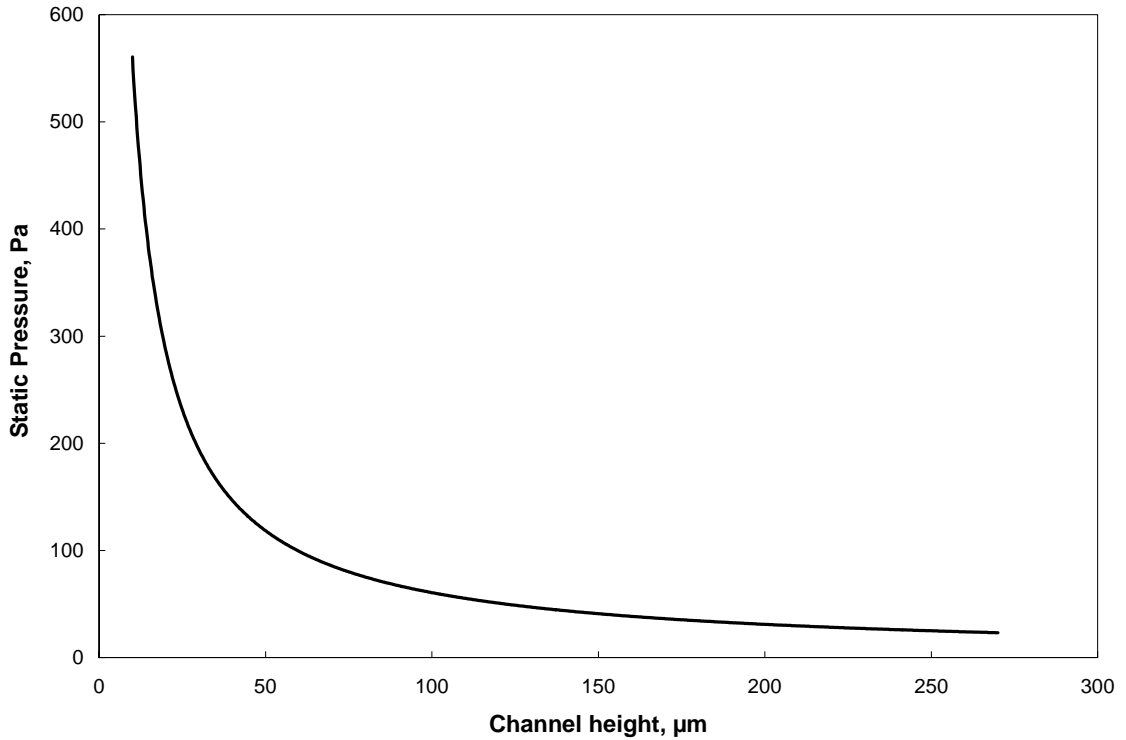


Figure 5-14 Static pressure vs. channel height for the 50f100 pump design operating at 600 V.

A summary of the channel height's effect on pump performance can be obtained from Figure 5-15, where pump characteristic curves are given for three different channel heights. The plot shows a well-known pump trade-off, that with increasing channel height, flow rate gains are offset by lower backflow pressures.

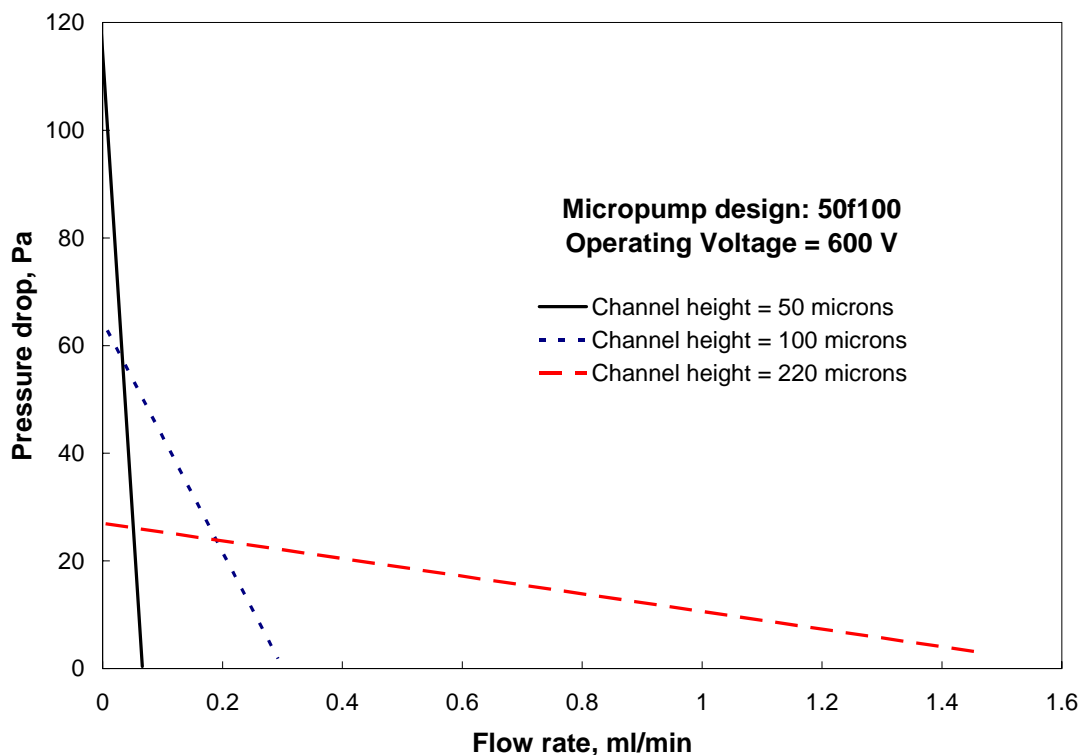


Figure 5-15 Pump characteristic curves for various channel heights.

5.4.2 Inter-electrode distance effect on pump performance

An attempt was made to use the numerical model to predict the effect of varying the distance between electrode stages. In the experimental work shown in Chapter 4, interactions between neighboring electrode stages reduced pump performance even though there was no appreciable difference in the I-V curves. These conclusions were derived from designs 50f100 with 50f200, 50s100 with 50s200, and 20s40 with 20s80. All three pairs of pump prototypes had the same *relative* distances between electrode stages compared to electrode gaps. A number X is defined to represent the ratio of these distances.

In the numerical model, if a constant total current for a fixed length device was assumed, the flow rate increased vs. X, as shown in Figure 5-16 (dashed curve). This

contradicted common sense, since this meant that for a fixed-length pump, fewer electrode pairs lead to greater flow. (Imagine an “ideal” case of having only 1 electrode pair!) Next, a constant current per electrode pair was maintained. This assumption is a reasonable one since it states that with varying inter-electrode stage spacing, resistance between the emitter and collector will not change significantly. The numerical result showed that with increasing electrode stage spacing, the flow rate peaks at a value of approximately 13. Such a result is important because it indicates that the inter-electrode stage spacing used in the experimental tests (at most 4:1) must be increased substantially for optimum pump performance.

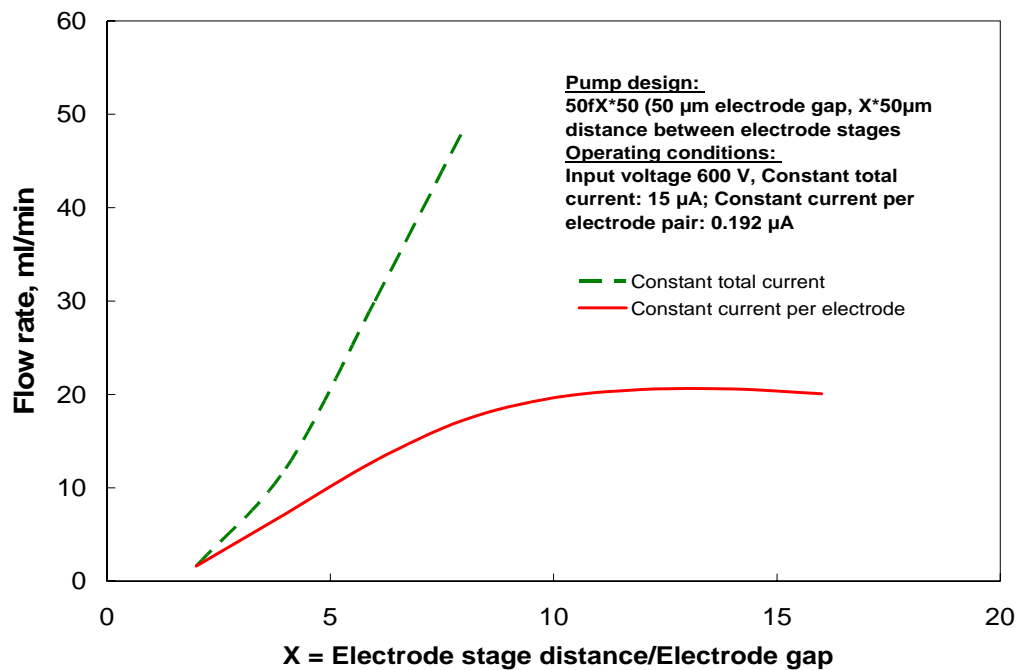


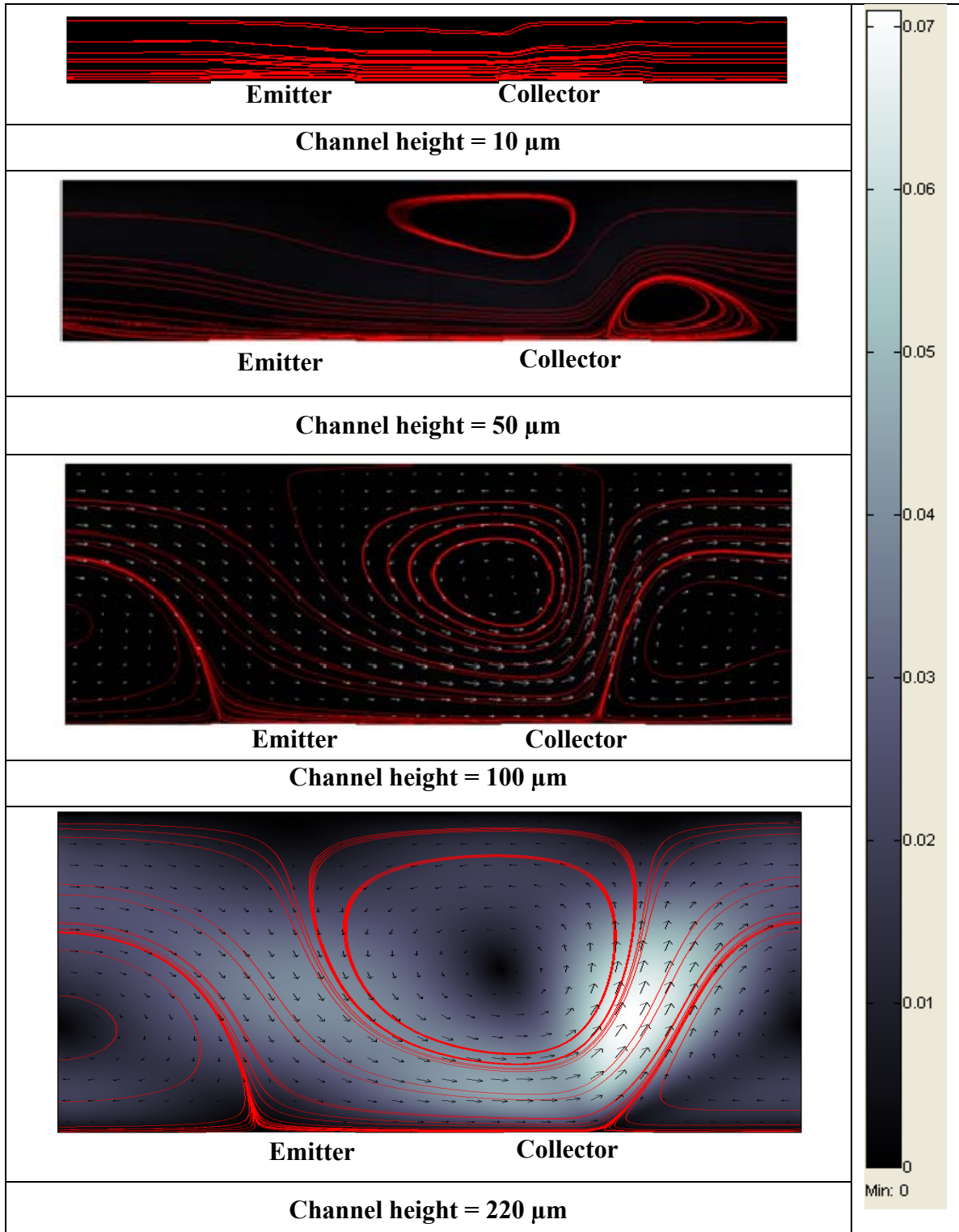
Figure 5-16 Effect of electrode stage spacing on the flow rate.

5.4.3 Discussion of the flow patterns

The numerical model allowed us to acquire new insight into the flow field and charge distribution. Table 5-6 presents velocities in the 50f100 pump model with four

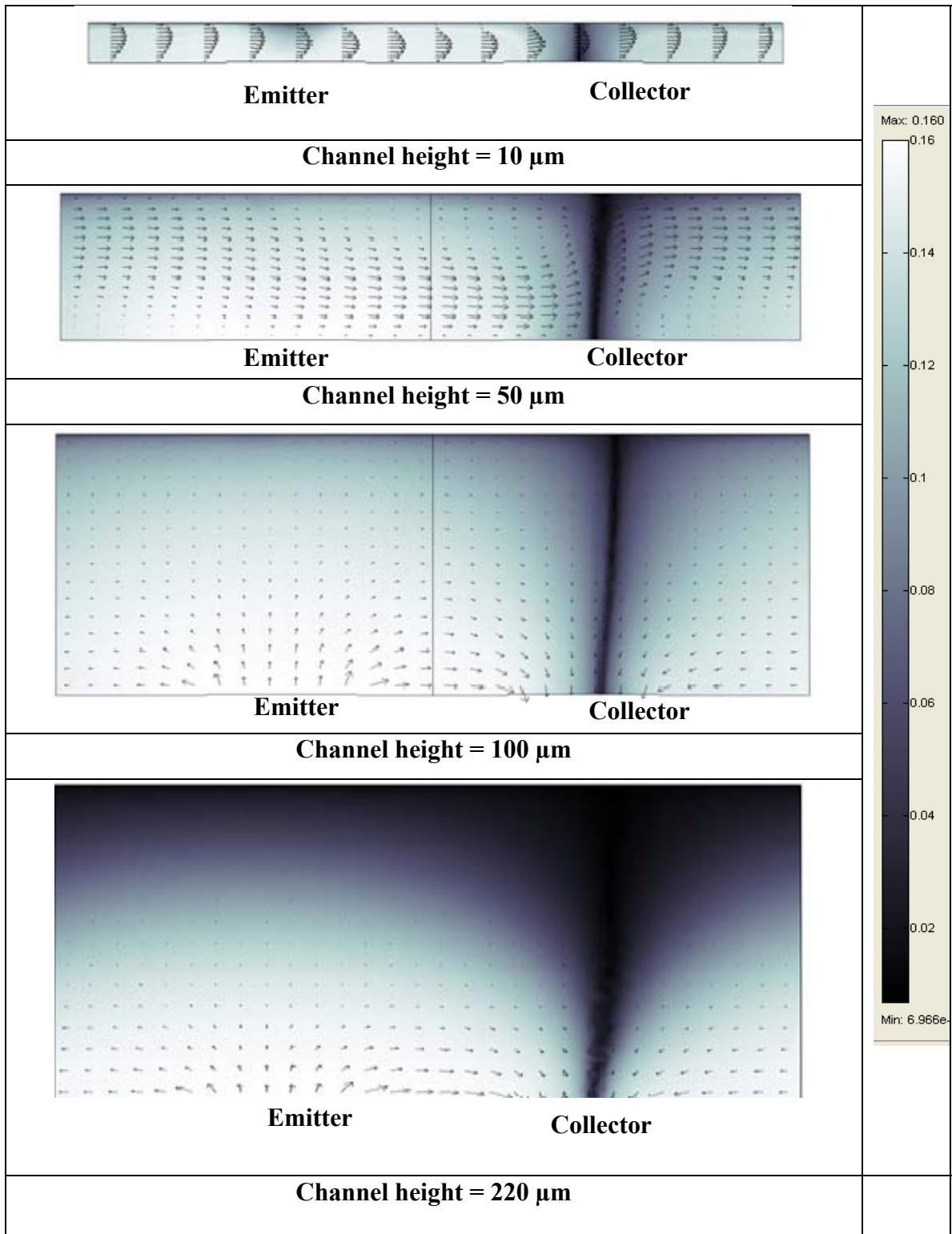
different channel heights. All designs except the 10- μm channel had strong recirculatory flows. This partially explains the low efficiency of the micropump. Also seen are regions close to the substrate past the collector electrode where local backflow is caused by neighboring electrode stages. For 110 μm channel heights, the flow resembles a fully developed velocity profile, but the internal flow resistance is too high for effective pumping.

Table 5-6 Flow streamlines overlaid on the velocity field for ion-drag micropump 50f100 with 10, 50, 100, and 220 μm channel heights. Velocity vectors are represented by white arrows, and velocity magnitude is shown according to the B-W color gradient scale shown to the right of the graphs. Operating conditions: 600 V input voltage, external loop with valve setting #1.



The charge density distributions for the same channel heights are shown in Table 5-7. For small channels, charge generation is suppressed, producing a lower current than in pumps with higher channels. The charge saturation region, which is reached when the emitter charge boundary condition does not depend on the channel dimensions for a fixed input voltage, was found for channel heights above 100 μm .

Table 5-7 Charge density profiles for ion-drag micropump 50f100 with 10, 50, 100, and 220 μm channel heights. Velocity vectors are represented by black arrows and the magnitude of velocity is shown in the B-W color scheme.



5.4.4 Electric field simulation

The most difficult variable to resolve in the ion-drag pump was charge density, as little is known about the true mechanism of charge generation, and no equations exist to describe it. Under the assumption of constant charge density (assumption 4), only the electric field can influence the performance of the pump. Since for similar electrode distances, and thus similar average electric fields, pointed electrode geometries produced better pumping in the experiments (Chapter 4), the maximum electric field has an important effect on pump performance. Identical electrode shapes with different electrode distances, having different average electric fields, also showed that the average electric field is important. The electric enhancement factor k as defined in Equation (5-14) was chosen to evaluate the combination of these two effects (Jackson 1999).

$$k = \frac{E_{\max}}{E_{\text{avg}}} \quad (5-14)$$

2-D simulation

The objective of the electric field simulation was to determine the effect of electrode geometrical design and electrode tip radius on the maximum and average electric fields, and therefore presumably on the overall performance of the pump. Thus, for the 2-D simulation only the in-plane component of the electric field was considered. This choice was based on the assumption that the maximum electric field is in the flow direction parallel to the electrodes.

The numerical model was set up using the FEMLAB electrostatics mode as discussed earlier. The geometry considered is shown in Figure 5-17, where electric field and potential contour lines are plotted. To represent manufacturing realities and to obtain

convergent results, the emitter tip radius was varied from 0.1 μm (best estimated microfabricated tolerance) to 5 μm . (An ideally sharp angle (no curvature) cannot be solved using Poisson's equation, as it leads to an infinitely large potential gradient at the boundary discontinuity.)

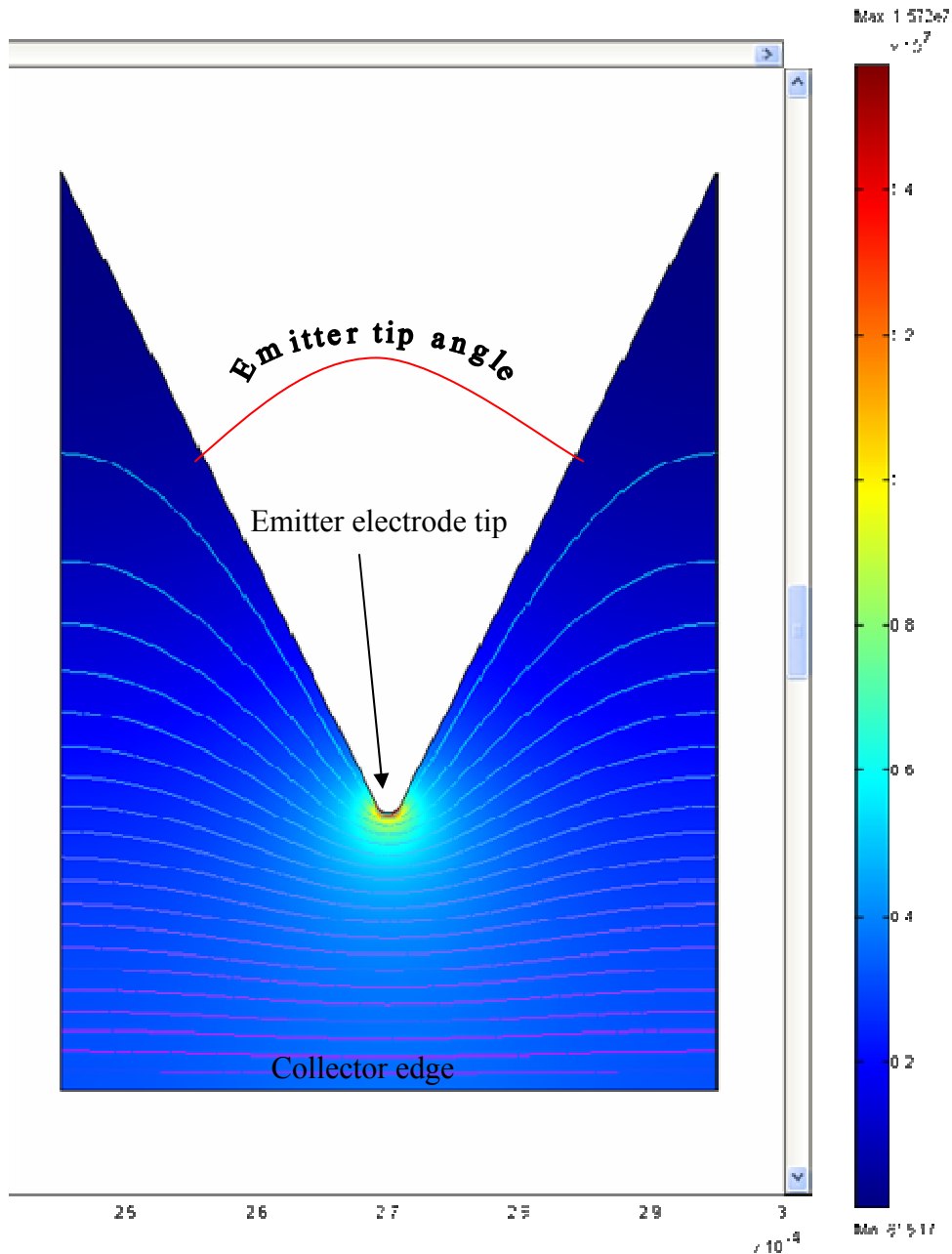


Figure 5-17 2-D model of electric field (color range) and potential (contour lines) for a saw-tooth electrode.

One effect of varying the radius of the emitter tip is shown in Figure 5-18, where an exponential decrease in k is observed with increasing radius. Such a trend was expected, as electric field is higher at smaller curvatures. Recall that the range of tip radii for the micropump prototypes in this work was between 0.5 and 2.5 μm . This confirms

that consistent emitter tip fabrication plays an important role in achieving consistent performance.

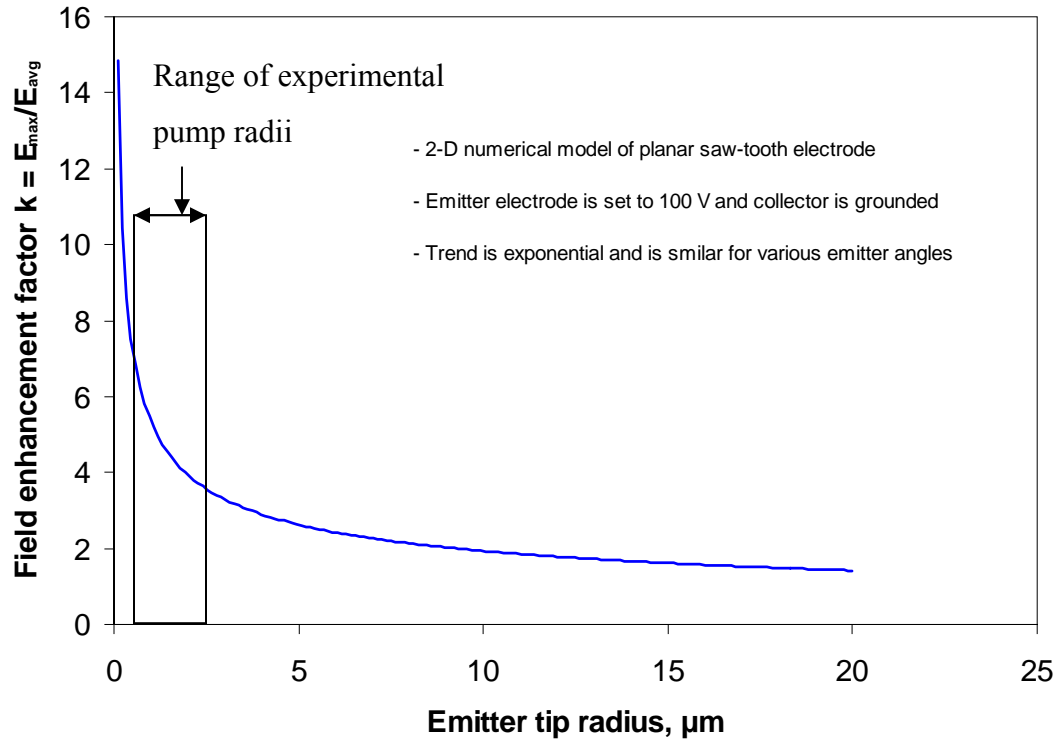


Figure 5-18 Electric field enhancement factor as a function of emitter tip radius.

Next, Figure 5-19 shows the effect of emitter saw tooth angle on the factor k . Simulations were run for two different pump designs: 20s80 and 50s100. They both have the same shape and size emitter “teeth”, but vary in distance between the electrodes (electrode pair distance was not considered). An optimum angle exists at which k reaches its maximum value. This can be explained by the effect of neighboring tips on the same electrodes. Small angle tips create higher fields that can affect charge at neighboring tips, resulting in an overall decreased maximum field due to smoothing of the overall field. Another interesting observation is that the optimum angle shifts with increasing tip radius. This is because increasing the angle with a constant tip radius

results in a smaller effective tip curvature because the spreading saw-tooth sides reduce the overall electric field.

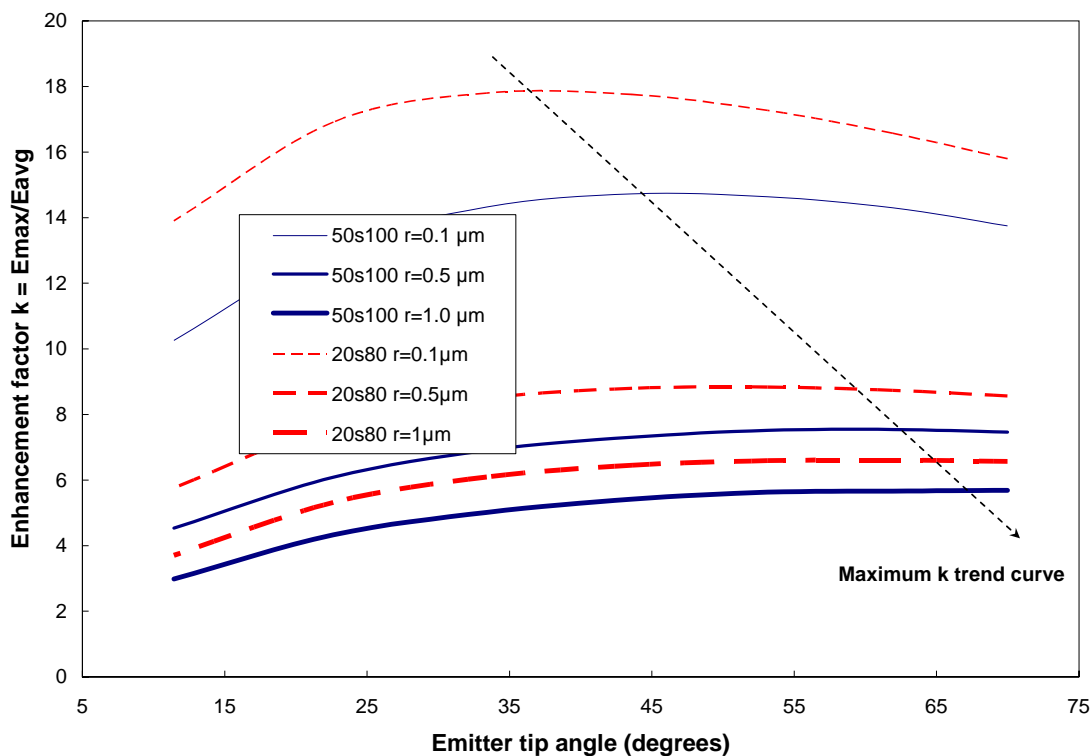


Figure 5-19 Electric field enhancement factor for saw-tooth electrode designs in a 2-D case for various emitter tip angles. There is an optimum in angle to achieve maximum k. 50s100 (blue) and 20s80 (red) designs were simulated with three different tip radii – 0.1, 0.5, and 1 μm.

Further analysis of Figure 5-19 together with Figure 5-20, which shows the effect of tip curvature on electric field, yields additional insight. A variation of as little as 0.5 μm in tooth radius of the 20s80 design could cause the pump to perform worse than the 50s100 design, even though it would normally be expected to perform better (thin blue line has higher enhancement factor than medium-thick red dashed line in Figure 5-20). The second finding is that maximum electric field plays the major role in the determining k, as the average electric field varies by only several percent for fixed electrode spacing.

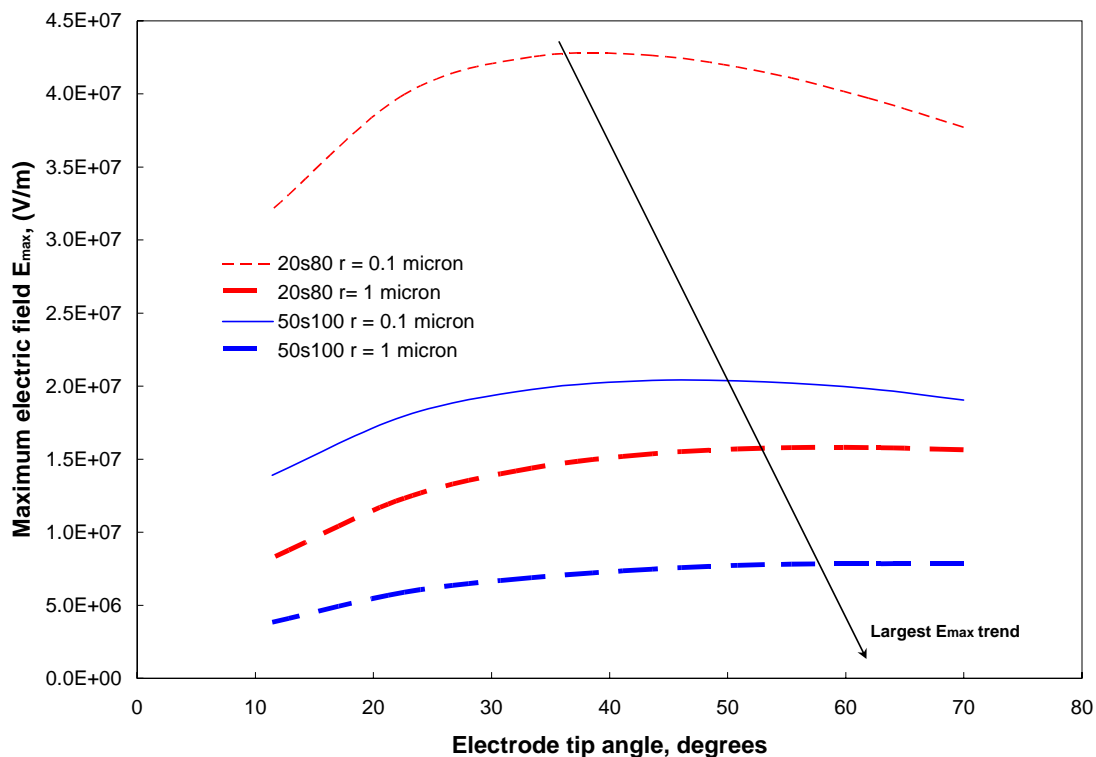


Figure 5-20 Maximum electric field for varying emitter electrode tip angles with two pump designs: 20s80 and 50s100.

5.5 Summary

A numerical model has been developed to predict ion-drag pumping performance and applied to the micropumps investigated experimentally in this study. The model was verified through good agreement between the experimental and numerical data for flow and pressure for micropump design 50f100-220. The numerical model used the experimentally determined current-voltage dependence and was built assuming unipolar charge, negligible convective current, and constant emitter electrode charge. While adjustments of up to one order of magnitude were needed for published conductivity and estimated mobility values to match the experimental and numerical currents, this was justified because the former was for AC voltages and because Walden's rule is only

accurate to within a factor of 10. The model was applied to evaluate the effects of channel height and inter-electrode spacing.

Electric field simulations were carried out to establish the optimum saw tooth design based on a field enhancement factor. Pump designs were compared in 2-D approximations for varying electrode tip radius and angle. The optimum saw-tooth angle was found to depend on both the electrode separation and the tooth radius. The findings also demonstrated the critical importance of precise micro-fabrication to obtain prototypes that produce reliable and repeatable data.

CHAPTER 6 CONCLUSIONS AND RECOMMENDED FUTURE

WORK

6.1 Introduction

In this chapter a summary of my accomplishments is given. This overview of the path taken to arrive at the conclusions summarizes the experimental data and numerical findings for the ion-drag micropump. The key challenges of the research are then reviewed, and the solutions that were implemented are presented. Recommendations for future work are listed according to the specific area of the study: experimental apparatus (test-side), design and fabrication of the pump (pump-side), and numerical work (simulation-side).

6.2 Overview and Conclusions

A main objective for the current project was to investigate *the effect of geometrical design parameters* on the performance of the micropump. Secondly, the study aimed to provide *insight into pump reliability* due to changes in the pumped liquid and electrode surface during the operation of the micropump. A secondary-level objective was the *development of a simplified numerical model* that would allow optimization of pump design parameters.

In order to achieve these goals, micropumps with several designs were fabricated and tested. The geometrical design parameters included electrode spacing and electrode pair spacing, electrode shape, and channel height. The effects of these parameters were

evaluated with respect to the performance of the pump. The findings are summarized in Table 6-1.

Table 6-1 Effect of geometrical parameters on the performance of the pump.

Geometrical parameter	Does an optimum parameter exist?	Effect description
Channel height	Flow rate – yes; Static pressure head – no; Efficiency – yes.	Applicable for specific external flow resistance: $\sim 250 \mu\text{m}$ for the current settings. Static pressure increases with decreasing height.
Electrode gap	No.	Flow rate and static pressure increase with decreasing gap. Efficiency depends on the combination of the electrode and inter-electrode gaps.
Inter-electrode pair gap	Flow rate, static pressure, efficiency – yes.	Applicable for a distance ratio factor, $X = \text{inter-electrode}/\text{electrode gaps}$. Numerically X_{optimum} was found to be 8. Experimentally increasing from $X = 2$ to 4.
Emitter electrode shape	Saw-tooth – yes. Overhang – did not investigate.	Found numerically to have an optimum saw-tooth angle that depends on tip radius. Overhang saw-tooth was found to perform better than planar saw-tooth, and both were better than flat electrodes.

To the best knowledge of the author, no former studies in the field of the ion-drag micropumps offered a parametric study on optimization of a planar ion-drag pump design

parameters. Some of the findings of this study, such as optimization of multi-stage electrode pair spacing, should be applicable to grid-type pumps as well.

A second major contribution of this work included developing a better understanding of electrode reliability during operation. Formerly, there were only limited reports of the visual appearance of the electrode surface after testing. To our knowledge, no chemical analysis of the electrodes after pump operation had been performed. This study found that collector electrodes participate in electrochemical reactions taking place during ion-drag pump operation to a greater extent than the emitter electrode. Material was deposited on the collector that consisted of fluorine, carbon, and oxygen, components of the working fluid and dissolved impurities such as oxygen gas and water. It was also found that larger electrode pair spacing reduced deposition levels, presumably due to both the lower electric field and the higher efficiency of the dissociation process on the collector surface (lower momentum charge carriers are less likely to “run away” from the collector).

As a third contribution, this work resulted in an ion-drag numerical model, which was verified with one set of experimental data. The model benefited from Shooshtari’s previous work (Shooshtari 2004) and from his additional assistance in setting up the model. Investigation of the current geometrical design parameters indicates that electrode pair spacing should be increased further for best pumping performance. The numerical model also provided predictions for optimum channel height that agreed well with experimental data for the given test loop condition.

A summary of some additional achievements and results include the following.

- The micropump was able to produce a maximum static pressure head of 750 Pa and a maximum flow rate of 15 ml/min for a voltage of 500 V. The maximum efficiency achieved was 0.2 %. The input electric power at this efficiency was 15 mW.
- Ion-drag micropumps with electrode spacing as low as 10 μm were microfabricated using the University facilities.
- The ion-drag micropump was packaged using channel heights from 100 to 1000 μm .
- A test loop was built with instrumentation capable of measuring flow rates down to 0.05 ml/min and pressure down to 2 Pa.
- The numerical model showed a good agreement with the pressure and flow results using experimental I-V curves as input to set the charge boundary condition for the emitter electrode, and modifying the fluid electric properties to match the experimental I-V curve. The extent of property modification was deemed acceptable as explained and justified in Chapter 5.

6.3 Recommendations

6.3.1 Recommendations on the test setup

Experimental setup is a key component in the study of any engineering device. For the micropump, it allows measurement of the input and output variables under desired operating conditions. The setup consists of three components: working liquid, test loop with instrumentation, and the pump. The former two determine the sensitivity of the measurements and the operating environment.

Test loop with instrumentation

Two main challenges were faced in setting up the test loop: measurement sensitivity and loop isolation from the environment. The ion-drag micropump operates at low input power (on the order of milliwatts) and has low efficiencies ($< 1\%$ for the pumps investigated in this study). For input voltages below several hundred volts, the electric current is small (in the 1-10 μA range) and the flow rates are low (on the order of 0.1-10 ml/min). Having a non-intrusive technique for measuring both parameters is crucial to accurate characterization of the micropump. The electric current was measured with a 6 $\frac{1}{2}$ digit-sensitivity multimeter (with an uncertainty of 2 μA). A 2-Pa sensitivity differential pressure transducer was used that, depending on the external loop flow resistance, could provide flow measurement accurate to 0.02 - 1 ml/min, which results in a 10-20% uncertainty.

To improve the setup, two changes are proposed. First, the stainless steel 1/8" tubing loop for fluid flow should be replaced with a *microfabricated test loop*. Liquid lines could be etched into two silicon wafer (limiting the channels to less than 500 μm for standard thickness wafers) that would be anodically bonded. A sketch of the proposed loop is presented in Figure 6-1, where only the liquid lines and electrode surface are shown. Additional components, such as a condenser or filter, could be incorporated in the liquid lines portion. A microfabricated setup would have several advantages over the existing one. Channels would be manufactured with high precision (down to 1 μm resolution). This would allow for smaller system volume and a more accurate measurement of system performance. Secondly, the integration of pump and flow lines would make a more compact overall device. Third, anodic bonding would ensure a well-

sealed pump protected from the environment. This would reduce the possibility of contaminating the liquid. However, anodic bonding would prevent the device from being taken apart for subsequent analysis.

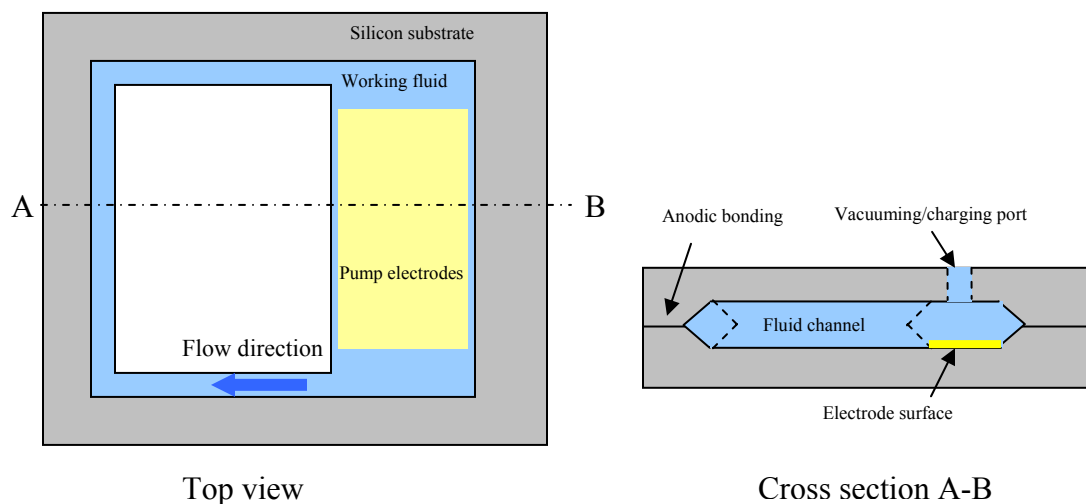


Figure 6-1 Schematic of a proposed microfabricated test loop/pumping device.

Improvements can also be made for determining pump performance parameters. Electric current could be measured with a resistor circuit such as a Wheatstone bridge for minimizing the influence on pump current during the experiment. Another option would be the acquisition of a higher precision current measurement device. A 7 ½ or 8-digit precision multimeter would yield <1% uncertainty for current measurement. In addition, the calorimetric method adapted by Shooshtari (Shooshtari 2004) would provide a second way to estimate the flow rate in the system, and could also allow calculation of the pump's heat transfer potential.

The Working fluid

In the past, several researchers have shown that the working liquid plays an important role in ion-drag pumping (Stuetzer 1959; Seyed-Yagoobi, Bryan et al. 1995).

Crowley demonstrated in his model that a combination of the fluid's mechanical and electric properties determine the performance of the ion-drag pump (Crowley, Wright et al. 1990). He showed that a higher dielectric constant increases the pressure head, as does lower viscosity and lower ion mobility. In addition, lower electrical conductivity yields higher pump efficiency. Based on this information, and the additional parameters of high liquid boiling point and low toxicity, HFE7100 manufactured by 3M was selected for this study. An in-depth discussion of its properties was provided in Chapter 3. Prior studies, however, had shown that the correlation between pump design parameters and performance varied significantly for different dielectric liquids (Bryan and Seyed-Yagoobi 1990; Crowley, Wright et al. 1990). Thus, for verification of the results of the current study, *several other working fluids* should be tested. The fluid should ideally have a simple and stable molecular structure for minimization of electrochemical reactions. Such materials, unfortunately, typically have lower dielectric constants, thereby reducing the pump's output. A compromise can be achieved with liquid nitrogen, which Darabi and Rada were among the first to pump successfully with electrohydrodynamic pumps (Darabi, Ohadi et al. 2001; Rada 2004). Lower temperature cryogenics, such as liquid helium, argon, and neon, are still waiting to be tested. For room temperature fluids, purified alcohols and other refrigerants should be tested with the micropump.

Performing tests with various working liquids is not sufficient to determine pump performance dependence on operating conditions. In addition, accurate information on the fluid physical properties is essential. The ion-drag pump model discussed in Chapters 2 and 5 takes several fluid properties into consideration. Among these are the charge

mobility, bulk electric conductivity, and viscosity. The latter is a well-defined material property, for which data are widely published for all fluids of interest. The electric properties are more difficult to acquire. Estimation of ion mobility (Chapter 2) is based on empirical correlations rather than direct measurement. For HFE-7100, the manufacturer has not published data on ion mobility. Thus *direct measurement of ion mobility* should be performed. Similarly, the electric conductivity has been estimated using the manufacturer's values from AC measurements at 1 KHz. However, the AC conductivity value is known to be up to several orders of magnitude higher than the DC conductivity. Measurement of this property is essential to characterization of the pump as well.

6.3.2 Recommendations on the design and fabrication of EHD micropumps

Electrode fabrication

The ion-drag pumping mechanism relies on the electrodes to provide the electric field and to inject the charge. The planar ion-drag pump uses a series of many electrode pairs that serve as multiple charge-injection points. Basic electrostatics indicates that the electrode geometry determines the magnitude of the electric field (Jackson 1999): sharper edges yield a higher field. Numerical simulations in Chapter 5 showed that the maximum field is sensitive to the radius of sharp protrusions on the order of several micrometers. Decreasing the tip radius by a factor of two can yield an electric field that is higher by a factor of ten. Because of these geometrical effects, particular care must be taken to produce electrodes with precise dimensional control in the microfabrication

process. Several improvements are suggested to attain better control over electrode manufacture.

- 1) Use the best photolithography mask possible. A soda-lime mask was used for the devices in the current study, which gave a significant reduction in the yield for feature sizes below 20 μm . Quartz, a more transparent, though more expensive material, should be used for mask manufacture.
- 2) Use the lift-off fabrication technique. It has two main advantages over etching for multi-parallel-line geometries. First, if a small particle is stuck to the mask, or if there is any defect, metal bridges that short the circuit are produced with positive masks (etching process), while negative masks leave small gaps, thus only voiding that arm of the electrode. Second, liftoff results in more consistent features, while etching requires precise timing, etchant concentration, and temperature control for repeatable feature dimensions.

Electrode design

The inverse dependence of electric field on distance between the electrodes suggests ***reducing the electrode gap*** to the smallest dimension possible. Experimental results show that operating voltage decreases linearly with electrode spacing for a fixed pumping output. Microfabrication can produce features smaller than 1 μm . In parallel, for a multistage grid, ***electrode pairs should be spaced at the optimum distance*** determined by numerical simulation (Chapter 5).

A second recommendation concerning design of the electrodes is based on the finding in this work and by previous researchers (Darabi, Rada et al. 2002) that the shape of the emitter controls the injection of charge. Sharper tips and higher vertical

dimensions produce proportionally higher charge injection at a given power input than identically spaced low-profile electrodes. Emitter electrodes should thus have a high vertical dimension, in conjunction with a channel depth for minimum pressure drop, as well as geometrical protrusions in the direction of flow. Electrode profile can be increased only to a limited extent using conventional thin film deposition techniques. Thus another method of metallization needs to be used. **Electroplating** could provide an inexpensive way to increase the height of the emitter electrode. In the current study, features as high as several micrometers were achieved with gold electroplating, versus 1 μm for thermally evaporated layer. For the emitter shape, Darabi proposed an overhang at the saw-tooth tip and circular bumps, which TRW manufactured using solder bump technology (Darabi, Rada et al. 2002).

Certain benefits could be achieved by redesigning the collector electrode, at which the injected charge is reduced. The experimental work showed that the majority of destructive electrochemical reactions took place on the collector surface. To increase charge collection, it would be advisable to **increase the area of the collector and smooth its surface**. **Changing the emitter metal** could also be beneficial. Since the emitter did not suffer damage, switching to a metal with a lower work function more readily able to inject charge might be beneficial.

Pump packaging

As shown experimentally, channel depth plays an important role in operation of the planar pump. Using silicon fabrication, it is possible to build a MEMS package that would incorporate microchannels, active ion-drag pumping surface, and integrated electronics. Pumps can be easily configured for multi-stage operation to increase

pressure head using an in-series configuration, and flow rate may be increased by placing pumping units in parallel. Pumps could also be produced by stacking several electrode surfaces instead of manufacturing a single-level planar pump. The proposed configuration for stacked pump design is Figure 6-2.

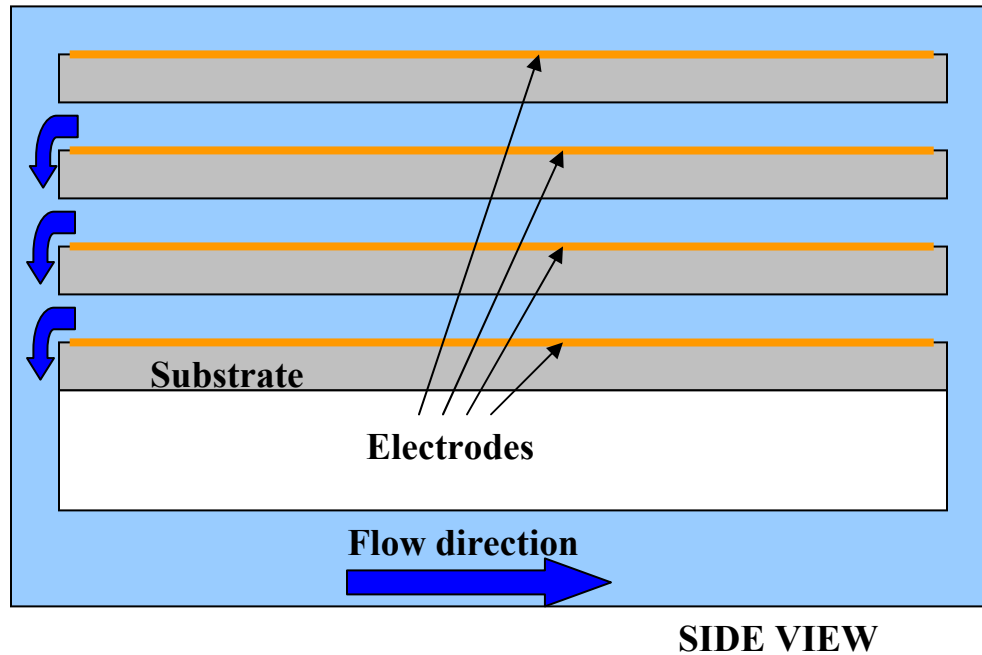


Figure 6-2 Stacked ion-drag pump packaging schematic.

6.3.3 Recommendations on the numerical modeling of the ion-drag micropump

The numerical model, though successfully verified with experimental data from one of the micropump designs, still has plenty of room for improvement.

- 1) **Verify the model with additional pump designs.** A more complex design, such as 50s100, should be used for validation as well. Because of the emitter saw-tooth shape, numerical models for these designs

require a 3-D computational domain and significantly more computational power.

- 2) **Derive expressions for the emitter charge boundary condition.** This step is an essential improvement in the model, making it independent of experimental data.

6.4 Summary

In this chapter an overview of the work performed was provided and major contributions were discussed. The challenges faced were identified and existing or proposed solutions offered. Finally, recommendations for future work to further increase the understanding of the ion-drag pumping mechanism, and design of the working device were outlined.

APPENDIX A

1. Pre-fabrication steps

a. Process selection

Electrode fabrication can be done in two ways: using either the negative field or the positive field mask. The methods differ in the sequence of major microfabrication steps, and several specific processes. Both methods were used to fabricate the ion-drag micropumps investigated in this study. Negative field yielded higher output for smaller electrode spacings; however, at the expense of longer fabrication time. Positive field fabrication process had lower yield due to the frequent build-up of random small metal bridges between the electrodes.

b. Mask drawing and ordering

Once chosen the method of fabrication, a photolithographic mask was designed. Commercial vendor Photo-Sciences, Inc. (San Jose, CA) was chosen for low rates and former history of working well with the University research labs. Micropump electrode design was drawn in AutoCAD using mask design rules (read more on <http://www.photosciences.com>) and submitted to the vendor. Typical turn-around time is about 2-3 weeks. For cost considerations, soda-lime substrate with feature sizes 5 μm and relative tolerance of 0.25 μm was used for the pump. More details on this process are available in the Chapter 3.

c. Substrate selection and sizing

Ion-drag micropump substrate selection guidelines are listed in the Chapter 3. The substrates selected for the pumps under investigation were silicon and alumina. They were sized to a typical microchip area of 1x2 cm.

2. Fabrication steps

a. Substrate cleaning and dehydrating

In order to perform successful microfabrication, cleanliness of the substrate is essential. It was done using two-step process. First, newly received substrates from the manufacturers were cleaned from organic and inorganic contaminants using Piranha solution. It consists of 5:1 of H_2SO_4 with H_2O_2 . The mixture is self-heating and the H_2O_2 has to be added slowly. Cooling solution loses its effectiveness, however, it can be refreshed by adding more H_2O_2 . After using piranha etch for about 10 min, de-ionized (DI) water is used to clean the wafer. Next, the wafer is spin-dried and dehydrated on the hot plate at 120°C for 10 min. In case of the wafers being already previously cleaned with the piranha etch, wafers are cleaned with the three organic solvers: acetone, methanol and isopropanol by spraying them on the substrate and cleaning with the DI water afterwards.

b. Positive field fabrication process (etching)

i. Thin film deposition (metallization)

Gold (Au) electrodes were used for the ion-drag pump. Gold does not adhere well to the alumina or silicon substrate, so an adhesion layer of chromium is used in between the gold and the substrate. Deposition techniques used: thermal evaporation and e-beam deposition. They both yield about the same quality bulk material. Cr/Au film thickness can be reached up to $1\ \mu\text{m}$ (Madou 2002). Further increase in the thickness of the electrode metal would yield cracks and delaminating due to the intrinsic stresses in the gold.

ii. Photoresist spinning

Shipley 1813 positive photoresist is used for the microfabrication. It is spun at 4000 RPM on the substrate for 40 seconds to get a 1.3 μm uniform thickness photoresist.

iii. Soft bake

For better adhesion photoresist is soft baked on the hot plate at 90 °C for 60 seconds.

iv. Mask exposure

UV (ultraviolet) light is used to expose the positive field pattern of the electrodes on the photoresist. An 8 mW/cm^2 UV light setting is used for 12 seconds.

v. Photoresist development

Clariant AZ 400 K inorganic developer is diluted with DI at ratio of 1:3 and used to develop the pattern in the photoresist. Development time is about 60-80 seconds.

Several times stirring helps to promote the development of the photoresist.

vi. Pattern check

Developer is washed off with the DI and dried with the nitrogen gas. Then the electrode pattern is checked for faulty lines through the optical microscope. If problems are found, photoresist is stripped off and steps are repeated from ii)

vii. Hard bake

Photoresist is hard baked for 5 minutes at 110 °C for better adhesion.

viii. Wet etching

Liquid etchant is used to remove the parts of gold and chrome that are not protected by the photoresist.

ix. Photoresist stripping

Once metal is etched, photoresist is stripped off with the Clariant AZ400T stripper for 1-2 hours.

c. Negative field fabrication process (liftoff)

i. Photoresist spinning

Same as ii) for positive field mask

ii. Soft bake

Same as iii) for positive field mask

iii. Mask Exposure

Same as iv) for positive field mask except the UV bulb setting is for 12 mW/cm² and used for 15-17 seconds.

iv. Photoresist chemical treatment

The photoresist is treated for 15 min by fully soaking the substrates in the bath of chlorobenzene. This changes the molecular structure of the several hundred Å by diffusing the chlorobenzene into the photoresist

v. Soft bake

The substrate is soft baked at 90⁰ for 5 min to strengthen the bond of diffused chlorobenzene.

vi. Photoresist developer

Photoresist is developed in AZ400K for 2-2.5 minutes. Watch for two-stage development: first, the top layer of the photoresist takes about 1-1.5 minutes, and then untreated layer of photoresist is being developed during the next 30-60 seconds.

vii. Pattern check

Same as vi) for positive mask field.

viii. Metallization

Same as i) for positive field process

ix. Lift-off

Use AZ 400T to lift-off the developed photoresist and the thin metal layers on top of it.

3. Electrode grid inspection

a. Electrical

Once the electrode grids are fabricated, they are checked using multimeters for any shorts between the collector and emitter electrode strips.

b. Visual

Same inspection is done visually to ensure the uniformity of the electrodes.

4. Electrode dimensions measurement

a. Profilometer

Profilometer readings are taken to evaluate the true thickness of the electrodes and the roughness of their surface.

b. Optical

Optical measurements are done for electrode gap, width, emitter saw-tooth radius, and inter-electrode spacing.

5. Numbering substrates

Final step is numbering of the substrates for further use and classification.

APPENDIX B

EES (Engineering Equation Solver) code for a simplified analytical model of the EHD pump

```

Tamb = 300
Pamb = 1
miu_HFE7100 = viscosity(HFE7100,T=Tamb,P=Pamb)
rho_HFE7100 = density(HFE7100,T=Tamb,P=Pamb)
rho_water = density(WATER,T=Tamb,P=Pamb)
hfe7100_spec = rho_HFE7100/rho_water

V_dot_mlmin = 3
V_dot = V_dot_mlmin/60/1e6           {flow rate in m^3/s}

w = 1.15e-2
{h = 300e-6}
L = 250e-6
ar = h/w
hmic = h*1e6

                                     {friction factors from R. Olson - best fit}
fRe = 34.590*ar^4 - 117.396*ar^3 + 172.393*ar^2 - 128.636*ar + 95.963

Ainlet = w*h
D_h = 4*Ainlet/2/(w+h)             {hydraulic diameter}
u_m = V_dot/Ainlet
Re = u_m*D_h*rho_HFE7100/miu_HFE7100

f = fRe/Re

P_muump = f*rho_HFE7100*u_m^2/(2*D_h)*L
F_muump = P_muump/h/89000         {Fluid friction force in the channel}

F_electric = h^(-1)*1e9/250/4e10   {Empirically designed electric body
force; the goal here was to build a force function that has a power-law described dependency on
the channel height: this correlation has been obtained from numerical simulations; force scaling
is accomplished for the purpose of having a similar order of magnitude force as the friction force}

Fnet = F_electric-F_muump         {Net force}

hm = h*1e6                       {in microns}

```

REFERENCES

- Ahn, S. H. and Y. K. Kim (1998). "Fabrication and experiment of a planar micro ion drag pump." Sensors and Actuators, A: Physical **70**(1-2): 1-5.
- American Society of Heating Refrigerating and Air-Conditioning Engineers. (2003). 2003 ASHRAE handbook : heating, ventilating, and air-conditioning applications. Atlanta, Ga., ASHRAE.
- Asano, K. and K. Yatsuzuka (1999). Fundamental study of EHD pump with needle-cylinder electrodes. Conference on Electrical Insulation and Dielectric Phenomena, Piscataway, NJ, USA.
- Atten, P. (1996). "Electrohydrodynamic instability and motion induced by injected space charge in insulating liquids." IEEE Transactions on Dielectrics and Electrical Insulation **3**(1): 1-17.
- Atten, P., L. Elouadie, et al. (1989). Electroconvection in a wire-cylinder geometry with forced flow and its effect on heat transfer. Conference Record of the 1989 IEEE Industry Applications Society Annual Meeting, New York, NY, USA.
- Atten, P. and J. Seyed-Yagoobi, Eds. (2003). Electrohydrodynamically Induced Dielectric Liquid Flow Through Pure Conduction in Point/Plane Geometry. IEEE Transactions on Dielectrics & Electrical Insulation.
- Barbini, G., R. Bozzo, et al. (1993). Influence of the electrode geometries on ion-drag overpressure production. IEEE 11th International Conference on Conduction and Breakdown in Dielectric Liquids (ICDL), New York, NY, USA.
- Barbini, G. and G. Coletti (1995). "Influence of electrode geometry on ion-drag pump static pressure." IEEE Transactions on Dielectrics and Electrical Insulation **2**(6): 1100-1105.
- Bart, S. F., L. S. Tavrow, et al. (1990). "Microfabricated Electrohydrodynamic Pumps." Sensors and Actuators, A: Physical **21**(1-3): 193-197.
- Bologa, M. K., I. V. Kozhevnikov, et al. (2000). Multistage electrohydrodynamical pump. Conference on Electrical Insulation and Dielectric Phenomena, Piscataway, NJ, USA.
- Bologa, M. K., I. A. Kozhukhar, et al. (1999). Electrohydrodynamic pumps. Proceedings of the 1999 IEEE 13th International Conference on Dielectric Liquids, Piscataway, NJ, USA.
- Bologa, M. K., I. A. Kozhukhar, et al. (1993). Electrohydrodynamic pump service life. IEEE 11th International Conference on Conduction and Breakdown in Dielectric Liquids, Piscataway, NJ, USA.

- Bryan, J. E. and J. Seyed-Yagoobi (1990). "Experimental study of ion-drag pumping using various working fluids." IEEE Transactions on Electrical Insulation **2**(4): 647-655.
- Bryan, J. E. and J. Seyed-Yagoobi (1990). Ion-drag electrohydrodynamic pumping-selecting an optimum working fluid. 10th International Conference on Conduction and Breakdown in Dielectric Liquids (ICDL), New York, NY, USA.
- Bryan, J. E. and J. Seyed-Yagoobi (1992). "An Experimental Investigation of Ion-Drag Pump in a Vertical and Axisymmetrical Configuration." IEEE Transactions on Industry Applications **28**(2): 310-316.
- Castaneda, J. A. and J. Seyed-Yagoobi (1991). Electrohydrodynamic pumping of refrigerant 11. Conference Record of the 1991 IEEE Industry Applications Society Annual Meeting, New York, NY, USA.
- Castellanos, A. (1998). Electrohydrodynamics. New York, Springer Wien.
- Castellanos, A. and N. Agrait (1992). "Unipolar Injection Induced Instabilities in Plane Parallel Flows." IEEE Transactions on Industry Applications **28**(3): 513-519.
- Castellanos, A. and A. Gonzalez (1998). "Nonlinear electrohydrodynamics of free surfaces." IEEE Transactions on Dielectrics and Electrical Insulation **5**(3): 334-343.
- Chattock, A. P., Walker, W.E. (1901). Philosophical Magazine(1): 79.
- Coletti, G. and R. Bozzo (1996). A contribution to the evaluation of electrohydrodynamic pumps for insulating oils. IEEE 1996 Annual Report of the Conference on Electrical Insulation and Dielectric Phenomena, New York, NY, USA.
- Crowley, J. M. (1980). "Efficiency of Electrohydrodynamic Pumps in the Attraction Mode." Journal of Electrostatics **8**(2-3): 171-181.
- Crowley, J. M., G. S. Wright, et al. (1990). "Selecting a Working Fluid to Increase the Efficiency and Flow-Rate of an Ehd Pump." IEEE Transactions on Industry Applications **26**(1): 42-49.
- Darabi, J. (1999). Micro and Macro Scale Electrohydrodynamic Enhancement of Thin-Film Evaporation. Mechanical Engineering. College Park, University of Maryland.
- Darabi, J., M. M. Ohadi, et al. (2001). "An electrohydrodynamic polarization micropump for electronic cooling." Journal of Microelectromechanical Systems **10**(1): 98-106.

- Darabi, J., M. Rada, et al. (2002). "Design, fabrication, and testing of an electrohydrodynamic ion-drag micropump." Journal of Microelectromechanical Systems **11**(6): 684-690.
- eFunda, I. (2005). Electrochemical Series: Common Metals. Sunnyvale. **2005**.
- Fowler, R. H. (1928). "The restored electron theory of metals and thermionic formulae." Royal Society -- Proceedings **117**(A778): 549-552.
- Fuhr, G., R. Hagedorn, et al. (1992). "Microfabricated Electrohydrodynamic (EHD) Pumps for Liquids of Higher Conductivity." Journal of Microelectromechanical Systems **1**(3): 141-146.
- Garimella, S. V. and V. Singhal (2004). Single-phase flow and heat transport and pumping considerations in microchannel heat sinks. Heat Transfer Engineering. **25**: 15-25.
- IEEE-DEIS-EHD Technical Committee (2003). Recommended International Standard for Dimensionless Parameters Used in Electrohydrodynamics. IEEE Transactions on Dielectrics & Electrical Insulation. **10**: 3-6.
- Incropera, F. P. and D. P. DeWitt (2002). Fundamentals of heat and mass transfer. New York, J. Wiley.
- Jackson, J. D. (1999). Classical electrodynamics. New York, Wiley.
- Kashani, R., S. Kang, et al. (2000). "Micro-scale electrohydrodynamic pumped high performance actuation." Journal of Intelligent Material Systems and Structures **11**(5): 343-350.
- Kojevnikov, I. V., O. V. Motorin, et al. (2002). Optimization of the electrohydrodynamic pump. Conference on Electrical Insulation and Dielectric Phenomena, Piscataway, NJ, USA.
- Kojevnikov, I. V., O. V. Motorin, et al. (2001). The effect of electrical field parameters, medium properties and interelectrode gap geometry on the EHD pump characteristics. Conference on Electrical Insulation and Dielectric Phenomena.
- Lee, W. Y., M. Wong, et al. (2002). "Pressure loss in constriction microchannels." Journal of Microelectromechanical Systems **11**(3): 236-244.
- Madou, M. J. (2002). Fundamentals of microfabrication : the science of miniaturization. Boca Raton, CRC Press.
- Melcher, J. R. (1981). Continuum electromechanics. Cambridge, MA, USA, MIT Press.
- Melcher, J. R. and M. Firebaug (1967). "Traveling-Wave Bulk Electroconvection Induced across a Temperature Gradient." Physics of Fluids **10**(6): 1178-&.

- Mirotvorsky, V. O. and Y. K. Stishkov (1996). Influence of near-electrode reaction on distribution of electric characteristics of "electrodes-liquid dielectric" system. 12th International Conference on Conduction and Breakdown in Dielectric Liquids (ICDL), New York, NY, USA.
- Olson, R. M. (1980). Essentials of engineering fluid mechanics. New York, Harper & Row.
- Pickard, W. F. (1963). "Ion Drag Pumping .1. Theory." Journal of Applied Physics **34**(2): 246-250.
- Pickard, W. F. (1963). "Ion Drag Pumping .2. Experiment." Journal of Applied Physics **34**(2): 251-&.
- Rada, M. (2004). EHD Pumping System for cryogenic spot cooling of low volume complex electronics. Mechanical Engineering. College Park, University of Maryland.
- Ramos, A., A. Gonzalez, et al. (2001). "Comment on "Theoretical model of electrode polarization and AC electroosmotic fluid flow in planar electrode arrays"." Journal of Colloid and Interface Science **243**(1): 265-266.
- Richter, A., A. Plettner, et al. (1991). Electrohydrodynamic pumping and flow measurement. Proceedings of the 1991 IEEE Micro Electro Mechanical Systems - MEMS '91, Nara, Japan, IEEE, Piscataway, NJ, USA.
- Richter, A., A. Plettner, et al. (1991). "Micromachined electrohydrodynamic (EHD) pump." Sensors and Actuators, A: Physical **29**(2): 159-168.
- Richter, A. and H. Sandmaier (1990). An electrohydrodynamic micropump. IEEE Micro Electro Mechanical Systems. An Investigation of Micro Structures, Sensors, Actuators, Machines and Robots, New York, NY, USA.
- Schmidt, W. F. (1990). "Electrons in nonpolar dielectric liquids." IEEE Transactions on Electrical Insulation **26**(4): 560-567.
- Schmidt, W. F. (1997). Liquid State Electronics of Insulating Liquids. New York, CRC Press.
- Schmidt, W. F. (1997). Liquid state electronics of insulating liquids. Boca Raton, CRC Press.
- Scott, M., K. Kaler, et al. (2001). "Theoretical Model of Electrode Polarization and AC Electroosmotic Fluid Flow in Planar Electrode Arrays." Journal of Colloid and Interface Science **238**(2): 449-451.
- Seyed-Yagoobi, J. (2002). Electrohydrodynamic induction pumping thermal energy transfer system and method. US, The Texas A&M University System.

- Seyed-Yagoobi, J. and K. Brand (2001). Electrode design for electrohydrodynamic induction pumping thermal energy transfer system. USA.
- Seyed-Yagoobi, J. and J. E. Bryan (2003). Electrohydrodynamic Conduction Pump. USA.
- Seyed-Yagoobi, J., J. E. Bryan, et al. (1995). "Theoretical-Analysis of Ion-Drag Pumping." IEEE Transactions on Industry Applications **31**(3): 469-476.
- Shoji, S. and M. Esashi (1994). Microflow Devices and Systems. Journal of Micromechanics and Microengineering. **4**: 157-171.
- Shooshtari, A. (2004). Experimental And Computational Analysis Of An Electrohydrodynamic Mesopump For Spot Cooling Applications. Mechanical Engineering. College Park, University of Maryland.
- Shou-Shing Hsieh, C.-Y. L., Chin-Feng Huang and Huang-Hsiu Tsai (2004). "Liquid flow in a micro-channel." Journal of Micromechanics and Microengineering **14**(4): 436-445.
- Stratton, J. A. (1941). Electromagnetic theory. New York, London,, McGraw-Hill book company, inc.
- Stuetzer, O. M. (1959). "Instability of Certain Electrohydrodynamic Systems." Physics of Fluids **2**(6): 643-648.
- Stuetzer, O. M. (1959). "Ion Drag Pressure Generation." Journal of Applied Physics **30**(7): 984-994.
- Stuetzer, O. M. (1960). "Ion Drag Pumps." Journal of Applied Physics **31**(1): 136-146.
- Washabaugh, A. P., M. Zahn, et al. (1989). "Electrohydrodynamic Traveling-Wave Pumping of Homogeneous Semi-Insulating Liquids." IEEE Transactions on Electrical Insulation **24**(5): 807-834.
- Watson, P. K. (1996). EHD-enhanced, space-charge-limited currents in insulating liquids. Conference on Electrical Insulation and Dielectric Phenomena, New York, NY, USA.
- Wong, C. C., D. Chu, et al. (1995). Rapid prototyping of a micro pump with laser micromachining. Proceedings of SPIE: Micromachined Devices and Components, Austin, TX, USA.
- Yanada, H., S. Hakama, et al. (2002). "An investigation of an ion drag pump using a needle-mesh electrode configuration." Proceedings of the Institution of Mechanical Engineers, Part C: Journal of Mechanical Engineering Science **216**(3): 325-334.

- Yang, L.-J., J.-M. Wang, et al. (2003). The micro ion drag pump using indium-tin-oxide (ITO) electrodes. IEEE The 16th Annual International Conference on Micro Electro Mechanical Systems, Piscataway, NJ, USA.
- Yu, Z. Q., K. Hallinani, et al. (2002). "Electrohydrodynamically augmented micro heat pipes." Journal of Thermophysics and Heat Transfer **16**(2): 180-186.
- Zeng, S. L. and C. H. Chen (2001). "Fabrication and characterization of electroosmotic micropumps." Sensors and Actuators, B: Chemical **79**: 107-94.
- Zhakin, A. I. (1999). Conduction and electrochemistry of liquid dielectrics. 13th International Conference on Dielectric Liquids (ICDL), Piscataway, NJ, USA.
- Zhakin, A. I. (2002). Theoretical investigation of complex ion formation in liquid dielectrics. 14th International Conference on Dielectric Liquids (ICDL) 2002, Piscataway, NJ, USA.
- Zhakin, A. I. and S. A. Lunev (1998). "Analysis of the operation of a grid EHD pump included in a closed hydraulic loop. I. The approximate theory." Magnetohydrodynamics **34**(3): 225.